Karolina Gronkiewicz

Ph.D. thesis within the Warsaw-4-PhD Doctoral School at the

Institute of Physical Chemistry
Polish Academy of Sciences

Single-molecule fluorescence on multilayer graphene and graphene boron nitride hybrids

IChF
Institute of Physical Chemistry PAS

IChF
Institute of Physical Chemistry PAS

Ph.D. thesis within the Warsaw PhD School in Natural and BioMedical Sciences at the

Institute of Physical Chemistry
Polish Academy of Sciences
Kasprzaka 44/52, 01-224 Warsaw

Single-molecule fluorescence on multilayer graphene and graphene boron nitride hybrids

Supervisor
Prof. Philip Tinnefeld
Auxiliary supervisor
Dr. Izabela Kamińska

Ph.D. Candidate
M.Sc. Karolina Gronkiewicz

Warsaw, February 2025

"Our virtues and our failings are inseparable, like force and matter. When they separate, man is no more"

Nikola Tesla

Acknowledgments

First and foremost, I would like to express my gratitude to my supervisor, Prof. Philip Tinnefeld, for his help and support, which have been instrumental in bringing my PhD journey to a successful conclusion.

I would also like to extend my heartfelt thanks to my auxiliary supervisor, Dr. Izabela Kamińska, whose guidance and support were essential to completing this work. Your advice and encouragement have been invaluable. Many thanks for everything!

Despite the challenges along the way, I have always been able to count on the support of Prof. Jacek Waluk. I am grateful for his willingness to help and the time he dedicated to my work whenever I needed it.

I am also sincerely thankful to my friends and colleagues from the Institute for creating a stimulating and supportive environment. Special thanks go to Dr. Agnieszka Jamrozik, the best lab-mate I could have asked for. Your companionship helped to make this journey not only productive but also enjoyable.

On a personal note, I want to express my deep gratitude to my mom and brother for their belief in me, constant encouragement, and emotional support throughout this challenging process. Your love and faith in me have been a pillar of strength.

Finally, to my husband Michał, thank you from the bottom of my heart for your patience, love, and unwavering support during the toughest times. Your presence in my life has made all the difference.

Funding acknowledgements

This thesis is part of a project that has received funding from the Foundation for Polish Science, HOMING/2017-4/32.

This thesis is part of a project that has received funding from the National Science Centre, Sonata 2019/35/D/ST5/00958.

1-month research stay at the foreign laboratory (Ludwig Maximilians Universität München) has been founded by The Polish National Agency for Academic Exchange within the project "STER", No. BPI/STE/2021/1/00034/U/00001.

This project was developed within the Warsaw PhD School in Natural and BioMedical Sciences (Warsaw-4-PhD Doctoral School) at the Institute of Physical Chemistry of the Polish Academy of Sciences.

List of publications

Publications related to the thesis:

1. Kamińska, I., Bohlen, J., Yaadav, R., Schüler, P., Raab, M., Schröder, T., Zähringer, J., **Zielonka, K.**, Krause, S., & Tinnefeld, P. (2021). Graphene energy transfer for single-molecule biophysics, biosensing, and super-resolution microscopy. *Advanced Materials*, *33* (21), 2101099.

2. **Gronkiewicz, K.**, Richter, L., Knechtel, F., Pyrcz, P., Leidinger, P., Günther, S., Ploetz, E., Tinnefeld, P., & Kamińska, I. (2024). Expanding the range of graphene energy transfer with multilayer graphene. *Nanoscale*, *16* (1), 123-134.

3. **Gronkiewicz, K.**, Pyrcz, P., Brzeziński M., Tinnefeld, P., & Kamińska, I. Van der Waals platforms of hexagonal boron nitride and graphene combined with DNA nanostructures investigated via single-molecule graphene energy transfer, *in preparation.*

Other publications:

4. Adamczyk, J. A., **Zielonka, K.**, Kotarba, S., Saramak, J., Glowacki, I., Rachwalski, M., & Pieczonka, A. M. (2021). Photophysical properties of novel fluorescent thin solid layers based on the aggregation induced emission of alkoxy-substituted salicylaldehyde azines. *Journal of Luminescence, 229*, 117668.

5. Bednarz, A., Kamińska, I., Jamrozik, A., **Zielonka, K.**, Listkowski, A., & Waluk, J. (2021). Substituent screening effect on single-molecule photostability: comparison of three differently substituted porphycenes. *Methods and Applications in Fluorescence, 9* (3), 035004.

Conferences:

1. **K. Zielonka**, R. Yaadav, J. Bohlen, B. Bałamut, M. Sobieska, J. Waluk, P. Tinnefeld, I. Kamińska, “Graphene/DNA origami biosensors for the detection and investigation of single biomolecules”, ***MicroSymposium IPC, PAS***, 2020, **poster presentation.**
   *This poster received the Scientific Committee Award

2. **K. Zielonka**, S. Krause, R. Yaadav, J. Bohlen, J. Waluk, P. Tinnefeld, I. Kamińska “White graphene in single-molecule biosensors: hBN/graphene heterostructures”, ***MicroSymposium IPC, PAS***, 2021, **poster presentation.**

3. **K. Zielonka**, M. Pryidarsi, R. Yaadav, P. Tinnefeld, I. Kamińska, „Heterostruktury 2D w roli obiecujących platform do badań na poziomie pojedynczych cząsteczek”, **BioOrg** 2022, **poster presentation.**

4. **K. Zielonka**, R. Yaadav, P. Tinnefeld, I. Kamińska, „2D heterostructures in single-molecule fluorescence microscopy”, Graphene Week, 2023, **oral presentation.**

5. **K. Gronkiewicz**, R. Yaadav, A. M. Szalai, G. Ferrari, L. Richter, J. Jagiełło, A. Dobrowolski, T. Ciuk, P. Tinnefeld, I. Kamińska, “2D heterostructures composed of graphene and hBN for single-molecule fluorescence microscopy”, ***MicroSymposium IPC, PAS*** 2024, **poster presentation.**

6. **K. Gronkiewicz**, L. Richter, P. Pyrcz, S. Günther, E. Ploetz, P. Leidinger, P. Tinnefeld, I. Kamińska, „Kanapki” z materiałów 2D – obiecujące platformy do badań na poziomie pojedynczych cząsteczek, **Kryształy Molekularne**,2024, **poster presentation.**

7. **K. Gronkiewicz**, L. Richter, P. Pyrcz, S. Günther, E. Ploetz, P. Leidinger, P. Tinnefeld, I. Kamińska, *“Focused on nanomaterials: Multilayer graphene and van der Waals heterostructures for single-molecule fluorescence microscopy”, **Single-Molecule Sensors and NanoSystems International Conference**, 2024, **oral presentation.**

8. **K. Gronkiewicz**, L. Richter, P. Pyrcz, S. Günther, E. Ploetz, P. Leidinger, P. Tinnefeld, I. Kamińska, “Multilayer graphene and van der Waals heterostructures for single-molecule fluorescence microscopy”, ***MicroSymposium IPC, PAS***, 2025, **poster presentation.**

Abstract

Graphene, renowned for its exceptional optical and electronic properties, has emerged as a pivotal material for understanding and controlling molecular interactions at the nanoscale. Its unique characteristics are particularly significant for advancements in biosensing, super-resolution microscopy, and quantum technologies. Graphene energy transfer (GET), a highly distance-dependent phenomenon with an active range of up to 40 nm, provides precise control over molecular interactions. DNA origami nanostructures serve as scaffolds in this context, enabling the precise placement of fluorophores relative to graphene with nanometric axial resolution below 3 nm. These constructs underpin the development of biosensors for single-molecule detection and real-time studies of biomolecular dynamics and interactions.

This thesis advances the field by introducing complex platforms composed of two-dimensional materials, extending the capabilities of graphene monolayers. An optimized protocol for fabricating high-quality graphene monolayer on glass substrates enabled the development of multilayer graphene and heterostructures with tunable properties. Systematic investigations of mono-, bi-, and trilayer graphene revealed additive effects of multiple layers on fluorescence quenching efficiency, thereby extending the dynamic range of GET. Experimental findings were validated by a theoretical model describing the influence of graphene layer numbers on energy transfer dynamics.

The integration of graphene with hexagonal boron nitride (hBN) further enhanced the performance of these platforms. hBN was selected for its exceptional compatibility with graphene, offering chemical inertness and atomic-level flatness. DNA origami nanostructures were successfully immobilized on hBN surfaces, with hBN functioning as an ultra-thin spacer that preserved the photophysical properties of dye molecules without affecting graphene's energy transfer efficiency. These heterostructures exhibited exceptional stability and reproducibility, enabling atomic-distance sensitivity and precise nanoscale control. Using hBN as an inert spacer on graphene, the recently discovered vertical alignment of DNA molecules on graphene was successfully demonstrated on hBN. The thickness of the hBN

spacer with a resolution of 0.1 nm was measured using GET, highlighting the platform's potential for precision applications at the nanoscale.

By integrating multilayer graphene and graphene-hBN heterostructures, this thesis significantly advances the application of graphene-based systems in biosensing, single-molecule imaging, and hybrid quantum sensing technologies. The results demonstrate the potential of these platforms to detect weak biomolecular interactions, fine-tune energy transfer processes, and achieve high spatial and temporal resolution. Collectively, these findings pave the way for the next-generation fluorescence-based studies and open new horizons in nanotechnology and molecular biology.

Streszczenie

Grafen, dzięki swoim wyjątkowym właściwościom optycznym i elektronicznym, odgrywa kluczową rolę w badaniach oddziaływań molekularnych w skali nanometrycznej. Jego unikalne cechy czynią go niezastąpionym w takich dziedzinach jak biosensoryka, mikroskopia superrozdzielcza czy technologie kwantowe. Transfer energii do grafenu (GET), charakteryzujący się silną zależnością od odległości (do 40 nm), stanowi innowacyjne narzędzie umożliwiające precyzyjną kontrolę interakcji molekularnych. W tym celu nanostruktury DNA origami wykorzystywane są jako rusztowania, pozwalając na dokładne pozycjonowanie fluoroforów względem grafenu i uzyskanie osiowej rozdzielczości na poziomie poniżej 3 nm. Takie platformy znajdują zastosowanie w detekcji pojedynczych cząsteczek oraz w badaniach dynamicznych procesów biomolekularnych w czasie rzeczywistym.

Przedstawiona rozprawa rozwija te technologie, proponując zaawansowane platformy oparte na materiałach dwuwymiarowych, które zwiększają możliwości aplikacyjności monowarstw grafenowych. Dzięki opracowanemu protokołowi wytwarzania wysokiej jakości monowarstw grafenu na szkle, podjęto próbę implementacji tej metody do wytworzenia wielowarstw grafenu oraz heterostruktur złożonych z różnych materiałów 2D. Badania jedno-, dwu- i trójwarstwowego grafenu ukazały addytywny wpływ kolejnych warstw na efektywność wygaszania fluorescencji oraz rozszerzenie zakresu GET. Wyniki te zostały wsparte teoretycznym modelem opisującym dynamikę transferu energii w zależności od liczby warstw grafenu.

W obszarze heterostruktur, połączenie grafenu z heksagonalnym azotkiem boru (hBN) umożliwiło stworzenie stabilnych platform 2D o wysokiej jakości. hBN jest materiałem kompatybilnym z grafenem, co zawdzięcza swojej atomowo płaskiej powierzchni oraz inertności chemicznej. Wykazano, że nanostruktury DNA origami mogą być skutecznie immobilizowane na powierzchni hBN, który – osadzony na grafenie – pełni rolę ultracienkiej warstwy dystansującej. Co więcej, struktury te charakteryzują się wyjątkową stabilnością i powtarzalnością wytwarzania, umożliwiając detekcję z nanometryczną precyzją. Dodatkowo, dowiedziono, że niedawno opracowana metoda prostopadłej immobilizacji DNA na grafenie jest

równie skuteczna na powierzchni hBN. Ponadto, grubość warstwy hBN określono za pomocą GET z precyzją 0,1 nm, co dodatkowo podkreśla potencjał hBN jako uniwersalnej platformy dla biomolekuł.

Wyniki pracy dowodzą, że integracja wielowarstwowego grafenu i heterostruktur grafen-hBN otwiera nowe możliwości w projektowaniu systemów dedykowanych biosensoryce, obrazowaniu pojedynczych cząsteczek oraz hybrydowym technologiom kwantowym. Uzyskane rezultaty wskazują na ogromny potencjał tych platform w detekcji słabych interakcji biomolekularnych, badaniu procesów transferu energii oraz osiąganiu wysokiej rozdzielczości przestrzennej i czasowej. Niniejsza rozprawa toruje drogę do opracowania nowej generacji systemów fluorescencyjnych oraz otwiera nowe perspektywy w nanotechnologii i biologii molekularnej.

Content

List of Abbreviations and Acronyms

2D – Two Dimensional

AFM – Atomic Force Microscopy

APD – Avalanche Photodiode

AOTF – Acousto-Optic Tunable Filter

BS – Beam Splitter

CCDs – Charge-Coupled Devices

CLSM – Confocal Laser Scanning Microscopy

Cy3B – Indocarbocyanine

CVD – Chemical Vapor Deposition

DFT – Density Functional Theory

DNA – Deoxyribonucleic Acid

dsDNA – Double-Stranded DNA

EDTA – Ethylenediaminetetraacetic Acid

F – Filters

FIB – Focused Ion Beam

FLG – Few-Layer Graphene

FLIM – Fluorescence Lifetime Imaging Microscopy

FRET – Förster Resonance Energy Transfer

FWHM – Full Width at Half Maximum

GET – Graphene Energy Transfer

hBN – Hexagonal Boron Nitride

L – Lense

LbL – layer-by-layer

M – Mirror

$MgCl_2$ – Magnesium Chloride

NA – Numerical Aperture

NSOM – Near-field Scanning Optical Microscopy

NT - Nucleotide

P – Pinhole

PALM – Photoactivated Localization Microscopy

PCA – Protocatechuic Acid

PCD – Protocatechuate 3,4-Dioxygenase

PMMA – Poly (Methyl Methacrylate)

ROXS – Reducing And Oxidizing System

SEM – Scanning Electron Microscope

SNR – Signal-to-Noise Ratio

ssDNA – Single-Stranded DNA

STORM – Stochastic Optical Reconstruction Microscopy

TAE buffer – Tris-Acetate-EDTA Buffer

TCSPC – Time-Correlated Single Photon Counting

Motivation

The study of nanoscale molecular interactions has gained importance in advancing both fundamental science and technological innovation. In this field lies graphene, a material with exceptional optical, electronic, and mechanical properties [1], [2]. Furthermore, its low optical absorption – only 2.3% of the incident light – renders graphene an excellent candidate for applications in optical devices, including energy conversion electrodes and graphene-on-glass coverslips for advanced microscopy [3], [4].

Graphene energy transfer (GET) represents a groundbreaking approach that leverages graphene's properties to study molecular interactions at the nanoscale. In contrast to traditional Förster resonance energy transfer (FRET), which operates effectively within a range of approximately 1–10 nm, GET extends the dynamic range and provides higher spatial resolution. This capability has significant implications for microscopy and single-molecule biophysics, enabling the study of molecular interactions with unparalleled precision [3], [5], [6]. However, certain aspects of GET remain not fully understood, including the impact of multilayer graphene on energy transfer dynamics and the potential of multi-layer systems to further extend GET's dynamic range [7], [8]. Resolving these questions is essential for optimizing graphene-based platforms for diverse applications.

Despite its remarkable potential, graphene's unique properties are often compromised when interfacing with substrates. To overcome this challenge, hexagonal boron nitride (hBN) has emerged as a highly complementary material. Thanks to its atomically flat surface, chemical inertness, and insulating properties, hBN serves as an ideal spacer, preserving the intrinsic functionality of graphene while minimizing undesirable interactions with substrates. These characteristics also position hBN as an invaluable component in heterostructure devices, where its integration with graphene enables the development of innovative platforms for nanoscale studies and fluorescence-based applications.

Additionally, while it has been recently discovered that double-stranded DNA (dsDNA) adopts vertical orientation on graphene, it is unknown whether this alignment is preserved when interfaced with hBN. Understanding this phenomenon is essential for leveraging hBN-graphene heterostructures in biosensing and molecular studies. Lastly, robust tools are needed to characterize the quality of hBN on graphene and ensure these heterostructures' reproducibility and integrity.

This thesis aims to address these challenges by:

- Studying the influence of mono-, bi-, and trilayer graphene on fluorescence quenching efficiency and energy transfer dynamics to elucidate how multilayer graphene affects the performance and operational range of GET.
- Investigating the behavior of dsDNA on hBN-graphene heterostructures to evaluate whether hBN preserves the vertical orientation previously observed for graphene.
- Employing GET as a novel approach to assess the quality of hBN on graphene and developing advanced methodologies for fabricating high-quality heterostructures for diverse applications.

This work aims to deepen our understanding of graphene’s role in energy transfer processes and its integration with hBN in advanced heterostructures. The findings may help to establish graphene-hBN platforms as versatile tools for fluorescence-based assays, single-molecule studies, and emerging nanotechnological applications. These efforts are anticipated to provide a foundation for next-generation platforms that tackle key challenges in molecular science, nanotechnology, and biophysics.

Introduction and Theoretical Background

This chapter provides a theoretical foundation for the key phenomena, substrates, and techniques that underpin this research. It begins with a detailed discussion of the interaction between light and matter, followed by an examination of energy transfer processes in donor-acceptor systems, which constitute a fundamental aspect of the present work.

1 Light-matter interaction

The interaction between light and matter includes various processes. Molecules that exhibit such interactions most prominently are called fluorophores. Among the various possibilities of light-matter interactions, this thesis focuses on electronic excitations, often accompanied by vibrational and rotational transitions. When molecules return to the ground state by emitting a photon, they are classified as fluorophores. Most room-temperature fluorophores reside in their electronic ground state. Typically, a closed-shell singlet state is denoted as S_0. Additionally, most molecules occupy the lowest vibrational energy levels associated with this electronic ground state. Molecules can absorb electromagnetic radiation with energy matching (or exceeding) the energy gap between two electronic states, thereby being promoted to a higher energy state. Once in the excited state, the molecules may dissipate the excess energy through various pathways. The variety of processes that can occur following absorption is commonly illustrated using the Jabłoński diagram (Figure 1.1).

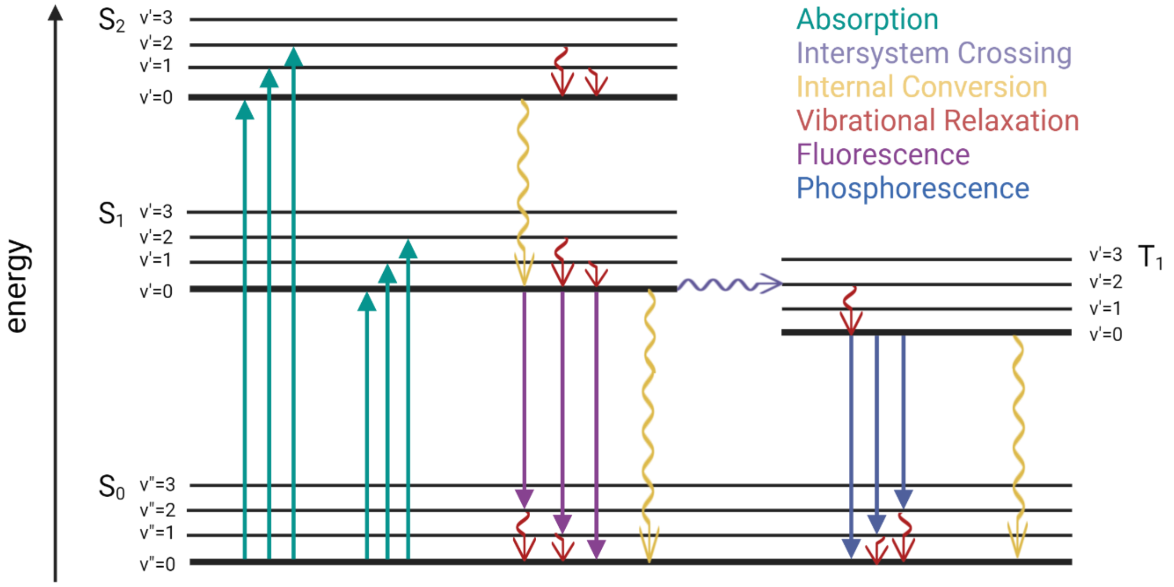

Figure 1.1 The Jabłoński diagram illustrates the energy states of an organic molecule excited to its second excited singlet state. S describes the singlet states, T the triplet state, and v the vibrational levels. All radiative processes are illustrated with straight lines, including absorption (turquoise), fluorescence (orchid), and phosphorescence (blue), and all non-radiative with wavy lines, including intersystem crossing (purple), vibrational relaxation (red), and internal conversion (yellow). Created with BioRender.com.

One of the most likely and rapid processes following excitation is intramolecular vibrational relaxation (IVR). This process occurs without changing the electronic state but involves the redistribution of vibrational energy within the molecule, ultimately leading to its dissipation as heat. Vibrational energy is transferred from higher-energy vibrational states to lower-energy ones until the molecule reaches its vibrational ground state. Internal conversion is another common pathway that may follow or compete with IVR, further contributing to the thermalization of energy. Internal conversion is another common pathway that may follow or compete with IVR. It is a non-radiative transition between electronic states of the same spin multiplicity. In organic molecules, this process occurs within picoseconds when two electronic states of the same multiplicity are energetically close. For instance, after thermal redistribution of vibrational energy in the first excited singlet state (S_1), internal conversion may occur, returning the molecule to highly excited vibrational levels of the ground state (S_0). However, this process is generally slower than internal conversion between S_2 and S_1 due to the larger energy gap between S_0 and S_1 compared to that between S_1 and S_2. As a result, other processes often compete with the relatively slow S_1–S_0 internal conversion. One competing process is fluorescence, which involves light emission as the molecule returns from the first excited singlet state (S_1) to the ground state (S_0). Although fluorescence from the S_2 state is theoretically possible, S_2 generally undergoes rapid internal conversion to S_1, leaving only a tiny fraction of excited molecules that lose energy through S_2 fluorescence. This observation is reflected in Kasha's rule, which states that fluorescence typically originates from the lowest excited singlet state, regardless of the initially excited state. In addition to singlet excited states, organic molecules can access lower-energy triplet states. However, transitions between singlet and triplet states are spin-forbidden, making them relatively weak. The non-radiative transition from a singlet state to a triplet state is known as intersystem crossing (ISC). This slow process depends on spin-orbit coupling, enhanced in molecules containing heavy atoms, such as iridium or other transition metals. The radiative transition from the triplet state back to the singlet ground state is called phosphorescence. Phosphorescence and intersystem crossing are slow processes, resulting in longer lifetimes for triplet states than singlet states, typically on the order of microseconds or longer under ambient conditions.

1.1 Radiative and non-radiative energy transfer

The previously described phenomenon occurs when a fluorophore returns to its energetically favorable ground state without external interference. However, the energy ($\mathrm{h\nu}$) of the excited molecule, referred to as the donor, can subsequently be absorbed by another molecule, called the acceptor, present in the surrounding medium. This process follows the principles of radiative energy transfer and can be represented as:

$$D^* \rightarrow D + \mathrm{h\nu} \tag{1.1}$$

$$A + h\nu \rightarrow A^* \tag{1.2}$$

Radiative energy transfer occurs when donor molecules (D) emit light, and acceptor molecules (A) absorb light from a similar spectral range. Specifically, there must be a significant overlap between the donor's emission spectrum and the acceptor's absorption spectrum. The efficiency of this energy transfer is proportional to the donor's quantum yield of emission and the acceptor's absorption in the overlapping spectral range. The probability of photon reabsorption by the acceptor (A) is inversely proportional to the square of the distance between the donor and acceptor molecules. This type of energy transfer does not alter the donor's emission lifetime but can be observed experimentally as changes in the shape of the donor's emission spectrum.

In contrast to radiative energy transfer, non-radiative energy transfer is a one-step process without photon emission and reabsorption. This transfer is driven by the direct dipole-dipole interaction between the excited donor molecules and the ground-state acceptor molecules, resulting in a reduced excited-state lifetime of the donor.

1.1.1 Dexter energy transfer

Following donor excitation, singlet states may transfer energy to the acceptor through long-range Förster resonance energy transfer (FRET) or short-range Dexter energy transfer. Triplet states, however, transfer energy exclusively via electron exchange, a Dexter mechanism. In Dexter energy transfer (Figure 1.2), energy exchange occurs only when donor and acceptor molecules are in close proximity, allowing electron overlap. This proximity limits the energy transfer range to a distance below 2 nm. During this process, electrons from the excited donor molecule (D*) are transferred to the acceptor (A). In contrast, electrons from the acceptor are simultaneously transferred to the donor, consistent with the Wigner spin rule. This mechanism permits triplet-triplet and singlet-singlet energy transfer, while singlet-triplet transitions are typically forbidden.

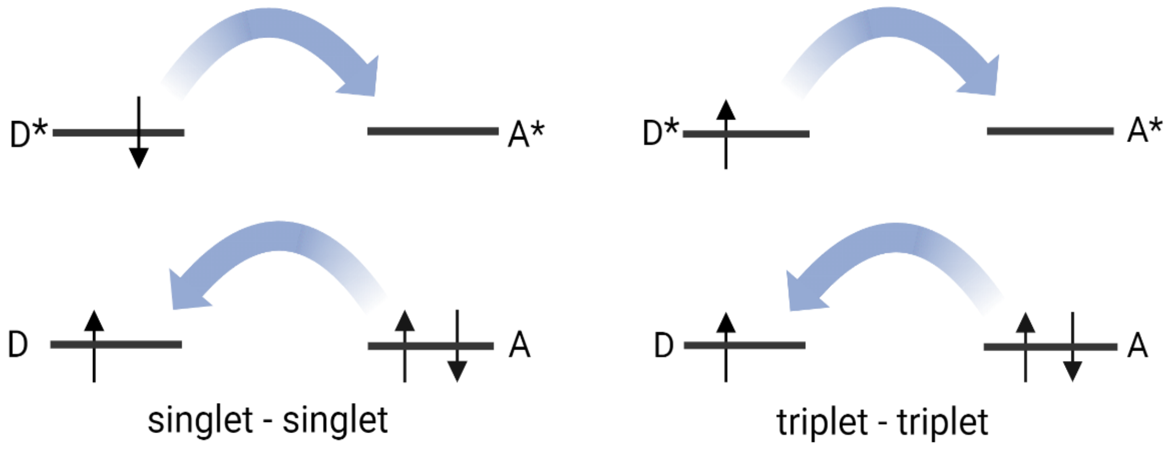

Figure 1.2 A schematic representation of Dexter energy transfer. This process involves a spin-conserved transfer between singlet-singlet or triplet-triplet states and entails a mutual exchange of electrons between the donor and acceptor. The ground and excited states of the energy donor are denoted as D and D*, respectively, while those of the energy acceptor are represented as A and A*. Created with BioRender.com.

1.1.2 Förster resonance energy transfer

In contrast, Förster resonance energy transfer (FRET) is a non-radiative process where energy is transferred from an excited donor molecule (D*) to an acceptor molecule (A) via dipole-dipole interactions (Figure 1.3). FRET can occur over distances between 2 and 10 nm, far exceeding the molecular dimensions. The efficiency of FRET is highly dependent on the distance between donor and acceptor molecules and the overlap between their emission and absorption spectra. FRET is often modeled as the interaction between two coupled oscillators, where the electric dipole moment of the donor excites the acceptor by generating an electric field that facilitates the transfer of energy. Optimal resonance requires near-identical energy levels between the donor and acceptor, conserving the electronic state multiplicity. Triplet-triplet energy transfer is allowed, while singlet-triplet transitions are generally forbidden.

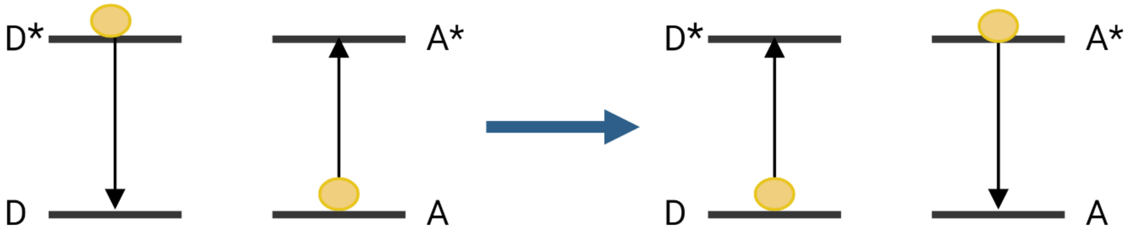

Figure 1.3 Schematic illustration of Förster resonance energy transfer. The mechanism is based on electrostatic interactions that enable nonradiative excitation energy transmission from the donor (D) to the acceptor (A). Created with BioRender.com.

The efficiency of energy transfer, E_T, quantifies the fraction of photons absorbed by the donor that are transferred to the acceptor. It can be described mathematically as:

$$E_T = 1 - \left(\frac{\tau_{da}}{\tau_d}\right) \qquad (1.3)$$

where τ_{da} represents the donor fluorescence lifetime in the presence of the acceptor, and τ_d is the donor fluorescence lifetime in the absence of the acceptor. By comparing these lifetimes, one can assess the degree of donor quenching caused by the acceptor, providing an indirect yet reliable measure of the distance between donor and acceptor molecules. This relationship arises because the acceptor shortens the donor's lifetime by energy transfer, allowing for spatial proximity between the two entities.

The E_T is highly sensitive to the donor-acceptor separation distance, r, which follows an inverse sixth-power law. This relationship can be expressed as:

$$r = R_0 \cdot \sqrt[6]{\left(\frac{1}{E_T}\right) - 1} \qquad (1.4)$$

where R_0 is the Förster radius, a critical parameter in FRET at which energy transfer efficiency between donor and acceptor is 50%.

Förster radius depends on several factors, including the spectral overlap between donor and acceptor, the donor's quantum yield, and the relative orientation of the dipoles. The spectral overlap integral, which quantifies the interaction, is expressed as:

$$\int_{0}^{+\infty} f_D(\lambda)\varepsilon_A(\lambda)\lambda^4 d\lambda \qquad (1.5)$$

where:

- λ is a wavelength (in nm),
- εA is the acceptor's molar extinction coefficient. ($cm^{-1}M^{-1}$)
- $f_D(\lambda)$ is the donor's fluorescence intensity in the absence of the acceptor.

The following equation calculates the Förster radius (R_0):

$$R_0 = 0.0211 \cdot \sqrt[6]{\frac{\kappa^2}{n^4} \cdot Q_D \cdot J} \qquad (1.6)$$

where:

- κ^2 is the dipole orientation factor (typically 2/3 for freely rotating chromophores),
- Q_D is the donor's quantum yield in the absence of an acceptor,
- n is the refractive index of the medium,
- J is the spectral overlap integral.

In summary, the overall rate of energy transfer is influenced by several key factors, including the degree of spectral overlap between the donor's emission spectrum and the acceptor's absorption spectrum, the donor's quantum yield, the relative orientation of the transition dipole moments of the donor and acceptor, as well as the distance separating the donor and acceptor molecules. Any event or process that alters the donor-acceptor separation distance will, in turn, modulate the rate of resonance energy transfer. This relationship enables the quantification of energy transfer, provided that potential artifacts are carefully controlled or eliminated.

Owing to its distance-dependent character and long-range interaction (compared to Dexter energy transfer), FRET is widely used in biological and medical research to investigate molecular distances, dynamics, and conformational changes in proteins, nucleic acids, and other macromolecules. Its sensitivity to distance makes it an ideal technique for probing molecular interactions within living cells and complex biological systems [9], [10], [11].

Having explored the various mechanisms of energy transfer, with a particular emphasis on the spatial limitations of each, it is now essential to turn our attention to graphene. This extraordinary material introduces a paradigm shift in energy transfer processes.

2 Graphene

Graphene-mediated energy transfer operates through the same physical mechanism as FRET, relying on dipole-dipole interactions. However, the effective range of energy transfer becomes significantly larger due to the integration of the many acceptors and their orientations present in the two-dimensional graphene lattice. This unique configuration offers enhanced potential for optoelectronic applications, where long-range and broadband energy transfer are advantageous. To understand its unique role as a highly versatile energy acceptor, it is essential first to examine graphene's distinctive structural and electronic properties.

The discovery of graphene marked a significant breakthrough in materials science. For years, researchers believed that two-dimensional (2D) materials were thermodynamically unstable and prone to collapsing or decomposing [1]. However, the successful exfoliation of free-standing graphene in 2004 defied these assumptions and unlocked a new research frontier [12]. This two-dimensional allotrope of carbon, consisting of a single layer of sp²-hybridized carbon atoms arranged in a honeycomb lattice (Figure 2.1), has captivated the scientific community and various industries due to its extraordinary properties.

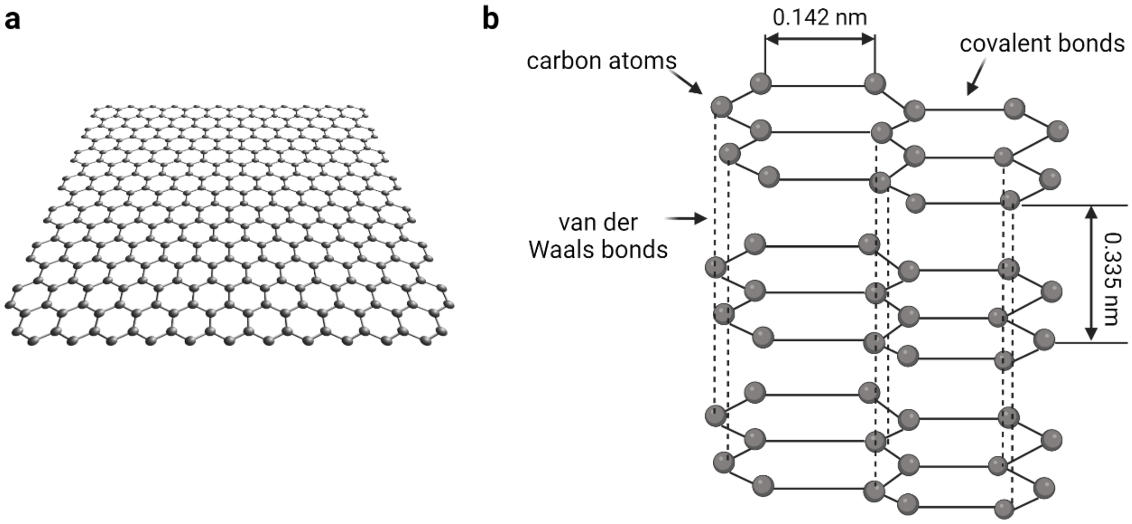

Figure 2.1 Graphical representation of (a) closely packed, sp² hybridized carbon atoms arranged in a honeycomb lattice and (b) the atomic structure of graphene [13].

Graphene's remarkable mechanical strength, lightweight nature, and exceptional thermal and electrical conductivity have opened up a wide array of applications, underscoring its pivotal role in advancing the field of nanotechnology [14]. It has become incredibly prominent in applications spanning electronics, photonics, and advanced materials science [2], [15], [16].

Beyond its mechanical and electrical advantages, graphene has also emerged as a valuable tool in fluorescence experiments due to its unique optical properties.

Specifically, its monolayer structure exhibits absorption of 2.3% in the visible (vis) and infrared (IR) spectrum. This unique optical property is directly linked to the linear dispersion relation of graphene, which implies that its charge carriers behave as massless Dirac fermions. This behavior results in several extraordinary characteristics, including high carrier mobility, constant optical conductivity, and ultrafast carrier dynamics.

Another noteworthy phenomenon associated with graphene is fluorescence quenching. Unlike Förster Resonance Energy Transfer (FRET), which requires fluorescence measurement from the donor and acceptor molecules and an analysis of their mutual interactions, fluorescence quenching by graphene operates purely through donor-based information. The presence of graphene effectively quenches the donor fluorescence without necessitating the involvement of an acceptor [4], [6], [17], [18], [19], [20]. This characteristic makes graphene an unbleachable, broadband energy acceptor suitable for diverse photophysical studies. Applications include fluorescence-based biological research [5] and super-resolution imaging techniques [3], underscoring its versatility in cutting-edge scientific investigations.

2.1 Graphene energy transfer

While Förster Resonance Energy Transfer has been extensively employed to probe molecular interactions, it is inherently limited by its dependence on the donor-acceptor distance, typically constrained to the 2-10 nm range. This limitation becomes challenging when studying biological systems or nanomaterials where longer-range energy transfer mechanisms may be desired. One approach to overcoming this constraint involves using graphene as an energy acceptor, introducing the concept of Graphene Energy Transfer (GET).

Similar to FRET, which relies on dipole-dipole coupling, GET is also based on dipole-dipole interactions. However, the mechanism involves a non-radiative energy transfer from the donor to the graphene surface through energy dissipation either by emission of heat [8,26,27] or phonon or plasmon emission [21] in the conducting plane of graphene. These features lead to several important distinctions between the two mechanisms. First, GET and FRET each have their unique strengths and applications. GET outperforms FRET by providing sub-nanometer axial resolution due to its d^{-4} distance dependence, whereas FRET is limited to pairwise distance measurements with lower scalability. The scalability of GET refers to its ability to interact with multiple emitters simultaneously due to the extended two-dimensional array of acceptors in graphene. This feature differs from the more localized nature of FRET. Unlike FRET, which struggles with dynamic systems and rapid movements, GET enables real-time tracking of biomolecular processes, such as DNA bending and protein diffusion, under physiologically relevant conditions. These advantages make GET a powerful tool for studying complex biological dynamics [22].

From a fundamental perspective, the near-field interactions between an emitter and a purely two-dimensional material are governed by nonradiative energy transfer from an excited dye molecule to graphene (Figure 2.2.) [7], [8], [19], [23]. This mechanism, initially modeled on dipole-dipole interactions by Swathi et al. [19], [23] has been experimentally validated, including accurately determining the characteristic distance (d_0) corresponding to 50% energy transfer to graphene [6], [18], [20].

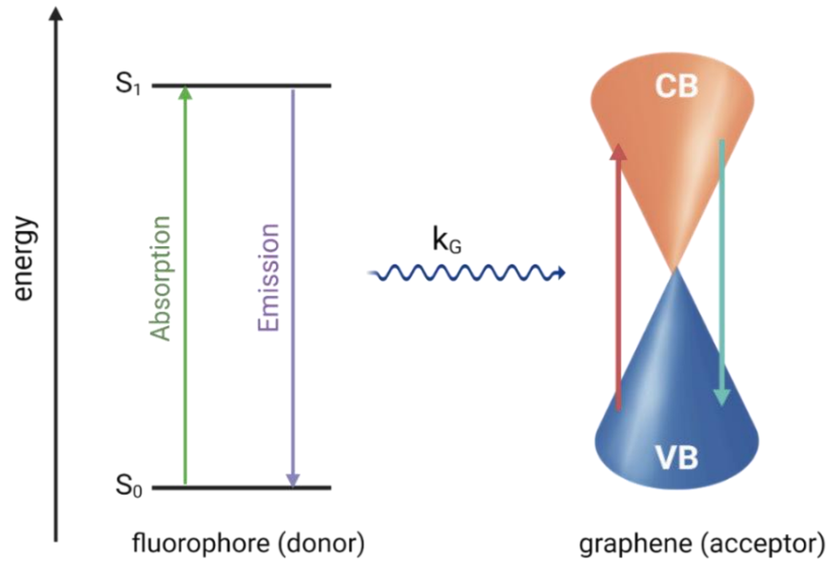

Figure 2.2 Jabłoński diagram of a fluorophore within the GET active range. There are two ways in which an excited molecule can relax to its ground state. Namely, radiatively through the radiative emission or non-radiatively via non-radiative energy transfer to graphene (waved blue arrow). The energy transferred to graphene results in the excitation (red arrow) of the electron from the graphene's valence band (VB) to the conduction band (CB) and then relaxes back to the VB (turquoise arrow). Created with BioRender.com.

Graphene energy transfer efficiency (η) can be quantified by calculating the GET rate constant (k_G) in relation to the total rate constants responsible for depopulating the S_1 state (Eq 2.1). Furthermore, η can be expressed as a function of the dye-graphene distance (d), considering the critical distance d_0, or by using fluorescence lifetimes in the presence of graphene (τ_{Gr}) and on the reference substrate (e.g. glass), where no changes of the fluorescence lifetime occur (τ_{Gl}) as outlined in Eq. 2.1. Alternatively, fluorescence intensities may be utilized instead of fluorescence lifetimes. The energy transfer follows a distance-dependent d^{-4} scaling law, with 50% transfer occurring at approximately 18 nm, allowing for a functional range extending up to 35 nm. Significantly, fluorescence can be restored with a displacement from graphene.

$$\eta = \frac{k_G}{k_{fl} + k_{nr} + k_{ISC} + k_G} = \frac{1}{1 + \left(\frac{d}{d_0}\right)^4} = 1 - \frac{\tau_{Gr}}{\tau_{ref}} \qquad (2.1)$$

As observed, GET shares many similarities with FRET. However, there is a significant difference in the distance dependence between the two processes, which arises from the nature of the energy acceptors. In GET, graphene as the energy acceptor can be represented as a 2D array of dipoles, whereas in FRET, the acceptor is a single, freely rotating dipole. If one exchanges the single acceptor (1D) in FRET with an array of acceptors (2D), the working range and distance dependency will become similar to GET [24].

3 DNA nanomaterials

The previous chapter discusses the unique properties of graphene as a universal fluorescence quencher, particularly its ability to efficiently quench fluorescence through graphene energy transfer. This feature makes graphene an ideal platform for investigating nanoscale interactions and energy transfer processes. However, to fully harness and control GET for precise studies, the spatial arrangement and positioning of fluorophores relative to graphene must be achieved with nanometer-scale accuracy.

DNA nanotechnology offers a powerful solution to address this challenge. DNA's base-pairing and programmable structure provide an unparalleled scaffold for nanoscale manipulation. Beyond its role as a genetic material, DNA can be engineered into complex nanostructures capable of precisely positioning molecules, including fluorophores, in defined spatial arrangements. DNA origami is one of the most advanced techniques in this field, enabling the construction of highly ordered, two- and three-dimensional nanoscale architectures with sub-nanometer precision. By utilizing DNA nanomaterials, we can achieve controlled placement of fluorophores at specific distances from graphene surfaces, enabling accurate GET tracking at the nanometer scale [3], [6], [25], [26].

The following chapter will delve into the fundamentals of DNA nanotechnology, from the basic properties of DNA to the advanced techniques of DNA origami, and demonstrate how these tools can be leveraged to enhance our understanding of energy transfer processes at the nanoscale.

3.1 Deoxyribonucleic acid (DNA)

Deoxyribonucleic acid (DNA) is the primary carrier of genetic information [27], [28]. Structurally, it is a polymer composed of nucleotides consisting of a sugar (deoxyribose), a phosphate group, and a nitrogenous base (a purine or a pyrimidine base). The covalent bond between the sugar and phosphate groups creates what is known as the sugar-phosphate backbone of the single-stranded DNA polymer. DNA strands have directionality, with the 5' end terminating in a phosphate group and the 3' end in a sugar. The sequence of the four nucleobases – adenine (A), cytosine (C), guanine (G), and thymine (T) – encodes genetic information by translating it into amino acid sequences (Figure 3.1).

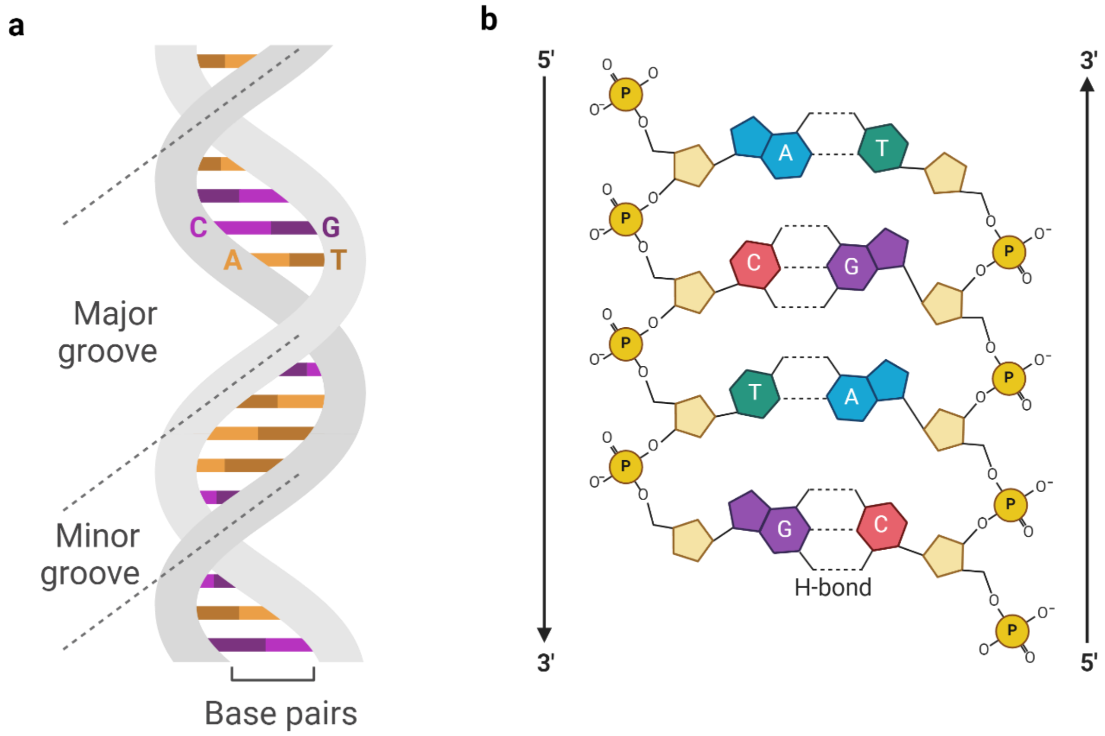

Figure 3.1 (a) Schematic representation of the DNA double helix, highlighting the major and minor grooves as the alternating smaller and larger gaps between two single strands. (b) Chemical structure of DNA, with nucleobases adenine (blue), guanine (purple), thymine (green), and cytosine (red). Dashed lines indicate hydrogen bonding between the strands, leading to the formation of a DNA duplex. Created with BioRender.com.

According to Watson and Crick’s model, the DNA molecule adopts a double helical structure, approximately 2 nm in diameter, where two strands are held together by hydrogen bonds between complementary bases [29]. Adenine pairs with thymine via two hydrogen bonds, while cytosine pairs with guanine via three hydrogen bonds. These base-pairing rules ensure that complementary strands hybridize to form the iconic double helix. Each strand's sugar-phosphate backbone is covalently linked, and the nitrogenous bases project into the center of the helix, forming specific base pairs that maintain the structural integrity of DNA. The purines (A and G) pair with pyrimidines (T and C), following a highly specific bonding pattern, ensuring the fidelity of genetic information during replication and transcription.

3.2 Self-assembly approaches in DNA nanotechnology

As previously discussed, the specificity of DNA base-pairing is the foundation of DNA nanotechnology. By designing specific sequences, DNA strands can be programmed to self-assemble into predetermined structures. Each strand serves as a building block, interacting with others in a highly precisely orchestrated manner. This bottom-up approach, where nanoscale objects self-assemble from individual components, contrasts with top-down methods that are often material-intensive and complex [30], [31]. Both approaches have distinct advantages and limitations.

Bottom-up methods excel in precision and versatility. For instance, DNA origami, a technique where single-stranded DNA is folded into complex three-dimensional shapes using complementary strands, demonstrates the power of self-assembly [32]. Such structures can serve as scaffolds for nanodevices [33], [34], carriers for drug delivery [35], [36] or templates for constructing nanoscale circuits [37], [38]. These approaches generate minimal waste and allow for the creation of highly intricate structures. However, they face challenges in scalability and reproducibility. For example, achieving uniform and defect-free assembly of DNA origami or nanomaterials over large areas remains difficult, limiting their industrial applications [39].

In contrast, top-down methods are well-established and widely used in industries such as semiconductor manufacturing. Photolithography, a prime example, involves using ultraviolet light to etch intricate patterns onto silicon wafers, enabling the production of microchips and integrated circuits. This method allows for the mass production of nanostructures with high precision and scalability, making it indispensable for modern electronics [40], [41], [42]. Similarly, focused ion beam (FIB) milling is a top-down technique that carves nanostructures into materials for applications ranging from nanoscale sensors to biomedical devices [43]. However, these methods often involve material removal, leading to significant waste. For instance, photolithography generates large quantities of chemical byproducts during etching and patterning. The sophisticated equipment and processes required for these techniques also contribute to higher costs and operational complexity [44], [45].

DNA nanotechnology began in the 1980s when Nadrian C. Seeman proposed using DNA to address challenges in protein structure determination [26], [46]. By harnessing DNA's programmable nature, Seeman envisioned nanoscale structures formed from DNA junctions linked by "sticky ends" to create crystalline arrays (Figure 3.2), though early yields were low [25], [26], [46], [47].

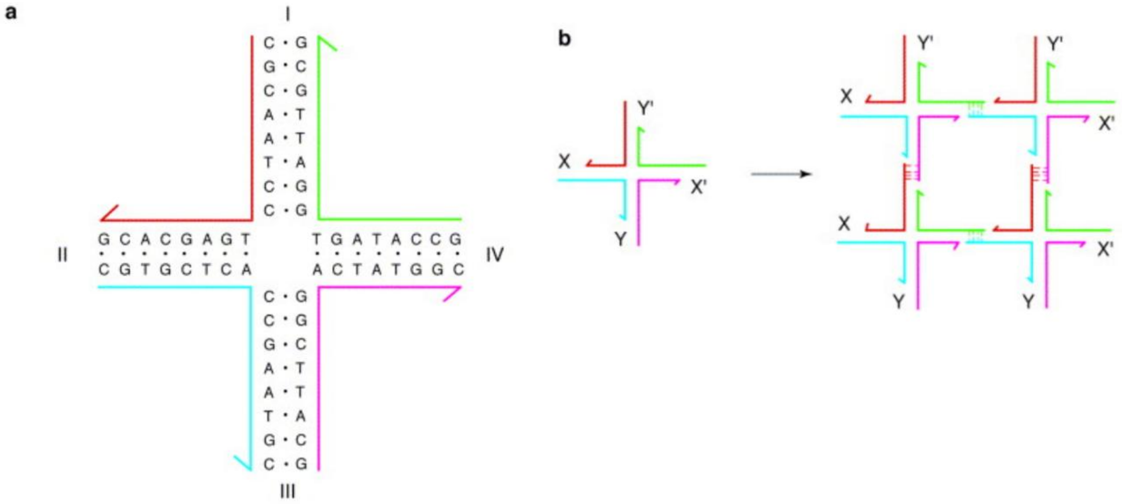

Figure 3.2 (a) A branched DNA molecule with four arms is depicted, with the strands distinguished by different colors. These strands assemble to form four distinct arms, labeled using Roman numerals, and the branch point of the molecule remains fixed. (b) The process of forming a two-dimensional lattice using a four-arm junction with sticky ends is illustrated. The sticky ends, labeled X and Y, pair with their complementary sequences, X' and Y'. Four monomeric junctions on the left align in a parallel orientation to create the structure shown on the right. DNA ligase can seal the remaining gaps in the complex, allowing it to maintain open valences for further extension by adding additional monomers. The dimensions of a DNA double helix are approximately 200 nm wide with a helical repeat of 10–10.6 base pairs, resulting in a pitch of 340–360 nm. Consequently, structures built from DNA exhibit features at the nanometer scale [47].

His work demonstrated DNA's thermodynamic stability and precision for organizing biomolecules. Key advancements included the development of DNA polyhedra, like the DNA cube (Figure 3.3), and double-crossover (DX) molecules (Figure 3.4), which improved structural rigidity, enabling the assembly of robust 2D arrays and substantially advancing the field.

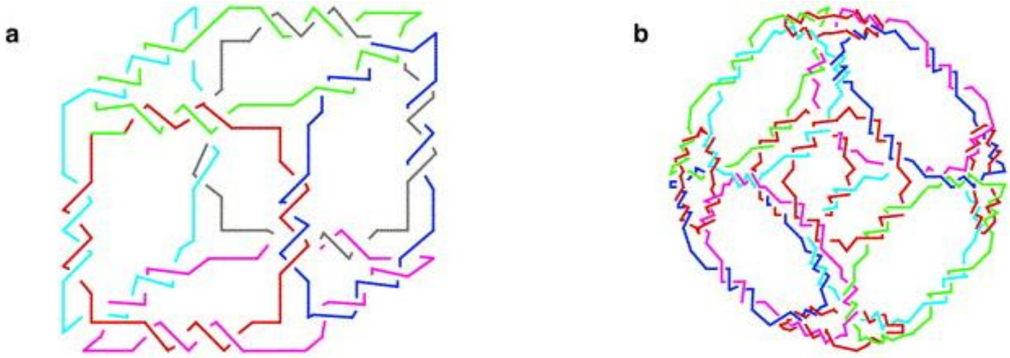

Figure 3.3 Ligated structures derived from flexible DNA components: (a) a cube and (b) a truncated octahedron, with edges composed of two turns of double-helical DNA. To enhance clarity, the twisting is depicted as localized to the central portion of each edge, though, in reality, it spans the entire length from vertex to vertex. Both structures are illustrated as assembled from three-armed junctions; however, the truncated octahedron is formed from four-armed junctions, a detail omitted for simplicity [47].

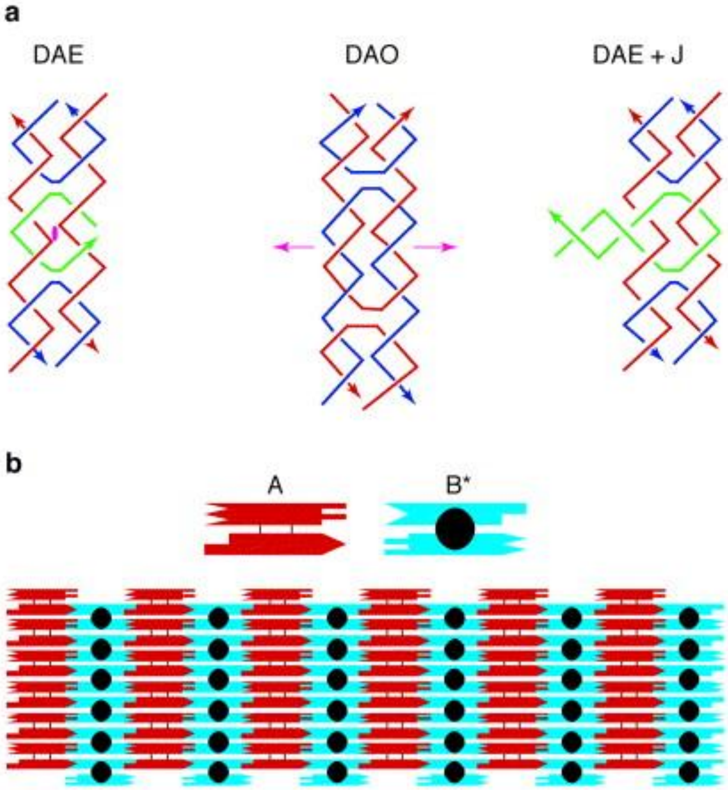

Figure 3.4 Double-crossover (DX) molecules and the arrays formed from them. (a) Two types of antiparallel DX isomers are referred to as DAE and DAO. In DAE, the symmetry axis is perpendicular to the plane of the page, with symmetry disrupted by a nick in the central strand. In DAO, the symmetry axis lies horizontally within the page, with strands of opposite colors (red and blue) exhibiting symmetry. The third structure, DAE1J, is a modified DAE molecule where an additional junction replaces the central nick. (b) Patterned two-dimensional array constructed from DX molecules. (b) At the top, two DX molecules with complementary sticky ends are represented as matching geometrical shapes. Molecule A is a standard DX structure, while B* is a DX1J molecule featuring a DNA hairpin that extends out of the plane formed by the helical axes of its two antiparallel domains. Below these molecules, an array of the two components is depicted, illustrating how they fit together to create a tiled plane [47].

A major breakthrough in the field came in 2006 with the development of Paul Rothemund’s DNA origami technique [32], which has since become a cornerstone of DNA nanotechnology. Given the central role of this method in the present work, Its specifics will be refrained from being delved into at this stage. The technique will be explored in depth in the next chapter (Chapter 3.2.1).

Subsequent innovations led to various DNA tile structures, including triple-crossover (TX) molecules, star motifs, and tensegrity triangles [48]. 2008 Peng Yin introduced a single-stranded tile (SST) approach, where a 42-base DNA strand binds to four local neighbors [49], [50]. This method enabled the creation of complex 2D and 3D shapes, including ribbons, tubes, and intricate structures, through a one-pot annealing process [51]. The SST technique evolved into the DNA brick approach, in which short DNA strands self-assemble into larger architectures. This method has since produced nanostructures with surface features, cavities, and tunnels assembled from thousands of unique components [52]. The beauty that arises from the diversity of DNA folding processes is illustrated in Figure 3.5.

Advancements in DNA synthesis techniques have enabled the precise creation of custom-designed oligonucleotides, facilitating the functionalization of DNA nanostructures with various chemical groups. This precision allows for the accurate positioning of modifications, such as the attachment of proteins, fluorophores, nanoparticles, and lipophilic molecules, with base-pair accuracy and stoichiometric control. The most common approaches rely on incorporating biotin, thiol groups or azide groups into DNA nanostructures.

Biotinylated oligonucleotides can be incorporated into DNA nanostructures to facilitate the attachment of biotin-binding proteins, such as streptavidin. This interaction enables the precise positioning of proteins on DNA scaffolds [53], [54], [55]. Thiol-modified oligonucleotides are commonly used to attach DNA to gold nanoparticles through the strong affinity between thiol groups and gold surfaces. This method creates polyvalent DNA-gold nanoparticle conjugates known as spherical nucleic acids (SNAs). These conjugates exhibit unique chemical and biological properties, making them useful in applications such as intracellular gene regulation and the assembly of nanoparticle superlattices [56], [57], [58]. Moreover, azide groups can be also utilized for the oligonucleotide’s functionalization. They can undergo bioorthogonal reactions, such as the Staudinger ligation or Huisgen cycloaddition ("click chemistry"), to attach various functional groups to DNA nanostructures. These highly specific reactions can occur under physiological conditions, enabling the conjugation of biomolecules without interfering with native biological processes [59], [60].

As a result, DNA nanotechnology has proven to be an effective platform for a wide range of applications, including developing drug delivery systems [61], [62], nanorobots [63], [64], and biosensors [3], [65], [66], [67], [68], [69].

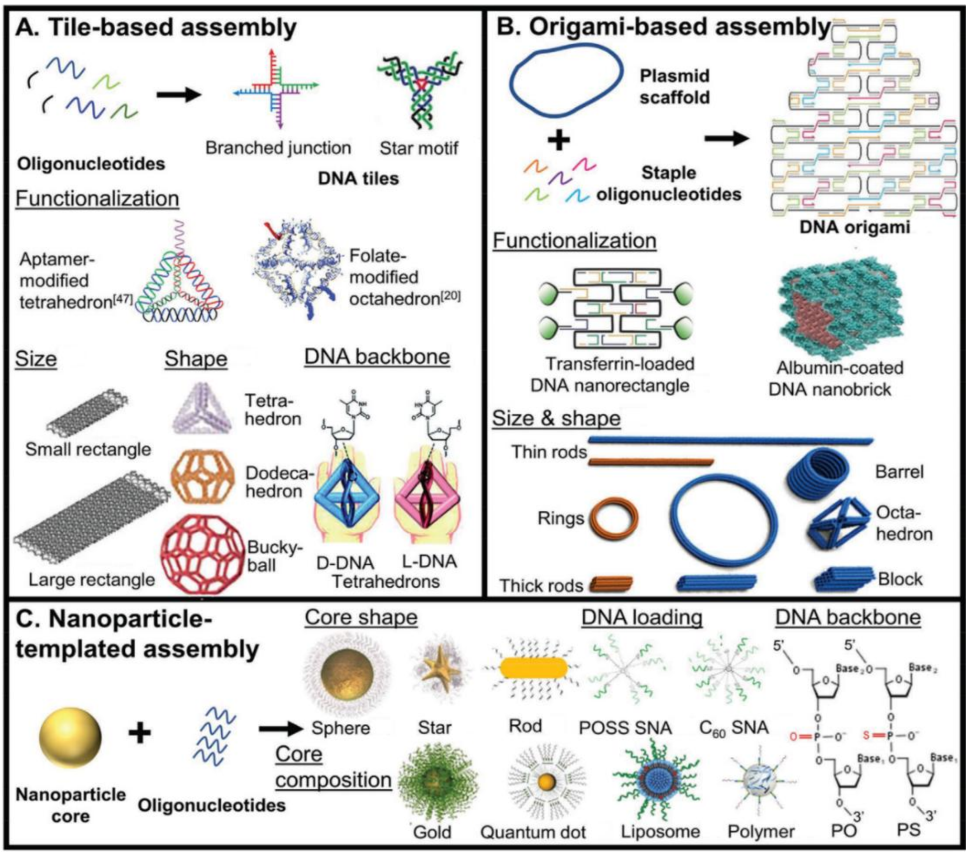

Figure 3.5 Three representative categories of self-assembled DNA nanostructures. A) Tile-based structures: Combining DNA oligonucleotides of varying lengths and concentrations induces the formation of DNA tiles, such as branched junctions and star motifs. These tiles subsequently assemble into geometrically distinct 3D nanostructures of various sizes and shapes, including tetrahedrons and buckyballs. These structures can also be functionalized with biomolecules, such as folate or aptamers. While DNA typically adopts a left-handed (d-DNA) helical configuration, mirror-image right-handed (l-DNA) can also be assembled into nanostructures. B) Origami-based structures: These are constructed by assembling short, specifically designed oligonucleotides (staple strands) with longer DNA (scaffold strands), often derived from plasmid DNA. The resulting origami structures can be tailored in terms of dimensions (2D or 3D), shape, and size by modifying the design of the staple strands and the scaffold. Functionalization with biomolecules, such as albumin for enhanced stability or transferrin for selective targeting of specific cell types, can further improve their properties. C) Nanoparticle-templated structures: Functionalizing the surface of a nanoparticle core with DNA oligonucleotides produces spherical nucleic acids (SNAs). The characteristics of the resulting nanostructures are determined by parameters such as the size and composition of the nanoparticle core and the length and sequence of the DNA oligonucleotides [70].

3.2.1 DNA origami technique

Among the various strategies developed within the field of DNA nanotechnology, one approach that holds particular importance within the scope of this thesis is the construction of nanostructures using the DNA origami technique. This method enables the simultaneous fabrication of billions of DNA origami nanostructures, each potentially designed with a unique configuration. At the heart of this process lies a long single-stranded DNA (ssDNA) molecule, often derived from the genome of the M13 bacteriophage, which serves as a scaffold for constructing these nanostructures (Figure 3.6). The M13 genome, comprising several thousand nucleotides, is hybridized with a series of shorter oligonucleotides, referred to as "staples," typically between 16 and 40 in length. While the M13mp18 bacteriophage genome is frequently used as the scaffold, any sequence of known ssDNA can be adapted for this purpose. These staple strands hybridize to specific regions of the scaffold, forming cross-links between different segments of the DNA, which induces the scaffold to fold into a pre-designed shape (as schematically represented in Figure 3.6).

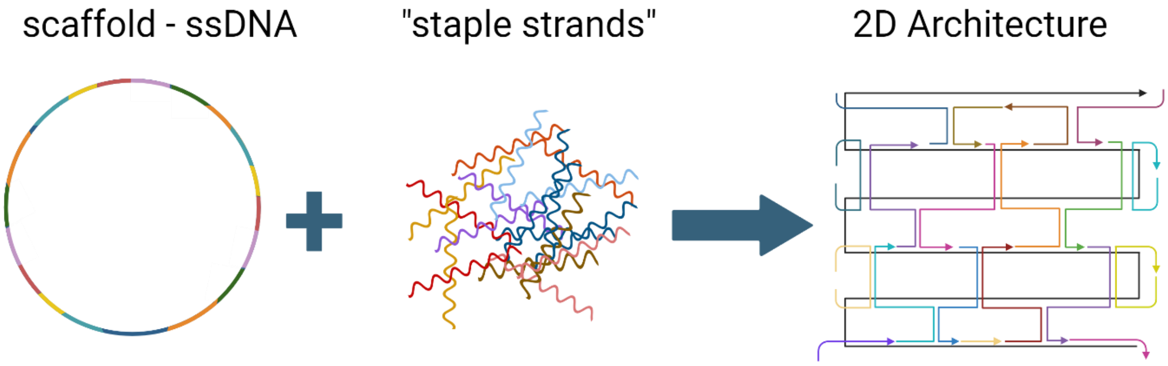

Figure 3.6 Schematic representation of DNA origami folding procedure. A long, single-stranded DNA "scaffold" (left) is combined with numerous short "staple" strands (middle) that bind to specific scaffold regions, folding it into a precise, two-dimensional structure (right). The scaffold sequence, staple lengths, and locations are carefully designed, allowing the formation of custom nanostructures with high spatial resolution. Created with BioRender.com.

This precise folding is governed by the specific sequence and placement of the staples, thereby allowing the same scaffold to be folded into a variety of shapes depending solely on the chosen set of staple strands. As already mentioned, the method was pioneered by Rothemund, who demonstrated the versatility of this technique by producing DNA origami structures in various shapes such as squares, rectangles, stars, and even more intricate designs like a “smiley face,” triangles with rectangular or trapezoidal domains, as illustrated in Figure 3.7.

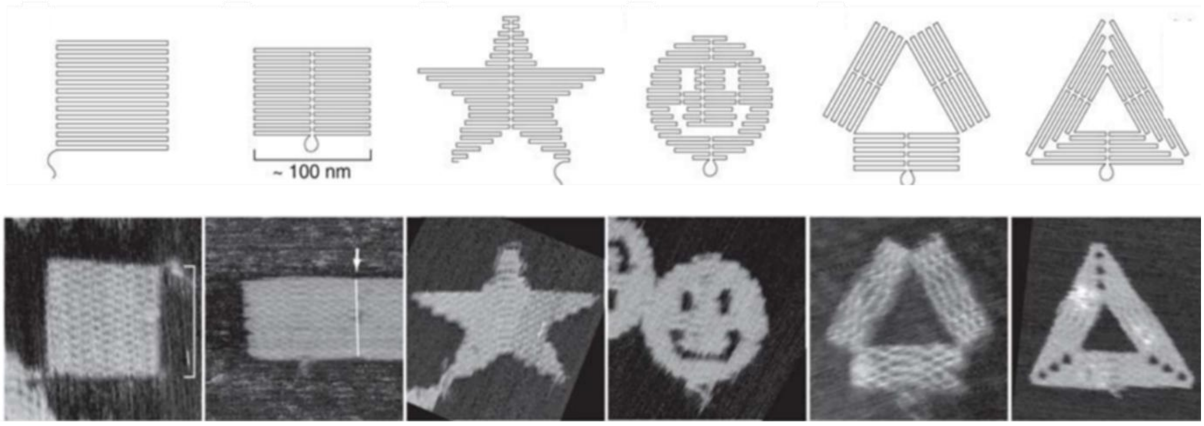

Figure 3.7 DNA origami nanostructures. The top row represents the folding path, and the bottom row represents the AFM images of various shapes as, successively: square, rectangle, star, “smiley face” – disk with three holes, triangle with rectangular domains, and sharp triangle with trapezoidal domains and bridges between them [32].

Two main strategies are employed for constructing 3D DNA origami structures. The first involves packing DNA helices into tightly bundled configurations, creating robust 3D forms (Figure 3.8) [71].

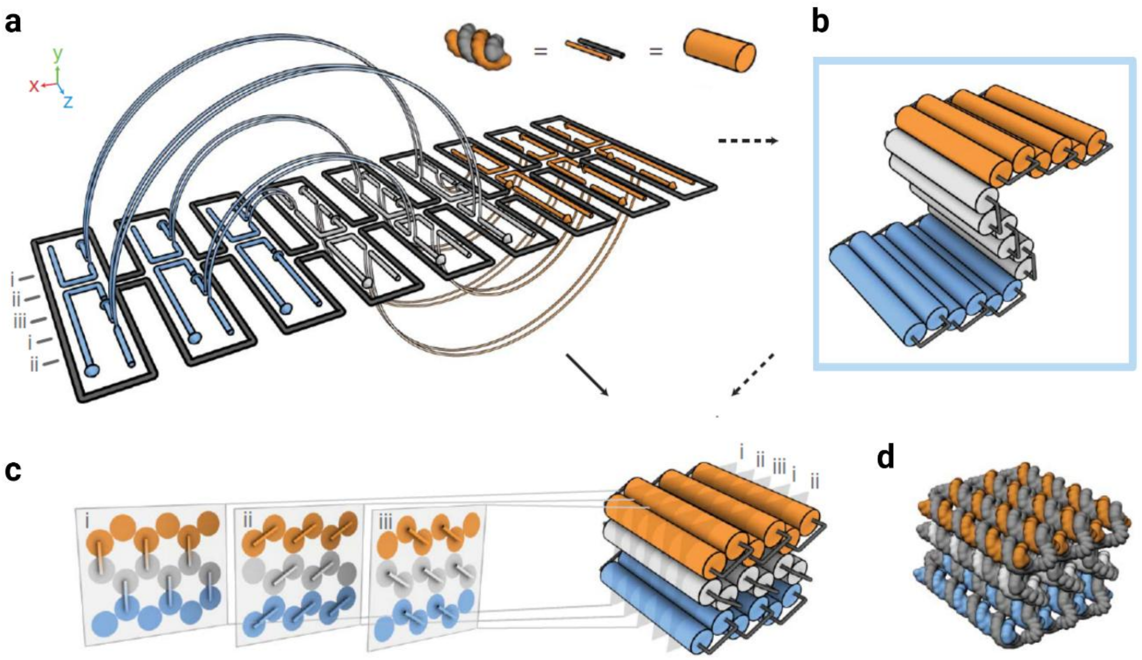

Figure 3.8 Design of three-dimensional DNA origami: (a) The structure is composed of double helices formed by a scaffold strand (grey) and staple strands (orange, white, blue) running parallel to the z-axis. This forms an unrolled, two-dimensional schematic representation of the intended shape. Phosphate linkages create crossovers between adjacent helices, with staple crossovers

bridging different layers, depicted as semicircular arcs. (b). A cylinder model represents a partially rolled intermediate state. In this model, double helices are shown as cylinders, and loops of unpaired scaffold strands connect the ends of adjacent helices. (c) The final folded target shape is illustrated as a cylinder model. The honeycomb-like arrangement of parallel helices is displayed in cross-sectional slices (i–iii) aligned with the x–y plane, spaced at intervals of seven base pairs, repeating every 21 base pairs. All potential staple crossovers are shown in this configuration [71].

In contrast, the second strategy, often called the "flat-pack" approach, involves designing the structure as a two-dimensional (2D) net that folds into a 3D configuration (Figure 3.9) [72].

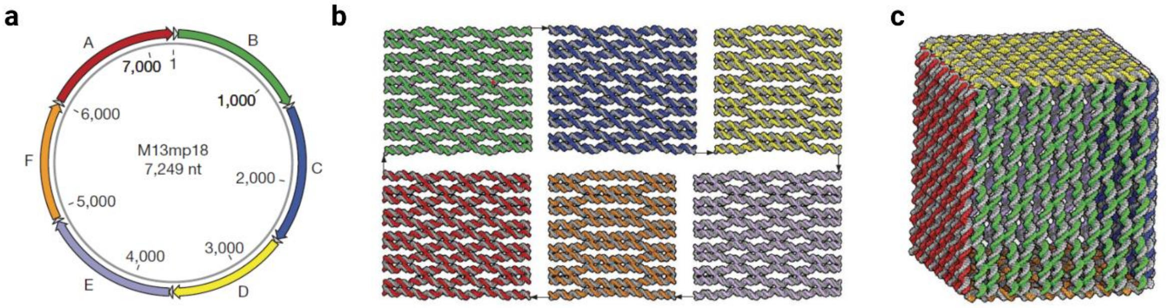

Figure 3.9 Design of a DNA origami box: a. The sequence map of the circular, single-stranded DNA genome of the M13 bacteriophage highlights regions used to fold the six DNA sheets, represented as colored arrows (A–F). Base numbering begins at a 44-nucleotide spacer region between sheets A and B, including a stable hairpin structure. Spacer regions consisting of 33 nucleotides are placed between each sheet. b, c. Molecular models illustrate the six DNA sheets in their flat configuration and the assembled cubic structure. The six sheets are color-coded consistently with the sequence map in part a [72].

One of the most widely used computational tools for designing and implementing DNA origami is caDNAno [73]. This software allows users to arrange DNA helices on a square or a honeycomb lattice, providing the framework to route the scaffold strand between these helices. Although caDNAno automatically generates the staple design based on the user's input, it also provides flexibility for customization, allowing for the modification of the staple pattern to accommodate specialized designs. Importantly, caDNAno adheres to design principles that minimize structural strain by ensuring that the DNA helices cross in a manner that avoids unwanted torsional stress. However, users can intentionally introduce elements such as hairpins, loops, or even mismatches, allowing for further complexity in the structure.

Following the design phase, CanDo (Computer-Aided DNA Origami) [74], [75] is a program that simulates DNA origami's solution structure and mechanical flexibility using finite element analysis [76]. Finite element analysis can simulate the designed DNA origami nanostructure's mechanical properties and solution structure. This tool is particularly valuable for predicting DNA origami's structural stability and flexibility in solution, offering insights into how the nanostructure might behave under experimental conditions.

Each tile or unit within a DNA origami structure can be viewed as an array of addressable "pixels," where each pixel corresponds to a staple strand. This high level of programmability, combined with the numerous techniques available for attaching molecules or particles to DNA, allows each staple to be functionalized with a specific moiety. As a result, DNA origami structures enable the precise positioning of functional elements – such as fluorophores, nanoparticles, or proteins – at sub-nanometer resolution. This feature is particularly important in nanotechnology applications where spatial precision is crucial, such as in developing molecular sensors or nanoscale devices.

4 Interaction between DNA and graphene

The previous chapter describes the fundamental properties of DNA and its potential as a building block for forming highly organized nanostructures. These structures exhibit remarkable potential for nanoscale applications due to their precision and addressability. Among the many fascinating aspects, one of the most intriguing aspects of this work is the interaction between DNA and graphene, which can further be applied in developing advanced tools. DNA nanostructures can serve as highly precise nanopositioners for the spatial arrangement of functional elements, such as fluorophores [77], [78]. Through precise control over the height of fluorophores positioned above the graphene surface, anchored within a DNA origami construct, it becomes possible to establish a calibration curve by correlating fluorescence lifetime with predetermined distances. This calibration enables the detection of variations in fluorescence lifetime from an emitter attached to a dynamic sensing element, which can be accurately translated into changes in distance. This methodology holds substantial promise for advancing applications in biosensing and biophysical research.

The following chapter presents the mechanisms of DNA-graphene interactions, starting with single- and double-stranded DNA. Subsequently, the immobilization of more complex DNA structures on graphene is described along with their usage in experiments at the single-molecule level.

4.1 Adsorption of single- and double-stranded DNA on graphene

Computational approaches, with particular emphasis on methods such as density functional theory (DFT), present the adsorption energies of individual nucleobases, indicating that guanine exhibits the strongest binding affinity to graphene, with the relative binding energies of other nucleobases varying according to the specific computational techniques employed. The adsorption energy hierarchy of DNA nucleobases on surfaces, such as graphene, correlates with their polarizability and follows the trend: guanine > adenine > cytosine ≈ thymine. Guanine, with the highest polarizability, exhibits the strongest adsorption energy, typically around -0.95 eV on graphene. Adenine follows with adsorption energies near -0.75 eV, while cytosine and thymine display lower adsorption energies, approximately -0.70 eV and -0.65

eV, respectively. These values underscore the influence of electronic structure and van der Waals interactions, with guanine forming the most stable interface due to its larger electron cloud and enhanced dispersion interactions. This hierarchy is significant for applications in DNA-2D material systems, such as biosensors, where adsorption strength affects DNA orientation and surface stability. For instance, in graphene-based devices, the stronger interaction of guanine facilitates robust anchoring, whereas thymine and cytosine may be more prone to desorption under similar conditions [79].

The DNA backbone, characterized by its regular sequence of deoxyribose sugars and negatively charged phosphate groups, exhibits different adsorption properties than the nucleobases. As a polymeric molecule, DNA interacts with surfaces through multiple sites along its extended chain, introducing a multivalent adsorption process that can result in a significant sub-additive effect on the overall enthalpy changes. Multiple segments of the DNA molecule simultaneously interact with the graphene surface, contributing incrementally to the total interaction energy. Notably, single-stranded DNA (ssDNA) is highly flexible, with a persistence length of approximately 2 nm, which causes it to adopt a coiled conformation [80]. In contrast, double-stranded DNA (dsDNA) is much more rigid, having a persistence length of around 50 nm [81]. Due to these structural differences, it can be inferred that their interactions with graphene will vary accordingly.

In the adsorption of single-stranded DNA (ssDNA) to graphene, the high affinity highlights the strength of non-covalent interactions between DNA and two-dimensional (2D) materials. In this context, ssDNA primarily interacts with graphene through hydrophobic and van der Waals interactions, with the π–π stacking between the purine and pyrimidine nucleobases and the graphene surface playing a crucial role. Such interactions facilitate the orientation of the hydrophilic sugar-phosphate backbone away from the graphene surface, emphasizing the specificity of these non-covalent forces in guiding DNA orientation [82].

The interactions between graphene and double-stranded DNA (dsDNA) differ significantly from those observed with single-stranded DNA (ssDNA) due to the shielding of nucleobases within the DNA duplex structure. In dsDNA, the nucleobases are paired and stacked internally, minimizing their direct exposure to the surface of graphene or hBN. Studies have demonstrated that the stacked nucleobases within the dsDNA duplex compete with potential π–π stacking interactions on graphene, leading to distinct adsorption behaviors and interaction dynamics. These differences are critical in understanding and leveraging DNA-2D material interfaces for applications in biosensing and nanotechnology [79]. Computational studies have predicted various mechanisms by which dsDNA might interact with graphene, suggesting that the adsorption process is more complex than for ssDNA. Molecular simulations conducted by Zeng et al. [83] revealed that dsDNA, in contrast to ssDNA, tends to rotate and orient itself perpendicularly to the graphene surface, thereby reducing the contact area between the molecule and the surface, consequently diminishing the interaction strength. This vertical orientation of dsDNA suggests that its affinity for graphene is lower than that of ssDNA. However, it is important to note that these simulations did not account for certain external factors such as pH, ionic strength, hydrogen bonding, and the length of the DNA strands, which may all significantly influence the observed binding affinity [84], [85].

While computational models provide valuable predictions, experimental validation and consideration of external factors remain essential for fully elucidating the complex nature of these interactions. The experiments indicated that ssDNA adsorbs to graphene faster than dsDNA, with shorter DNA strands exhibiting even more rapid adsorption due to weaker electrostatic repulsion [84], [85]. This pattern is consistent for both ssDNA and dsDNA, underscoring the kinetic differences in their adsorption behaviors [86].

The observed disparity in adsorption kinetics can be attributed to the distinct structural characteristics of ssDNA and dsDNA. The reduced accessibility of the nucleobases in dsDNA leads to a lower adsorption affinity when compared to ssDNA. This difference in binding affinity between ssDNA and dsDNA has emerged as a critical factor in the development of advanced sequencing devices [87] and sensing platforms, where the ability to discriminate between ssDNA and dsDNA is essential for optimizing sensor performance [88], [89], [90], [91].

The interactions of both ssDNA and dsDNA with graphene offer significant possibilities, each with its strengths and limitations. In both cases, the same fundamental interactions anchor the structures onto graphene. DNA nanostructures, such as DNA origami, provide additional advantages due to their well-defined, highly programmable architecture. These advantages enable the creation of more advanced systems, including those tailored for specific applications, which are not achievable with ssDNA or dsDNA alone. While DNA origami excels in structural precision, Szalai et al. have demonstrated a level of sensitivity with ssDNA and dsDNA systems that surpasses the sensitivity of DNA origami [92]. This highlights the complementary nature of these approaches and underscores the need to explore their distinct capabilities further.

This thesis focuses mainly on nanostructures formed using the DNA origami technique (described in detail in Chapter 3.2.1), especially in the fluorescence studies at the single-molecule level. While most experiments combining 2D materials and fluorophores have been conducted using bulk (ensemble) spectroscopy, the single-molecule research provides a much deeper understanding of the studied systems as individual molecules are analyzed independently (the single-molecule approach is discussed in Chapter 5). This approach eliminates averaging and detects even minor heterogeneities within the system that might otherwise be overlooked in ensemble studies [51], [93], [94], [95], [96], [97], [98], [99].

5 Single-molecule fluorescence studies

This chapter outlines the fundamental principles of single-molecule studies, emphasizing their importance in achieving high-resolution analysis. It covers the core concepts of fluorescence confocal microscopy, the primary technique utilized throughout this thesis. The chapter then explores the role of graphene energy transfer (GET) in monitoring signal fluctuations from individual fluorescent molecules. Lastly, the immobilization of DNA origami nanostructures on graphene surfaces is discussed, showcasing the exceptional potential of these systems for single-molecule fluorescence experiments.

Single-molecule microscopy and spectroscopy (SMS) represent a powerful suite of techniques that enable the detection and characterization of individual molecules with exceptional sensitivity [94], [100], [101]. SMS provides unique insights into molecular behaviors often obscured in ensemble measurements by directly observing single molecules rather than averaging over large populations. These techniques are widely applied in fields like biophysics, material science, molecular biology, nanotechnology, and chemistry, where understanding molecular heterogeneity and dynamic processes at the nanoscale is crucial. The core principle of single-molecule microscopy is to observe and analyze the behavior of individual molecules with high spatial and temporal resolution. This is achieved by limiting the excitation volume to a small region, ideally containing only one molecule within the probe volume 104]. In contrast to traditional ensemble methods, which measure the average response of thousands or millions of molecules, single-molecule techniques isolate the response of individual molecules. This eliminates ensemble averaging and allows for constructing histograms of measured parameters, revealing the underlying distribution of behaviors. Such detailed analysis is fundamental when studying heterogeneous systems, such as biological tissues, polymers, or amorphous materials, where each molecule may experience a unique local environment. Single molecules can act as local reporters, sensitive to their immediate surroundings, including functional groups, electrostatic fields, and nearby atoms or ions.

Despite their advantages, single-molecule techniques come with several limitations. The most significant challenge is the low signal intensity from a single molecule, making it susceptible to background noise and requiring sophisticated detection systems. Photobleaching is another major drawback, as it limits the observation time of individual molecules. The molecule may transition into non-fluorescent states, further complicating data acquisition. Detecting a single molecule requires carefully optimizing the experimental setup to maximize signal while minimizing noise. The key challenge is to achieve a signal-to-noise ratio (SNR) greater than one, ensuring the molecular signal can be distinguished from background noise [94], [101]. Several factors influence the signal strength, including the molecule's absorption cross-section, photostability, and fluorescence quantum efficiency. A small focal volume and effective rejection of Rayleigh and Raman scattering are crucial in maximizing signal while limiting background interference. A significant limitation of single-molecule studies is the sensitivity to noise. Background photons from the environment, optical components, and even the excitation laser can degrade the signal. Moreover, single-molecule experiments are highly sensitive to environmental conditions, requiring precise control over temperature, humidity, and the chemical environment. For example, the buffer conditions in biological systems must be carefully optimized to maintain molecular function without introducing artifacts.

In fluorescence-based single-molecule studies, particular attention must be given to the photophysical properties of the fluorescent label, such as the molecule's tendency to enter non-emissive states, which can reduce the overall fluorescence yield. Additionally, photobleaching, where a molecule loses its ability to fluoresce over time, can limit the duration of observation [105].

Overcoming undesired phenomena such as photobleaching and the formation of non-emissive states, including triplet states, is crucial for enhancing fluorescence yield and extending observation times. Strategies to address these issues have significantly improved the accuracy and longevity of fluorescence signals.

Redox-based buffer systems are widely employed to mitigate photobleaching. These buffers, incorporating reducing and oxidizing agents such as ascorbic acid and methyl viologen, stabilize fluorophores by maintaining them emissive, effectively minimizing photobleaching and fluorescence blinking. Additionally, self-healing dyes, achieved by covalently attaching intramolecular triplet-state quenchers to fluorophores, provide a robust solution. This approach suppresses non-emissive states directly within the fluorophore, enhancing photostability without external additives [102], [103].

Eliminating non-emissive states, particularly triplet states, can also be achieved through tailored buffer formulations. Additives like Trolox are effective triplet-state quenchers that reduce the population of these states, thereby improving fluorescence yield. Furthermore, optimizing excitation parameters, such as adjusting intensity and wavelength, minimizes the likelihood of fluorophores entering non-emissive states, contributing to a more consistent and reliable fluorescence signal [104], [105], [106], [107].

Single-molecule microscopy employs various imaging techniques, broadly categorized into scanning and wide-field approaches. These methodologies differ in their imaging mechanisms, probe volumes, and applications, offering distinct advantages and limitations.

Wide-field techniques illuminate a large area simultaneously and capture images using sensitive cameras, such as charge-coupled devices (CCDs). Among wide-field methods, wide-field fluorescence microscopy is the most basic, enabling simultaneous observation of multiple molecules. However, this approach often suffers from increased background noise and limited temporal resolution due to the larger probe volume [108], [109].

To address these limitations, Total Internal Reflection Fluorescence (TIRF) microscopy has emerged as a specialized wide-field technique. By exploiting the evanescent wave generated at the interface of two media with different refractive indices, TIRF restricts excitation to molecules near the surface, significantly reducing background noise and improving signal-to-noise ratio. This makes TIRF particularly valuable for studying molecular dynamics at or near cell membranes. Another advancement within wide-field approaches is super-resolution microscopy, which includes techniques like Stochastic Optical Reconstruction Microscopy (STORM) and Photoactivated Localization Microscopy (PALM). These methods overcome the diffraction limit of conventional optical microscopy, achieving nanometer-scale resolution and enabling the visualization of molecular structures in unprecedented detail [114].

On the other hand, scanning techniques involve localized excitation and sequential sample scanning to construct an image. Confocal Laser Scanning Microscopy (CLSM) is a widely used method in this category. CLSM provides high spatial resolution and depth selectivity by using a pinhole to reject out-of-focus light, making it ideal for three-dimensional imaging of thick specimens [110], [111]. Near-field Scanning Optical Microscopy (NSOM) is a more specialized scanning approach that uses a sub-wavelength-sized probe to achieve resolutions beyond the diffraction limit. NSOM enables imaging and spectroscopic analysis at the nanoscale, offering unique insights into molecular and surface phenomena [112], [113].

Each of these techniques contributes unique capabilities to the field of single-molecule microscopy, and their selection depends on the specific requirements of the experiment, such as resolution, imaging depth, or the need to minimize background noise. The diversity of available methods ensures that researchers can tailor their approaches to achieve optimal results in their molecular behavior and interactions studies.

In this thesis, special attention is devoted to confocal microscopy. Despite high sensitivity due to their small illumination volume and high temporal resolution, the primary reason for employing confocal fluorescence microscopy in this work is the use of Time-Correlated Single Photon Counting (TCSPC), as fluorescence lifetime is the key parameter being measured. While wide-field techniques could also be used for fluorescence lifetime measurements, confocal microscopy remains advantageous. It should be noted that there are now wide-field approaches with cameras capable of measuring fluorescence lifetimes, such as those offered in specialized systems like the Widefield FLIM Bundle by PicoQuant. However, these systems are generally more expensive and less common. As a core technique of this thesis, fluorescence confocal microscopy is described in greater detail in the following chapter.

5.1 Fluorescence confocal microscope

Confocal microscopy is a powerful technique for high-resolution imaging and single-molecule studies. In this method, a laser is focused on a single spot within the sample, and emitted fluorescence is collected through a pinhole, which rejects out-of-focus light, significantly improving the signal-to-background ratio. This approach (Figure 5.1) enables precise spatial resolution by detecting light exclusively from the focal plane.

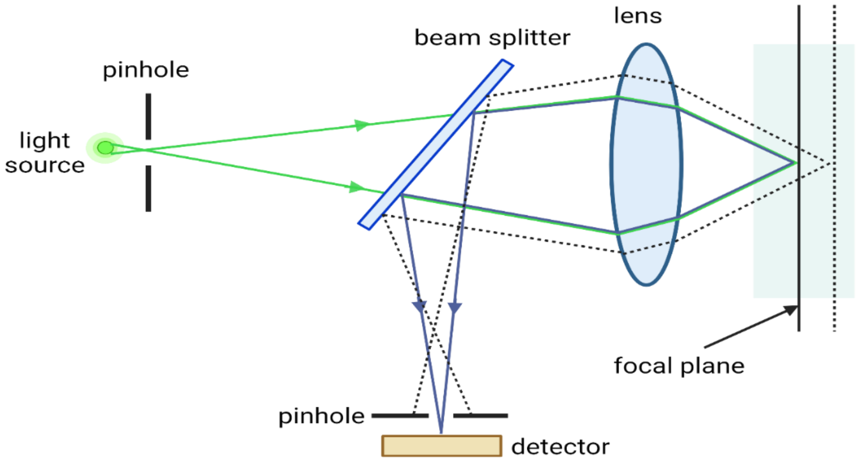

Figure 5.1 Sketch illustrating the concept of confocal microscopy. Only light originating from structures near the focal plane is detected. Created with BioRender.com.

The confocal microscope can be applied for both solution-based and surface-based measurements. In solution, molecules diffuse through the focal volume, producing single bursts of fluorescence as they pass through [114].

In surface-based measurements, the sample surface is scanned in a raster pattern, generating an image on a point-by-point basis. Moreover, confocal microscopy can be coupled with time-correlated single photon counting (TCSPC) to measure fluorescence lifetimes [109]. In this case, a pulsed laser excites the sample, and the time delay between excitation and photon detection is recorded. This allows the analysis of fluorescence decay curves and the extraction of individual molecule lifetimes.

The image formed by a point source through a lens is characterized by the Airy disk, and the achievable lateral resolution is limited by the diffraction of light, as described by the Rayleigh criterion:

$$\Delta x = \frac{0.61\lambda}{NA} \tag{5.1}$$

Where:

- NA is the numerical aperture of the objective lens,
- λ is the wavelength of light.

The numerical aperture (NA) is given by:

$$NA = n \cdot \sin(\alpha) \tag{5.2}$$

Where:

- n is the refractive index of the transmission medium,
- α is the half-opening angle of the objective.

The Rayleigh criterion specifies the minimum distance between two-point emitters at which they remain distinguishable by the microscope. This is achieved when the maximum of the Airy disk of the first emitter coincides with the first minimum of the second emitter. A high NA objective enhances signal collection and reduces background noise, significantly improving the performance of the confocal microscope.

This increased light-gathering ability enables higher spatial precision, essential for confocal microscopy. Additionally, a higher NA results in a more minor, more tightly focused light spot, enhancing the system's ability to resolve fine details. This tighter focus also helps minimize background light from regions outside the focal plane, improving image quality. Another crucial component in maximizing the signal is the size of the pinhole, which determines the depth of field. The pinhole size is crucial in improving axial resolution by excluding out-of-focus fluorescence.

A confocal image is typically generated by raster scanning the sample stage beneath the laser spot, often using a piezo-electric stage for precise movement. The stage must have sufficient resolution for single-molecule studies to remain precisely positioned on individual molecules. High-resolution confocal imaging allows for detailed observation of single-molecule dynamics, such as fluorescence fluctuations, which are critical for studying molecular interactions and behaviors at the nanoscale.

5.2 Graphene in single-molecule measurements

Building on the significance of single-molecule studies, graphene’s potential in this field emerges as a groundbreaking tool. By leveraging graphene energy transfer (GET), it is possible to track fluorescent signals from single-molecule fluorophores with unprecedented precision. As described in Chapter 2.1, graphene acts as a highly distant-dependent, unbleachable, universal fluorescent quencher.

Utilizing graphene for studies of energy transfer from single emitters is a relatively young area of research. The first experimental evidence of highly efficient energy transfer from quantum dots (QDs) to graphene was reported in 2010 [7]. This pioneering study revealed a remarkable 70-fold fluorescence quenching of QDs when placed on graphene. Additionally, they observed significant alterations in the blinking behavior of QDs and an increase in energy transfer efficiency with the number of graphene layers. A few years later, Koppens and coworkers extended this work by experimentally validating the theoretically predicted d^{-4} scaling of the energy transfer rate to graphene (Figure 5.2) [21], [24].

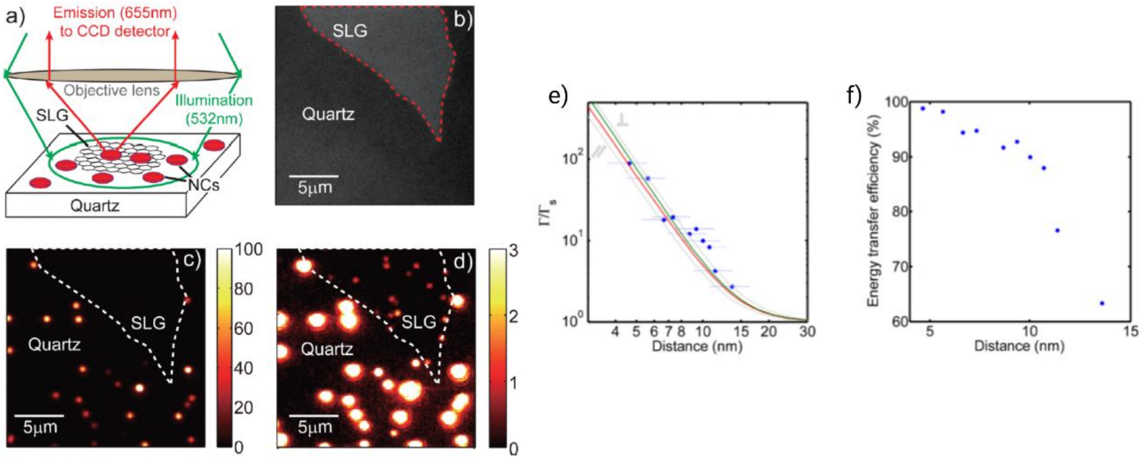

Figure 5.2 (a) Schematic of the experimental setup, (b) optical image of the nanocrystals’ emission range, (c) wide-field fluorescence image of individual CdSe/ZnS nanocrystals (color scale: photon count over the 30s), (d) same as (c) but with a 30x reduced color scale to emphasize emission from nanocrystals on the graphene monolayer [7]. (e) Decay rate enhancement ($\Gamma/\Gamma s$) obtained from the lifetime measurements as a function of distance, (f) energy transfer efficiency as a function of distance [20].

These findings demonstrated for ensemble samples were later corroborated in experiments involving single emitters, solidifying the understanding of this interaction [18], [115]. In the experiments described above, emitters were separated from graphene by a layer of oxide that played the role of a spacer, which positioned fluorophores within the active range of GET without complete fluorescence quenching (as seen with direct deposition of single emitters on graphene). While this approach enabled controlled interactions, it introduced several limitations. Spacer thickness requires precise measurement before experiments, and such spacers are not suitable for placing more complex objects and biomolecular assays at a well-defined distance from graphene. These challenges had broader implications. Despite a solid theoretical understanding of GET, the experimental tools for accurately examining distance dependence across the full range of graphene-emitter interactions were limited. Consequently, the d0 value (distance of 50% quenching efficiency, more details in Chapter 2.1.) remained inconsistent across studies [7], [18], [116]. This lack of consistency hindered the development of sensitive, reliable devices and ultraprecise position or distance measurement systems.

5.3 Immobilization of DNA origami on graphene

To overcome the limitations outlined above, a spacer that is highly addressable, reproducible, and capable of precisely placing molecules, such as fluorescent markers, is essential. As discussed in Chapter 3.2.1, DNA, particularly DNA origami nanostructures, has emerged as a promising candidate to meet these criteria. Harnessing the full potential of DNA origami requires controlled and reproducible immobilization on the graphene surface while preserving the stability, integrity, and intrinsic properties of both the DNA origami nanostructures and graphene.

The most straightforward approach of directly depositing DNA origami nanostructures onto graphene has been shown to lead to distortion of the nanostructures [117], [118], [119]. This distortion is likely due to strong stacking interactions between the DNA bases and the hexagonal lattice of graphene. To mitigate this issue, specific molecular linkers facilitate either non-covalent or covalent interactions between the DNA nanostructures and the graphene surface. Among these, pyrene stands out as a significant non-covalent connector, particularly for interfacing graphene with biomolecules. The pyrene moiety interacts with graphene via π–π stacking interactions, enabling the attachment of biomolecules while preserving the structural and electronic properties of both DNA origami nanostructures and graphene [6]. This approach prevents the distortion of

DNA origami nanostructures caused by direct DNA-graphene interactions. In the case of graphene, hydrophobic interactions often play a dominant role in mediating biomolecule binding. Non-covalent functionalization approaches, such as those involving pyrene linkers, enable specific and reversible positioning of DNA nanostructures without compromising the graphene's lattice structure or significantly altering its electronic properties, maintaining the pristine nature of the graphene surface [120], [121].

Alternatively, covalent functionalization techniques offer a more permanent method for attaching DNA nanostructures to graphene [122], [123], [124]. By forming site-specific chemical bonds between the nanostructure and the graphene surface, covalent approaches provide enhanced chemical stability and resistance to environmental fluctuations. However, these methods may introduce defects into the graphene lattice, potentially affecting its electronic properties. Therefore, selecting the appropriate functionalization method requires a careful balance between achieving chemical stability and preserving the intrinsic characteristics of the 2D material. In conclusion, both non-covalent and covalent immobilization techniques offer distinct advantages, and the optimal choice will depend on the specific requirements of the system under study.

5.3.1 GET determination at the single-molecule level

Building upon the successful immobilization of DNA origami nanostructures on graphene without altering their intrinsic properties, the precision and versatility of this system can be further leveraged to study nanoscale energy transfer dynamics.

Pyrene molecules, previously mentioned as universal linkers, facilitated the attachment of DNA origami constructs to graphene [6]. Pyrene molecules were incorporated within DNA origami nanostructures via external labeling (DNA hybridization). This immobilization approach ensured the stable positioning of various DNA origami geometries, enabling precise and adjustable placement of single fluorescent molecules relative to the graphene surface. Utilizing this precise control, the distance-dependent energy transfer from single dye molecules to graphene was systematically investigated. DNA origami nanostructures of various shapes were selected to position a single dye molecule (ATTO 542) at predetermined heights relative to the graphene surface, covering a range of distances from 3 nm to 53 nm. Three distinct DNA origami geometries were utilized: rectangular (NR), disc-shaped (ND), and pillar-shaped (NP). These geometries allowed precise placement of dye molecules at defined heights, specifically 3 nm (NR), 7 nm (ND), 12 nm (NP1), 16 nm (NP2), 24 nm (NP3), and 53 nm (NP4), as schematically depicted in Figure 5.3.

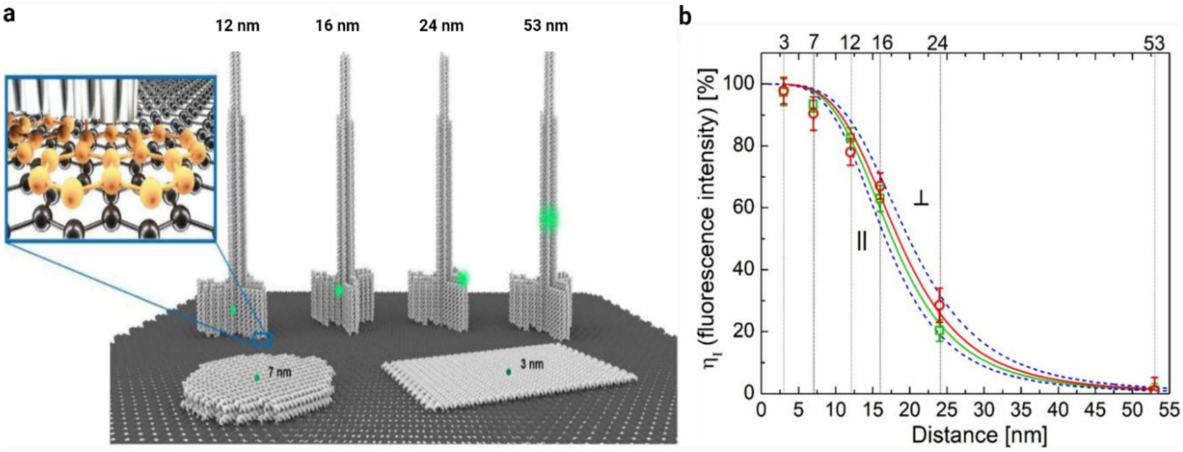

Figure 5.3 (a) Schematic representations of DNA origami structures, each incorporating a single ATTO 542 fluorophore (depicted as a green sphere) positioned at varying heights, ranging from 3 nm to 53 nm. The inset, highlighted by a blue frame, provides a magnified view of a pyrene-modified DNA strand (in orange), protruding from the DNA origami and interacting with graphene via non-covalent interactions. (b) The mean excitation energy transfer efficiency, derived from fluorescence intensity measurements, is plotted as a function of the distance between the dye molecules (ATTO 647N in red and ATTO 542 in green) and the graphene surface. The fitted curves (red and green lines) illustrate the energy transfer efficiency as a function of the separation distance between the graphene and the emitters. The blue dashed lines represent theoretical predictions based on a semiclassical model for point-dipole emitters oriented either parallel (||) or perpendicular (⊥) to the graphene plane [6].

These distances encompass the range over which energy transfer from a dye to graphene can vary from 0% to nearly 100%. The pyrene-based immobilization of DNA origami nanostructures on graphene enabled the precise positioning of fluorescent dyes at specific distances, confirming the d^{-4} dependence of energy transfer and determining the 50% transfer distance (d_0) to be 17.7 nm ± 0.5 nm for a green dye molecule and 18.5 ± 0.7 nm for a red dye molecule. The homogeneity in the resulting populations demonstrates that the dye-to-graphene distance can be measured with high precision, particularly in the 5–30 nm range, across the visible spectrum.

6 Beyond monolayer graphene-based platforms

The preceding chapters examined the energy transfer mechanism between a fluorophore and monolayer graphene, highlighting how proximity to the graphene surface influences the efficiency of excitation energy transfer. The introduction of additional graphene layers, however, can significantly alter these energy transfer properties. As the system transitions from monolayer to bilayer, trilayer, and even multilayer graphene, the electronic and optical properties of graphene evolve, leading to changes in energy transfer dynamics. Building on this foundation, the following chapter will examine how varying the number of graphene layers modulates the energy transfer range.

6.1 Multilayer graphene

The unique electronic, optical, and mechanical properties of graphene have driven extensive research into both single-layer and multilayer forms. Unlike monolayer graphene, which exhibits a well-defined set of properties (as long as the high quality of the sample is conserved), multilayer graphene offers a broader and more tunable range of characteristics influenced by the number of layers, stacking order, and sample quality. To unlock its full potential for advanced electronics, photonics, and materials science applications, the controlled synthesis of multilayer graphene with precise layer numbers and minimal structural defects is essential. Achieving this level of precision demands a careful selection of fabrication methods, as the performance of the multilayered structure is intrinsically linked to its structural quality.

6.1.1 Methods for multilayer graphene preparation

This chapter begins by outlining various fabrication techniques for multilayer graphene, offering a comparative analysis of their capabilities, limitations, and typical applications. Following this overview, the discussion centers on the layer-by-layer assembly method, highlighting the rationale for its selection in this work and its advantages in producing high-quality, customizable multilayer graphene samples. This discussion underscores the critical relationship between the fabrication method and the resulting sample quality. It emphasizes that the reliable study of multilayer graphene properties necessitates meticulous control over its synthesis.

Among the most prominent methods developed to prepare multilayer graphene are chemical vapor deposition (CVD), mechanical exfoliation, liquid phase exfoliation, epitaxial growth on silicon carbide (SiC), and electrochemical exfoliation [125]. These techniques vary in their ability to control the number of layers, scalability, and quality of the resulting graphene, making certain methods more suitable for specific applications. A comparative summary of the most commonly used methods is provided in Table 1.

Table 1. Comparison of the multilayer graphene preparation techniques.

Method	Layer control	Quality	Scalability	Customization of stacking
Chemical Vapor Deposition (CVD) [126], [127], [128] - carbon-containing gases (like methane or acetylene) decompose on a heated metal substrate (often copper or nickel) to form graphene. After cooling, carbon atoms precipitate onto the surface, forming graphene layers.	moderate	very high	moderate	limited
Mechanical exfoliation[129] [130], [131] - peeling thin graphene layers from bulk graphite using adhesive tape (the “Scotch tape” method). One can reduce graphite to thin graphene flakes by repeatedly applying and removing the tape.	low	very high	low	limited
Liquid phase exfoliation [132], [133], [134], [135] - Graphene production from graphite typically involves several steps to facilitate layer separation. Graphite is first oxidized using chemical agents (e.g., Hummers' method) to introduce oxygen-containing functional groups, weakening the interlayer forces and forming graphite oxide. This material is then exfoliated into graphene oxide (GO) sheets through sonication or	moderate	moderate	high	low

mechanical stirring in a solvent. To restore conductivity and other properties, the GO is reduced to reduced graphene oxide (rGO) using chemical, thermal, or electrochemical methods. Centrifugation is often applied to separate graphene layers by thickness, ensuring the desired material quality.				
Epitaxial Growth on SiC [136], [137], [138] **-** heating a SiC crystal at high temperatures in a vacuum or inert atmosphere causes silicon atoms to sublimate, leaving behind carbon atoms that rearrange to form graphene layers.	high	very high	low	Limited
Electrochemical exfoliation [139], [140] **-** graphite is placed in an electrolyte solution, and an electrical potential is applied. The intercalation of ions (often involving ionic liquid or aqueous solutions) separates the layers, exfoliating the graphite into multilayer graphene.	moderate	moderate	moderate	low

While each method for multilayer graphene preparation offers distinct advantages, many face limitations when precise control over the layer structure is required. Chemical vapor deposition (CVD) and epitaxial growth can produce large-area multilayer graphene with high structural integrity. However, achieving the exact number of layers and uniform distribution across an entire sample remains challenging. Similarly, although scalable, exfoliation-based methods often result in inconsistent layer thickness and require further processing to improve homogeneity, which can introduce defects and compromise sample quality. Given the objectives of this study – specifically, the need for simplicity in multilayer formation, precise control over the number of graphene layers, and high uniformity across a sample area on the order of a few square millimeters (the areas scanned during measurements are much smaller, usually limited to a few hundred micrometers by a few hundred micrometers) – a more controlled and adaptable approach is essential.

The layer-by-layer (LbL) assembly method was selected to address these requirements. By enabling the sequential addition of monolayer graphene sheets, the LbL approach offers excellent control over the layer number and stacking arrangement, ensuring the desired multilayer structure with minimal variation across the sample. Its simplicity and adaptability make it particularly suitable for research applications where customizability and quality are paramount. Through LbL assembly, a high degree of uniformity can be achieved, providing a reliable foundation for the detailed investigation of multilayer graphene's unique properties.

6.1.2 Properties modulation in graphene via layer control

Graphene exhibits notable layer-dependent variations in its key properties – electronic [141], [142], optical [143], [144], mechanical [145], [146], and thermal [147], [148], [149] – as the number of layers increases. As this thesis primarily focuses on the optical properties of graphene, this chapter provides an in-depth discussion of how the number of graphene layers influences these optical characteristics, with particular emphasis on absorbance, transparency, band structure, and light-matter interactions.

The optical properties of graphene undergo significant transformations as the number of layers increases. Due to its unique electronic structure, single-layer graphene absorbs about 2.3% of incident light across the visible spectrum. As additional layers are added, the absorbance increases linearly up to approximately 10 layers, with each layer contributing an additional 2.3% absorption. Each added layer contributes diminishing increments in absorbance, gradually reducing transparency [17]. Moreover, optical conductivity and refractive index increase proportionally upon increasing the number of layers, enhancing interaction with electromagnetic waves. This rise in conductivity and refractive index enables effective light modulation, offering improved control over reflection, refraction, and phase-shifting [150]. Notably, the band structure of graphene also transforms significantly with added layers. Monolayer graphene exhibits a gapless Dirac cone structure. In contrast, bilayer graphene can develop a tunable bandgap (up to ~250 meV) influenced by the application of an external electric field, expanding its use in electronic and optoelectronic applications. With additional layers, the structure shifts toward graphite-like properties, narrowing the bandgap and increasing the density of states. These changes modify the optical response, making multilayer graphene suitable for applications like photodetectors and optical modulators that benefit from a tailored band gap [141], [151]. The tunability of graphene’s bandgap with increasing layers significantly affects its energy transfer properties, particularly in how it absorbs, transfers, and interacts with photons and charge carriers such as electrons and holes. The subsequent chapter thoroughly explores these effects, focusing on the relationship between the number of layers and GET.

6.2 GET of multilayer graphene

As mentioned before, graphene exhibits metallic-like behavior, while bilayer graphene, in contrast, possesses semiconducting characteristics with a tunable bandgap [152]. When introducing a third layer, the system's complexity increases further [153], [154], reflecting the intricate nature of multilayer graphene structures. As discussed in Chapter 2.1, the theoretical model describing graphene-mediated energy transfer (GET) in monolayer systems is well-established and closely matches experimental results. However, theoretical expressions that account for the influence of multiple graphene layers on the energy transfer rate remain notably less accurate.

Experimental investigations into this subject reveal that one of the most significant factors influencing the rate of energy transfer is the dielectric function at the emission wavelength of the dipole [8]. For instance, studies on energy transfer from quantum dots (QD) to graphene layers of varying thickness (monolayer, bilayer, and bulk with 12 layers) demonstrate that as the number of graphene layers increases from monolayer to bulk, the decay rate of the donor also increases. This suggests that non-radiative energy transfer becomes more dominant as the graphene thickness increases. In contrast, the effect of electric field screening, which could potentially reduce the energy transfer rate constant, plays a minor role.

Since the interactions between adjacent graphene layers are relatively weak [7], and we are primarily focused on the excitations in the visible spectral range, we can approximate the few-layer graphene (FLG) system as a stack of decoupled single-layer graphene sheets. In this approximation, each graphene layer acts as an independent energy transfer channel, separated by the characteristic interlayer spacing of graphite, approximately 0.34 nm. The dielectric screening effect from the upper layers of FLG is assumed to remain similar to that of the nanocrystal ligands, which are organic or inorganic molecules capping the surface of nanocrystals to stabilize them and control their surface properties. Consequently, the quenching factor for an FLG system with n layers is given by:

$$\rho\,(n\mathrm{L}) = \frac{\pi}{16}\frac{\alpha}{\varepsilon^{5/2}}\left(\frac{c}{v_F}\right)^4 \sum_{i=1}^{n} I(z_i) + 1 \tag{6.1}$$

In this model, the distance from the center of the nanocrystal to the i-th graphene layer is defined as:

$$\mathrm{z}_i = z_1 + (\mathrm{i}-1)\cdot 0.34\,nm \tag{6.2}$$

While experimental results are consistent with the dipole theory, as presented in Equation 6.1, and confirm that the quenching process can be attributed to resonant energy transfer rather than electron transfer, a discrepancy remains between the theoretical quenching factor for few-layer graphene and the experimental data. Specifically, the theoretical model fails to accurately describe multilayer graphene systems with more than three layers [7].

This work attempts to define further the influence of the number of graphene layers on GET. The experimental part of the thesis presents the results obtained in this project and the proposed model describing these relationships.

6.3 Van der Waals heterostructures

Building on the foundation of multilayer graphene systems, the broader potential of 2D platforms (beyond monolayer graphene) can be explored. The previous chapter examined how additional graphene layers influence energy transfer, focusing on the nuances of multilayer formation and their impact on graphene’s electronic properties. In the following chapter, the scope has been expanded by introducing van der Waals heterostructures, which are composite structures formed by stacking two-dimensional (2D) materials in layers held together by weak, non-covalent van der Waals forces [155]. Unlike conventional heterostructures that rely on strong chemical bonds at the interface, these structures utilize naturally weak interlayer bonding, enabling the assembly of diverse materials without requiring lattice matching or chemical compatibility. This versatility allows for the design of heterostructures with specific electronic, optical, or thermal properties by combining layers of different materials in novel configurations [156].

Graphene plays a central role in van der Waals heterostructures due to its extraordinary electronic, optical, and mechanical properties, which can be further tailored by combining it with other 2D materials. Notably, graphene’s pairing with hexagonal boron nitride (hBN) has emerged as an area of particular interest, owing to hBN's complementary properties. Unlike other 2D materials, hBN has a similar lattice structure to graphene, minimizing lattice mismatch while preserving each material’s intrinsic properties. Moreover, hBN is an excellent insulator with a wide bandgap and minimal light absorption, making it an ideal dielectric substrate for graphene. These characteristics reduce unwanted charge traps and enhance graphene’s optical properties, making graphene/hBN heterostructures especially suitable for high-resolution optical and fluorescence studies.

This thesis focuses on graphene and hBN heterostructures, exploring their combined properties and their application in fluorescence studies at the single-molecule level. This pairing leverages the structural compatibility and complementary properties of graphene and hBN, demonstrating their potential in advancing fluorescence-based research and applications.

6.3.1 Hexagonal boron nitride

Hexagonal boron nitride (hBN) shares a nearly identical crystal structure with graphene (as presented in Figure 6.1), differing in lattice constant by only approximately 2% [157], [158]. Often referred to as "white graphene," a single layer of hBN consists of alternating boron and nitrogen atoms arranged in a honeycomb pattern, resulting in an atomically smooth surface. In multilayer hBN, these layers are bonded through weak van der Waals forces, preserving the integrity of each layer’s properties. Unlike graphene, however, hBN is an excellent dielectric material with a substantial bandgap of about 5.9 eV, distinguishing it as an insulator with unique optoelectronic characteristics [157], [158].

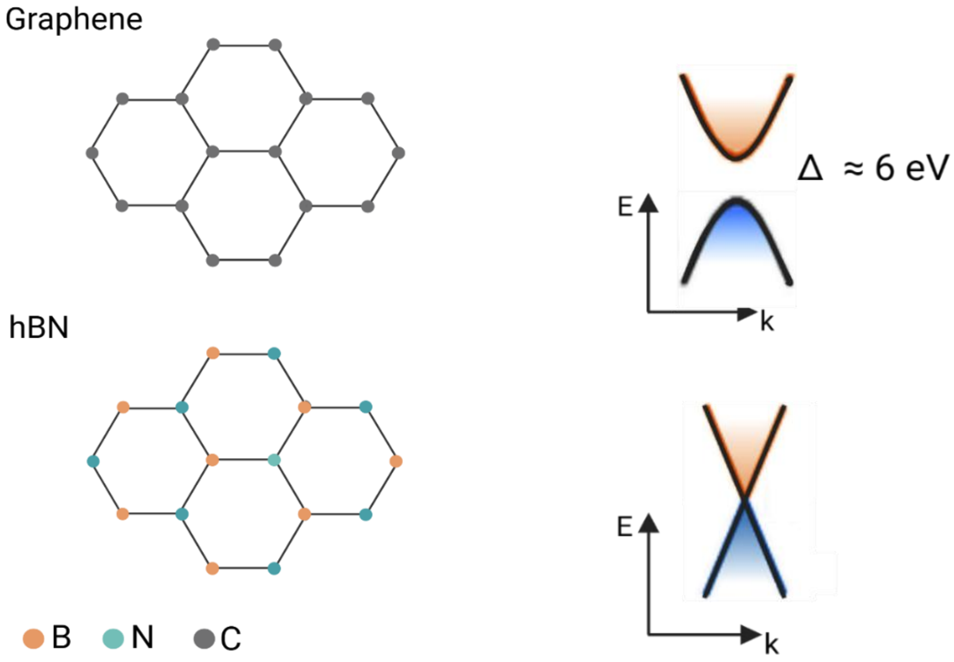

Figure 6.1 Left panel: Graphene and hBN lattices, right panel: the schematic band structures of graphene and hBN [159].

In addition to its electronic properties, hBN exhibits remarkable mechanical and chemical stability, high thermal conductivity, and optical activity in the deep ultraviolet range, where it displays several distinct absorption bands and intense luminescence peaks [88], [157], [160]. This structural, thermal, and optical combination makes hBN a versatile material for advanced applications in optoelectronics, photoelectric devices, and field-effect transistors [161].

Similar to graphene, hBN can be synthesized through mechanical exfoliation, chemical vapor deposition (CVD), or various solvent-based techniques, with the method of preparation tailored to achieve the desired quality, flake size, and application-specific properties [88].

The distinctive optoelectronic and dielectric properties of hBN, coupled with its compatibility with graphene, have led to its growing popularity in the design of layered heterostructures. In particular, heterostructures composed of hBN and graphene benefit from the complementary properties of each material, providing a versatile platform for applications in electronics, photonics, and nanotechnology [157].

6.3.2 Graphene/hBN heterostructure

Combining graphene with hBN offers numerous advantages, including enhanced electronic properties and thermal management. Various strategies have been developed for such combinations, such as creating heterostructures and hybrid materials. [162], [163]. One of the most established approaches involves using hBN as a substrate for graphene [162], [164], [165], [166], or, conversely, applying hBN as a protective layer over graphene [167], [168]. Additionally, graphene can be encapsulated between two hBN layers to preserve its intrinsic properties [168], [169], [170]. Alternatively, both materials can be patterned and deposited on a single substrate. In this latter approach, lithographically patterned hBN serves as a template for graphene growth, resulting in in-plane heterostructures with precisely controlled domain sizes [169].

Using hBN as a substrate offers several advantages over conventional materials like SiO_2, including its atomically smooth surface, free of dangling bonds and charge traps, its close lattice match with graphene, and its sizeable electrical bandgap. These characteristics contribute significantly to enhanced performance in graphene devices. Carrier mobility is improved by nearly an order of magnitude compared to graphene on SiO_2 substrates, while surface roughness and intrinsic doping are substantially reduced. Furthermore, studies indicate that the optical properties of graphene in the visible and near-infrared (NIR) regions remain largely unaffected by the presence of hBN, underscoring hBN’s compatibility with graphene for optical applications [162], [164].

Using atomically thin hBN layers on top of graphene in heterostructures has demonstrated synergistic benefits, especially in surface-enhanced Raman spectroscopy (SERS). This configuration preserves graphene’s electronic properties, as electrons can tunnel through the thin hBN layer while enhancing SERS sensitivity due to graphene’s interaction with analyte molecules [168]. In addition, hBN protects both graphene and any underlying silver nanoparticles from oxidation, enabling the regeneration of the SERS substrate through simple heat treatment.

The integration of graphene and hBN has garnered significant interest, particularly in optoelectronics and photonics. This is primarily due to hBN’s role as a wide-bandgap dielectric, which enables interesting optical behavior in the ultraviolet (UV) range and is an ideal substrate that enhances graphene’s electronic properties. Moreover, hBN enables band structure engineering in graphene and offers protective encapsulation without altering graphene’s optical characteristics.

Recent studies have extended the potential applications of graphene/hBN heterostructures, proposing their use in investigating biomolecules such as DNA and proteins [164], [170], [171], [172]. For instance, Dean et al. (2010) [164] and Kretinin et al. (2014) [170] explored the exceptional electronic and thermal properties of graphene/hBN interfaces, laying the groundwork for their use in sensitive detection platforms. More recent works, such as those by Sülzle et al. (2024) [171] and Yang et al. (2024) [172], have specifically demonstrated the feasibility of using these heterostructures for single-molecule analysis and biosensing. These studies highlight the potential of graphene/hBN heterostructures as stable, high-performance platforms at the atomic scale. A detailed discussion of their implications for biosensing applications is provided in the following chapter.

Based on the discussion of graphene and hBN heterostructures, the focus now turns to another crucial component of this thesis: the interactions between hBN and DNA. These interactions are particularly interesting given the study’s focus on the systems based on graphene and DNA nanostructures. This chapter delves into the underlying mechanisms of hBN-DNA interactions.

6.3.3 Exploration of hBN-DNA Interactions

As outlined in Chapter 6.3.1, graphene and hexagonal boron nitride (hBN) share a similar crystal structure and exhibit unique interactions with biomolecules, rendering them highly attractive for biosensing applications. Despite these structural similarities, hBN demonstrates distinct adsorption behaviors. While interactions with pristine graphene are predominantly governed by physisorption, the binding of DNA strands to hBN is more complex. Initially mediated by van der Waals forces, electrostatic forces further influence these interactions. The surface of hBN is polar, displays a non-uniform charge distribution, and is chemically inert. Lin et al. [173] reported that nucleobase interactions with hBN are predominantly driven by mutual polarization. Consequently, it is unsurprising that hBN interacts more strongly with purine bases, particularly guanine, than pyrimidines. Furthermore, the functionalization of hBN through nucleobase adsorption has been observed to alter the bandgap of this two-dimensional material, as noted by the authors.

Zhang and Wang [174] investigated the interfacial interactions between hBN and nucleobases, concluding that hBN exhibits superior sensitivity to nucleobases compared to graphene, enabling effective nucleotide discrimination. Studies on in-plane graphene – hBN heterostructures [175], [176] provide compelling evidence that ssDNA preferentially adheres to hBN domains over graphene due to stronger van der Waals attractions [177]. These experimental findings align with computational predictions [178].

The interaction between hBN and dsDNA exhibits similarities to graphene, with notable distinctions. Specifically, hBN's affinity for ssDNA differs significantly from its interactions with dsDNA. Zhan et al. [179] exploited these differences for fluorescence-based sensing. In their experiments, ssDNA labeled with X-rhodamine (ROX) was strongly adsorbed onto the hBN surface through π–π stacking and other interactions, effectively quenching the fluorescence of the dye molecule. Upon hybridization with complementary DNA strands, the weakened hBN–DNA interaction led to fluorescence restoration, a phenomenon corroborated by other studies [180], [181].

Although the interaction between dsDNA and hBN is weaker than that with ssDNA, mathematical modeling by Alshehri et al. suggests that hBN's interaction strength surpasses that of other widely studied two-dimensional materials, such as graphene, MoS_2, and WS_2. Computational studies have further demonstrated that ssDNA lies flat on graphene surfaces with an interaction energy of approximately -23 kcal mol^{-1} per nucleotide, increasing to -29 kcal mol^{-1} per nucleotide on hBN [175]. The boron atoms within hBN play a pivotal role in aligning nucleobases, explaining its higher affinity for DNA than graphene. This high affinity has been leveraged in nanopore sequencing, where the strong interactions with hBN slow DNA translocation, providing sufficient time resolution for sequencing [173], [182].

The interactions of graphene and hBN with dsDNA differ markedly from those with ssDNA, as the nucleobases are shielded within the DNA duplex. Studies have shown that stacking nucleobases within dsDNA compete with π–π stacking interactions on graphene surfaces [183], [184]. While such differential affinities between ssDNA and dsDNA are common across two-dimensional materials, the underlying mechanisms and the degree of interaction contrast vary significantly depending on the material system. This highlights graphene and hBN's unique opportunities in tailoring biomolecule interactions for specific applications. The detailed exploration of these mechanisms forms the foundation for the subsequent chapters, which delve deeper into the interplay between 2D materials, their interactions with DNA, and practical applications.

Materials and methods

This chapter provides an overview of the methodologies employed in this research. It details the procedures for sample preparation, followed by an in-depth discussion of the microscopy and spectroscopy techniques utilized throughout the experiments. Each method is described along with the rationale behind its selection and its relevance to the research objectives.

1. Graphene-on-glass coverslip preparation

To fully exploit the exceptional properties of graphene, it is crucial to recognize that the quality of the samples plays a pivotal role. Attaining the optimal characteristics of this carbon allotrope strongly depends on the precision and integrity of the material's preparation. This chapter details the process of transferring graphene from a copper foil substrate to a glass coverslip and the subsequent cleaning procedures to ensure effective residue removal. Several approaches to the transfer procedure described in the literature [185], [186], [187], [188] have been evaluated. The experiments conducted at the single-molecule level demonstrated the highest sensitivity in assessing graphene quality. Even samples initially considered defect-free and clean failed to meet the stringent "single-molecule grade" quality criteria. Optimizing an effective protocol proved challenging, and the final optimized method is detailed below, as outlined in a previous study [4].

Monolayer graphene grown on the copper substrate via chemical vapor deposition (CVD) and covered with poly (methyl methacrylate) (PMMA) on top was purchased from Graphenea® and ACS Material®. The wet-transfer approach was employed for graphene transfer onto glass coverslips (Figure 7.1) [4]. All glass coverslips were cleaned by sonicating in 50 ˚C, in 1 % aqueous solution of Hellmanex (Hellma®), and then twice in MilliQ water, each step for 15 minutes. Small pieces of graphene, approximately 0.25 cm², were cautiously cut from the PMMA/Gr/Cu foil. The samples were floating in the 0.2 M ammonium persulfate solution to remove the copper substrate for approximately 4 hours. The cleaned coverslip was then vertically submerged, aligned with the PMMA/Gr layer, and slowly raised to lift the graphene onto the coverslip. The sample was subsequently rinsed twice in MilliQ water to eliminate residual ammonium persulfate.

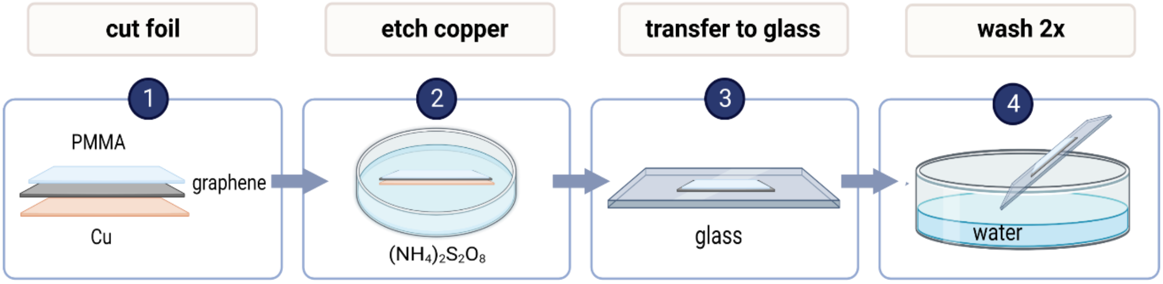

Figure 7.1 Schematic representation of the wet-transfer approach of graphene onto the glass coverslip. Created with BioRender.com.

Before the removal of the PMMA layer (Figure 7.2), an additional layer of PMMA (M_w = 120,000 g/mol), dissolved in chlorobenzene (50 mg/mL), was drop-cast onto the existing PMMA/Gr layer. This process facilitated the re-dissolution of the dried PMMA, thereby relaxing the underlying graphene monolayer and improving its adhesion to the substrate. After 30 minutes, the PMMA/Gr-coated glass was subjected to sequential immersion in fresh acetone (twice, for 5-10 minutes each) and subsequently in toluene (5-10 minutes). Following the second acetone and toluene treatment, the samples were gently dried using a nitrogen stream. Finally, they were placed on activated charcoal, heated on a hot plate at 230 °C for 8 hours, and allowed to cool gradually.

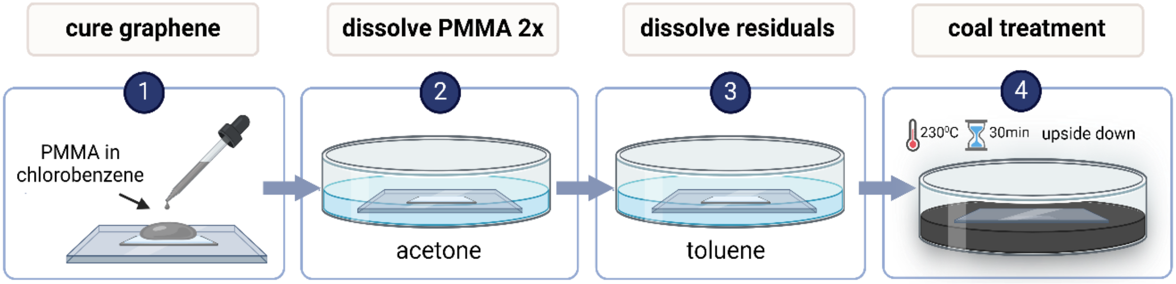

Figure 7.2 Schematic representation of the protocol of PMMA removal. Created with BioRender.com.

2 DNA Origami Production

2.1 Buffer and recipes

If no other company is mentioned, chemicals were purchased from Sigma Aldrich.

Table 2 The list of buffers with recipes.

	Recipe
FOB20	20 mM $MgCl_2 \cdot 6H_2O$ 20 mM Tris base 20 mM acetic acid 1 mM EDTA-$Na_2 \cdot 2\ H_2O$
FOB12.5	12.5 mM $MgCl_2 \cdot 6H_2O$ 20 mM Tris base 20 mM acetic acid 1 mM EDTA-$Na_2 \cdot 2\ H_2O$
PCA/Trolox12	2 mM Trolox (6-hydroxy-2,5,7,8-tetramethylchroman-2-carboxylic acid) 25 mM PCA (protocatechuic acid) 12 mM $MgCl_2 \cdot 6H_2O$ 40 mM Tris base 20 mM acetic acid 1 mM EDTA-$Na_2 \cdot 2H_2O$
50× PCD	2.8 mM PCD (protocatechuate 3,4-dioxygenase from pseudomonas sp.) 50% glycerol 50 mM KCl 100 mM Tris HCl 1 mM EDTA-$Na_2 \cdot 2H_2O$
TAE-Mg^{2+}	40 mM Tris base, 20 mM acetic acid, 1 mM EDTA, 12.5 mM $MgCl_2$, pH 8.0

Among different DNA origami nanostructures, the most stable and best-examined pillar-shaped DNA origami nanostructure (Table 2) was applied for the experiments. DNA origami nanostructures used in the thesis were designed in caDNAno and employed the p8064 as a scaffold derived from M13mp18 bacteriophages. DNA origami structures were folded with a 10-fold excess of unmodified and internally labeled oligonucleotides (from Integrated DNA Technologies, biomers.net GmbH, and Eurofins Scientific) along with a 100-fold excess of biotinylated or pyrene-modified oligonucleotides in comparison to the scaffold in 1× FOB20 buffer. In this study, DNA origami nanostructures were folded using a thermocycler to achieve precise temperature control during the annealing process. The mixture was first heated to 65°C for 15 minutes to denature secondary structures and ensure all DNA strands were fully single-stranded. Following this denaturation step, the temperature was gradually decreased to 25°C over 12 hours. This slow cooling allowed the staple strands to hybridize with the scaffold strand at their designated positions, enabling the correct folding of the DNA origami nanostructures [189].

Alternatively, single-stranded extensions were employed for DNA origami immobilization on graphene. The DNA origami structures were assembled by mixing the scaffold strand (e.g., M13mp18) with an excess of ssDNA-modified staples (rich in guanine and adenine bases) in a folding buffer (1× TAE with 12.5 mM $MgCl_2$). The mixture was subjected to thermal annealing, starting at 95°C for 2 minutes, and gradually cooled to room temperature over 12 hours.

Some of the oligonucleotides carried chemical moieties to introduce modifications and were added at 30× excess. The mixture contained 10 mM Tris, 1 mM EDTA, and 14 mM $MgCl_2$. The mixture was heated to 96°C, and a temperature ramp to slowly cool down was driven to induce a stepwise hybridization of the oligonucleotides with the scaffold until the structures were folded into the desired shape.

Following the folding process, the sample was purified via agarose gel electrophoresis. First, 1× Blue Juice gel loading buffer was added to the DNA origami solution. Then, 1.5% agarose gel was prepared in 50 mL of FOB12.5 buffer containing peqGREEN (VWR) at a concentration of 2 µL per 100 µL of buffer. Electrophoresis was conducted at 70 V for 1.5 hours, allowing the DNA nanostructures to migrate and separate based on size and folding state. After electrophoresis, the gel was visualized under UV or blue light to identify the band corresponding to the correctly folded DNA origami nanostructures. This band was excised carefully using a clean scalpel, and the DNA was recovered using a gel extraction method, such as electroelution or passive diffusion, into FOB12.5 buffer. If necessary, the purified DNA origami nanostructures were subsequently concentrated by ultrafiltration or ethanol precipitation. Finally, the samples were prepared for experimental use and stored at -20°C to maintain structural integrity and prevent degradation.

Before deposition onto glass or graphene substrates, the concentration of the purified DNA origami solution was adjusted to 50 pM using FOB12.5 buffer. The spatial positions and separations of dye molecules within the DNA origami nanostructures were estimated based on the assumed inter-nucleotide distance of 0.34 nm along the DNA double helix and an inter-helical spacing of 2.7 nm within the square lattice arrangement, as described in previous studies [190], [191]. Deviations from these calculated values may result from minor bending or tilting of the DNA origami nanostructures [192]. Additionally, differences between the designed and experimentally determined distances could be influenced by the specific nanostructure geometry, dye molecule-DNA interactions, and the salt concentration used during preparation.

2.2 DNA sequences

The DNA oligonucleotides sequenced used within this thesis are listed in the tables below (Appendix, Tables 3 – 7).

2.3 Hybrid DNA

DNA oligonucleotides were obtained from biomers.net GmbH, Germany (Biomers), and Integrated DNA Technologies, Inc., USA (IDT). A complete list of the oligonucleotides used, along with their respective suppliers, is provided in Table 8

Table 8 The sequences of the DNA oligonucleotides used in the study

Name	Sequences (5' to 3')	Supplier	Description
51 mer ATTO 542	[ATTO 542]TAACCACCGTGTACTCGT TATTCGATCCGATCAGTCCGTCGTA GCCAGTTC	Biomers	Labeled strand for hybrid 51 bp dsDNA
136 mer	ACGGTCGTCAAATCTGTCGTGGTAG GATCTGTCGTGGTAGGATCTGTCGT GGTAACTTTGGGGTTGGATAAATCT ACAGTCTTAAGAACTGGCTACGACG GACTGATCGGATCGAATAACGAGTA CACGGTGGTTA	IDT	Unlabeled strand, complementary to 51 bp

To prepare the hybrid system, single-stranded DNA strands were purified using 8 M urea polyacrylamide gel electrophoresis (PAGE) for 1 hour at 100 V (current ranging from 15 to 8 mA) in 1× TBE buffer. Post-electrophoresis, gels were illuminated with a UV lamp at 254 nm (Analytik Jena GmbH + Co. KG, Germany) to visualize the bands, which were subsequently excised. The gel fragments were finely chopped, incubated in 400 µL of elution buffer, and frozen at –20 °C. The solution was then agitated for 3 hours, and gel debris was removed using a Spin-X filter (Favorgen Biotech Corp., Austria) by centrifugation at 10,000 g for 2 minutes at room temperature. An additional 100 µL of elution buffer was added to the gel debris, and the centrifugation step was repeated under the same conditions. The ssDNA strands were desalted via dialysis and concentrated using a 3K Amicon Ultra Filter (Merck Millipore, Merck KGaA, Germany) to achieve a concentration of 1 µM or higher. DNA quantification was performed by measuring UV absorbance at 260 nm or the absorbance specific to the fluorescent dye using a spectrophotometer (Thermo Scientific NanoDrop 2000, Thermo Fisher Scientific Inc., USA). For final visualization of the purified DNA strands, samples were loaded onto a polyacrylamide gel in 1× TBE buffer, electrophoresed for 60 minutes at 100 V, and stained with Sybr™ Gold (Invitrogen, Thermo Fisher Scientific Inc., USA). Throughout the purification process, ssDNA strands labeled with a fluorescent dye were handled separately from unlabeled strands.

For graphene and/or hexagonal boron nitride experiments, ssDNA strands were annealed to their respective reverse complementary strands by mixing both in a

1× TAE buffer solution. The mixing utilized a tenfold excess of the longer ssDNA strand, which served as a toehold on graphene. Following premixing, the solution was incubated on a thermomixer (Eppendorf ThermoMixer® C, Germany) at 37 °C with shaking at 300 rpm for 2 hours to facilitate the formation of double-stranded DNA (dsDNA).

3 Confocal microscopy

Single-molecule experiments were conducted using a custom-built optical setup schematically presented in Figure 8.1. The system includes a pulsed supercontinuum laser source, spectral selection components, and spatial and spectral filtering to ensure precise wavelength control and beam quality. Depending on the specimen's requirements, 532 nm (green) wavelengths and 639 nm (red) were alternately used. The filtered beam was directed into the microscope, which focused on the sample through an objective lens, and fluorescence was detected using an array of avalanche photodiodes (APDs). This setup enabled the acquisition of single-molecule intensity maps and time-correlated single-photon counting (TCSPC) data. Further details on the modifications and optimization of this setup, undertaken as part of this thesis, are provided in Chapter 1 of the Results section.

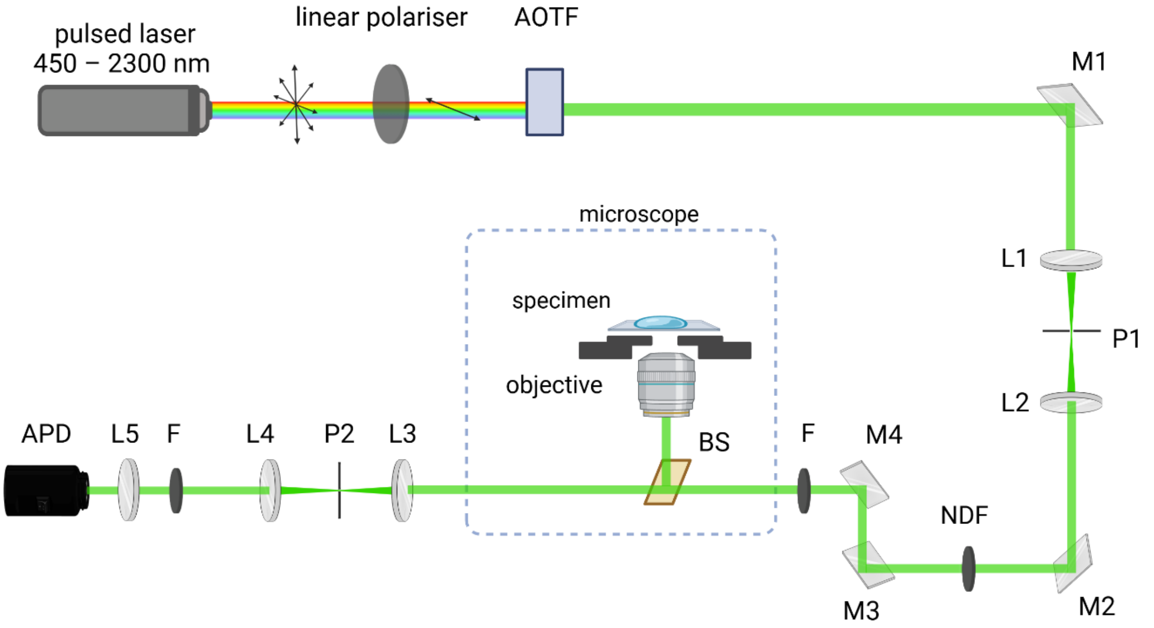

Figure 8.1 The schematic representation of the home-built optical setup based on the confocal microscope consisted of the non-polarized supercontinuum laser source, a linear polarizer, acousto-optic tunable filter (AOTF), avalanche photodiode (APD), and several optical elements such as mirrors (M), lenses (L), pinholes (P), filters (F), beam splitter (BS). Created with BioRender.com.

3.1 Time-Correlated Single Photon Counting (TCSPC)

Time-Correlated Single Photon Counting [193], [194] (TCSPC) is a highly sensitive technique for recording low-intensity light signals. It is based on detecting single photons from a periodic light source, typically a pulsed laser, and accurately measuring the arrival time of individual photons to construct decay curves. A key requirement for TCSPC is that the probability of detecting more than one photon per pulse must remain low; ideally, fewer than one photon per 1,000 emitted excitation pulses should be detected. Higher detection rates would bias the histogram toward shorter times, as TCSPC only records the first detected photon, disregarding subsequent photon arrivals. The core principle of TCSPC involves measuring the time delay between the excitation pulse and the corresponding photon detection event, as illustrated in Figure 8.2. These time intervals are accumulated and stored in a histogram, which forms the basis for constructing fluorescence decay profiles. The TCSPC system operates using two key signals: a ‘start’ signal and a ‘stop’ signal. The ‘start’ signal is generated by the laser driver or a fast photodiode upon excitation of the sample and is recorded by the timing electronics as a reference.

The ‘stop’ signal is generated when a single-photon detector detects an emitted fluorescence photon (e.g., an avalanche photodiode or a photomultiplier tube). The system measures the time difference between the ‘start’ and ‘stop’ signals, corresponding to the delay between the excitation pulse and the photon emission. This process is repeated many times, with each photon detection contributing to a histogram of photon arrival times, thereby reconstructing the fluorescence decay curve. Noteworthily, the TCSPC system often operates in reverse start-stop mode for practical reasons. In this configuration, detecting a fluorescence photon serves as the "start" signal, and the subsequent laser pulse acts as the "stop" signal. The electronics measure the time interval between the photon detection and the preceding laser pulse. This reverse approach ensures that the system processes only detected photons, avoiding the overwhelming frequency of laser pulses while leveraging the laser’s highly stable repetition rate. The resulting histogram of time intervals provides an accurate reconstruction of the fluorescence decay curve. The repeated excitation ensures a steady population of molecules in the excited state, enabling statistically robust measurements. As shown in Figure 3.2, the fluorescence decay curve is constructed by accumulating photon detection events over time.

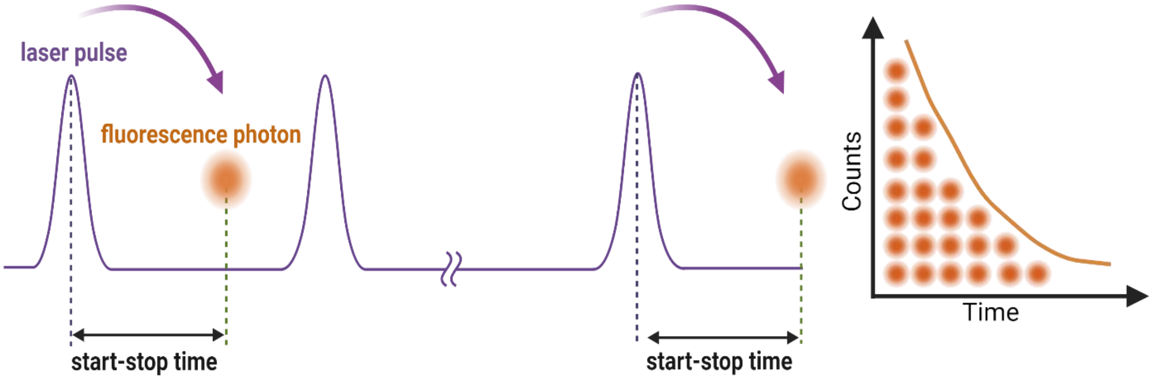

Figure 8.2 The time measurement between excitation and emission of the fluorescence photon. Created with BioRender.com.

Mono-exponential decay can be described mathematically using the following equation:

$$I(t) = \alpha \cdot exp\left(-\frac{t}{\tau}\right) \qquad (3.1)$$

$\mathrm{I(t)}$ is the fluorescence intensity at time t, α is the pre-exponential factor, and τ is the fluorescence lifetime.

TCSPC distinguishes itself from traditional analog signal processing techniques through its superior time resolution, which is not constrained by the detector’s impulse response width [195], [196], [197]. Instead, the time resolution in TCSPC is dictated by the timing accuracy within the detection channel. This accuracy is influenced by the transit time spread of single-photon pulses within the detector and the precision of the trigger signals in the electronics. Remarkably, the timing precision in TCSPC can be up to an order of magnitude better than the half-width of the detector's impulse response. [198], [199], [200]. For a given number of detected photons N, the signal-to-noise ratio (SNR) is given by Equation 3.2.

$$SNR = \sqrt{N} \qquad (3.2)$$

TCSPC also benefits from a favorable noise profile: noise arising from leakage currents, gain instabilities, and stochastic processes in the detector do not contribute to the decay curve. Consequently, TCSPC offers an excellent signal-to-noise ratio as long as the emission intensity is kept low enough to avoid photon pile-up effects, ensuring that all detected photons contribute meaningfully to the fluorescence decay.

4 Scanning Electron Microscopy

The Nova NanoSEM 450 scanning electron microscope (SEM) was used to verify whether the 2D materials were free of defects and impurities after the transfer. For SEM analysis, small sections of silicon wafer substrates (approximately 1 cm^2) were prepared by sonicating them in a 0.5% Hellmanex™ III solution at 50 °C for 15 minutes. This was followed by a second sonication in deionized water (50 °C, 15 minutes) to ensure complete removal of any residual alkali solution. Subsequently, graphene or hexagonal boron nitride (hBN) was deposited onto the cleaned substrates using the method described earlier in Chapter 2.1 [4]. After removing the PMMA layer, the samples were mounted onto SEM specimen stubs with copper tape. The samples were then characterized using the scanning electron microscope (SEM) in immersion mode. In this technique, the sample is placed within the magnetic field of the objective lens to enhance resolution and improve image quality. This characterization was performed at an accelerating voltage of 10 kV.

5 Raman spectroscopy

Raman spectroscopy is a primary tool for assessing the quality of graphene. This study acquired Raman spectra using an Invia Renishaw Raman spectrometer coupled with an integrated Leica microscope. The system is equipped with a thermoelectrically cooled 1024 × 256-pixel CCD detector and a high-resolution single monochromator. Raman spectra were collected at each measurement position during raster scanning of the sample in the horizontal (XY) plane. Measurements were conducted using excitation wavelengths of 632.8 nm and 520 nm, with a 50× Leica objective (NA = 0.75). The scattered light was dispersed using 1200 l/mm holographic gratings in the visible spectral range. The acquisition time per pixel was set to 20 seconds, with an excitation power of 1 mW. Data processing, including cosmic ray correction, intensity mapping of graphene peaks, and averaging the collected data, was performed using Renishaw Wire 5.6 software.

6 Atomic Force Microscopy

High-resolution imaging of the samples' surface topography was performed using atomic force microscopy (AFM) with a Dimension Icon system (Bruker). All images were captured in tapping mode to minimize sample perturbation and ensure accurate characterization of the delicate graphene layers. Standard silicon cantilevers (Bruker TESPA-V2) with a nominal spring constant of ~42 N/m and a resonant frequency of ~320 kHz were used for imaging. The drive amplitude was carefully optimized to balance image resolution and tip-sample interaction, typically at 60% of the free amplitude.

The scan rate was maintained at 1 Hz, and images were acquired with a resolution of 512 × 512 pixels to provide detailed visualization of the surface features. The setpoint ratio was adjusted to maintain a gentle interaction force, ensuring that no damage occurred to the graphene layers during imaging. To obtain statistically robust information, multiple regions of interest were scanned across different surface areas for each sample, typically covering scan sizes ranging from 1 μm × 1 μm to 10 μm × 10 μm, depending on the feature size and uniformity of the sample.

The images presented in this study are representative of the observed surface characteristics and were processed using NanoScope Analysis software to extract quantitative information, such as roughness and layer thickness. These parameters were carefully selected to ensure reliable and reproducible imaging of the graphene layers and related nanostructures.

Results

This work presents graphene as a highly efficient, broadband, and non-bleaching energy acceptor, underscoring the potential of "graphene energy transfer". The efficiency of GET strongly depends on the distance between graphene and the energy donor (fluorophore), which allows for the precise detection of fluorescence signal variations at the nanometric scale as the distance changes. To accurately measure these subtle variations, significant modifications were implemented to the optical setup based on a confocal microscope. These enhancements include an expanded excitation wavelength range, precise multi-wavelength selection, improved time resolution, and an optimized signal-to-noise ratio, allowing for more accurate fluorescence measurements. Additionally, the setup facilitates fluorescence lifetime measurements using time-correlated single-photon counting (TCSPC), further advancing the capabilities of fluorescence studies and enabling detailed exploration of GET dynamics. Moreover, additional graphene layers were incorporated to extend graphene's energy transfer capabilities, expanding the interaction range between graphene and the fluorophore. A layer-by-layer assembly technique was employed to meticulously control the formation of multilayer graphene. This method, optimized for mono- and multilayer graphene, also facilitated the creation of more complex systems such as van der Waals heterostructures. In particular, hexagonal boron nitride (hBN) was selected to form heterostructures with graphene due to its atomically flat surface, structural compatibility with graphene, and insulating properties. These unique characteristics of hBN are expected to enhance the overall quality of the graphene system without compromising its energy acceptor properties.

1. Modification of the home-built optical setup based on a confocal microscope

This chapter outlines the step-by-step protocol for single-molecule experiments, detailing the data obtained from individual experiments and the methodologies used for analyzing and representing the results. The focus is on the stringent conditions that must be met for successful experimentation. Additionally, modifications to the optical setup are introduced to enhance the performance of the home-built apparatus.

The initial optical setup is schematically presented in Figure 9.1. The system was based on an inverted confocal microscope configuration. As explained in more detail in the Methods section, lenses are arranged in a confocal microscope so that their focal points coincide. The system incorporates confocal apertures, allowing light only from the focal plane to reach the detector. This feature is a key advantage of confocal microscopy, as "out-of-focus" light is excluded from the image through the aperture. Consequently, the system provides images of exceptional resolution and clarity. Imaging is achieved by altering the plane or level of observation, resulting in images obtained from different focal positions. In the optical system, two lasers were employed: a 633 nm HeNe continuous wave (CW) laser and a pulsed 635 nm laser. The light was directed through a telescope, comprising two lenses and a confocal aperture, to “clean” the beam and ensure its collimation. The desired beam diameter was achieved by appropriately selecting the focal lengths of the lenses. The collimated beam then passed through a linear polarizer and a set of neutral density filters, enabling precise laser power regulation. Upon entering the microscope, the collimated and filtered laser light was directed via a 90:10 beam splitter onto the sample plane. The laser power was adjusted not to exceed 1 μW at the focal plane. Fluorescence signals from the sample were returned through the same beam splitter to the detector. Before reaching the detector, the signal passes through a set of lenses and high-pass filters to separate the fluorescence signal from laser light. An avalanche photodiode was used as the detector, converting the signal into a digital format containing information about the laser’s position on the sample and the intensity of light emitted from the sample.

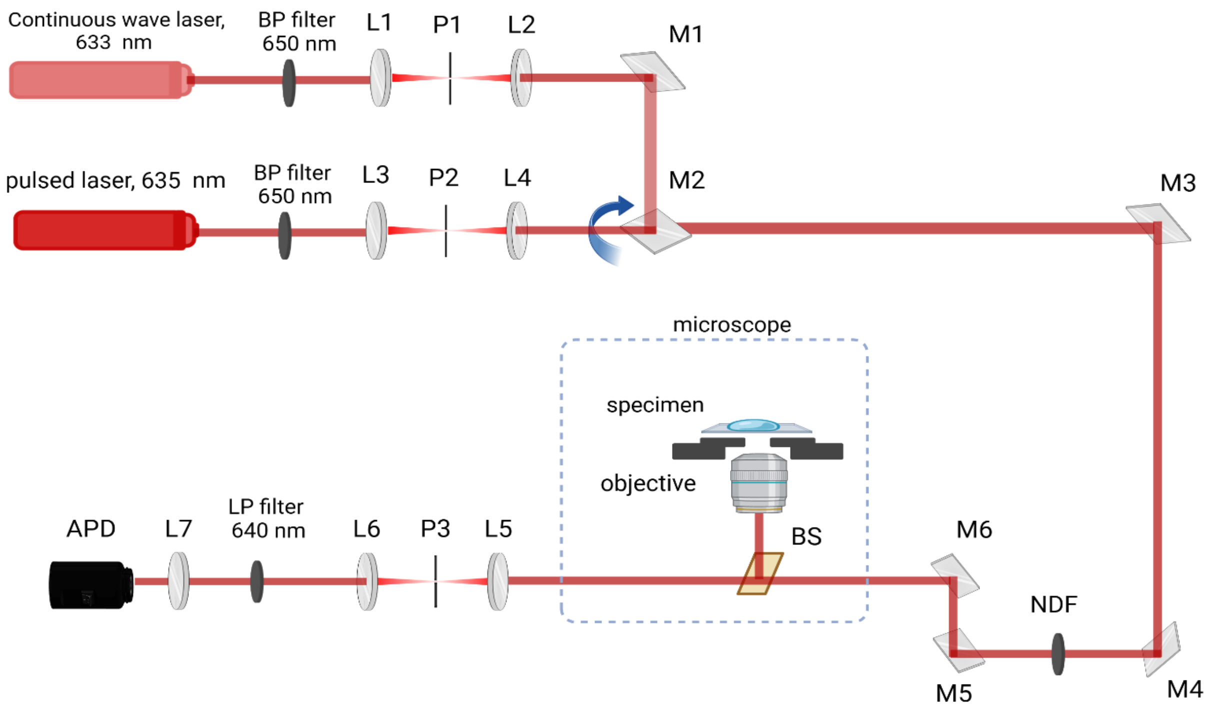

Figure 9.1 The schematic representation of the home-built optical setup based on the confocal microscope consisted of the non-polarized supercontinuum laser source, a linear polarizer, acousto-optic tunable filter (AOTF), avalanche photodiode (APD), and several optical elements such as mirrors (M), lenses (L), pinholes (P), filters (F), beam splitter (BS). Created with BioRender.com.

The measured data is represented by the fluorescence maps of the studied molecules, displayed as high-resolution images obtained through XY-plane scanning of the sample. Moreover, the pulsed laser enabled measurements of transient fluorescence. The TCSPC software from Becker & Hickl controls the system for high-resolution fluorescence lifetime measurements. It enables real-time photon data acquisition, decay analysis, and Fluorescence Lifetime Intensity Map (FLIM) generation.

The main components of the constructed measurement system included:

- 633 nm CW laser and 635 nm pulsed laser: The light source used for sample excitation.
- Controlled shutter: Regulates the timing of sample excitation.
- Inverted fluorescence microscope, whose components include:
    - Microscope stage: Ensures sample movement in a plane perpendicular to the propagation direction of the excitation beam.

  - Immersion objective lenses (100×, NA 1.4) or alternative objectives (60×, 40×, 10×): For focusing the excitation beam and collecting fluorescence.
  - Dichroic mirrors (Omega Optical; XF 2012 for 514.5 nm excitation, and XF 2021 for 632.8 nm excitation): Direct the excitation light and separate it from fluorescence emission.
  - Filters eliminate excitation radiation. These include "cut-off" filters (Omega Optical; XR02 and XR3003-640 ALP) and "notch" filters (Kaiser Optical System).
  - Avalanche photodiode: Used as the fluorescence detector (SPCM-AQRH-14-TR, Excelitas).
  - CCD camera (SHARP; YK-2047): Monitors the uniformity of sample illumination.

While functional, the system lacked flexibility in excitation wavelengths, limiting the range of fluorophores that could be investigated. Additionally, the inability to excite multiple fluorophores quasi-simultaneously hindered the development of multiplexed biosensing applications and limited studies involving the colocalization of dyes.

To overcome these limitations, several modifications were implemented. A nonlinear pulsed supercontinuum laser source and an acousto-optic tunable filter (AOTF) were integrated into the system. Both parts have been designed on the optical table to fit all the other parts of the microscope. The supercontinuum white Fyla laser is a nonlinear, pulsed light source that generates a broadband emission spanning the visible spectrum and beyond. Its high temporal resolution and spectral versatility make it particularly suitable for advanced fluorescence microscopy and spectroscopy. This laser excites multiple fluorophores, significantly enhancing the capabilities for multiplexed imaging and single-molecule studies. The acousto-optic tunable filter (AOTF) is an advanced optical device that allows precise, rapid, and programmable selection of specific wavelengths from a broadband light source, such as the supercontinuum laser. The AOTF enables simultaneous or sequential excitation at multiple wavelengths by utilizing acoustic waves to modulate light, providing exceptional flexibility and control in spectrally resolved fluorescence measurements. These modifications expanded the excitation wavelength range and provided precise multi-wavelength selection, enabling significant advancements in fluorescence studies.

The modified setup is presented in Figure 9.2. The system features a pulsed, non-polarized supercontinuum laser source (450–2300 nm, Fyla®), which is aligned through a linear polarizer (WP12L-Vis, Thorlabs) and an acousto-optic tunable filter (AOTFnC-VIS-TN, Opto-Electronic®) to select the desired wavelength within the 450–700 nm range. For these experiments, wavelengths of 532 nm (green) and 639 nm (red) were alternately employed, depending on the specific requirements of the specimen. The beam is spatially filtered by focusing it through a lens (L1) onto a 25 μm pinhole (P, Thorlabs). The laser power was precisely regulated using a neutral density filter, followed by spectral filtering with a bandpass filter (F) tailored to the laser wavelength. Specifically, a bandpass filter with a center wavelength (CWL) of 640 nm and a bandwidth of 10 nm (FBH640-10, Thorlabs) was employed for the red laser, while a bandpass filter with a CWL of 532 nm and a bandwidth of 4 nm (FLH532-4, Thorlabs) was utilized for the green laser. These filters ensured spectral purity before the laser beams entered the microscope. Within the microscope, the laser beams were first directed to a beamsplitter (BS, 90:10) and subsequently focused onto the sample through the objective lens. The sample is scanned point by point, with a piezoelectric stage moving the specimen relative to the stationary laser beam. The emitted fluorescence is collected and refocused by a lens (L3) before passing through a 50 μm pinhole, which serves to eliminate signals originating from regions outside the focal plane. The laser light is then further filtered (F, red: FESH0750, Thorlabs and LP02-647RU-25, Semrock green: 582/75 BrightLine HC, Semrock and LP03-532RU-25, Semrock), and the fluorescence signal is collimated with another lens (L5) before reaching an array of avalanche photodiodes (APD, SPCM-AQRH-14-TR, Excelitas), where individual photon events are detected. Single-molecule intensity maps were acquired using custom-developed software in LabVIEW, which also facilitates recording single-molecule time traces. This software includes modules for time trace analysis, providing critical data such as the average fluorescence intensity, the photobleaching time, and the total number of emitted photons. Time-correlated single photon counting (TCSPC) of individual molecules was performed using software from Becker & Hickl.

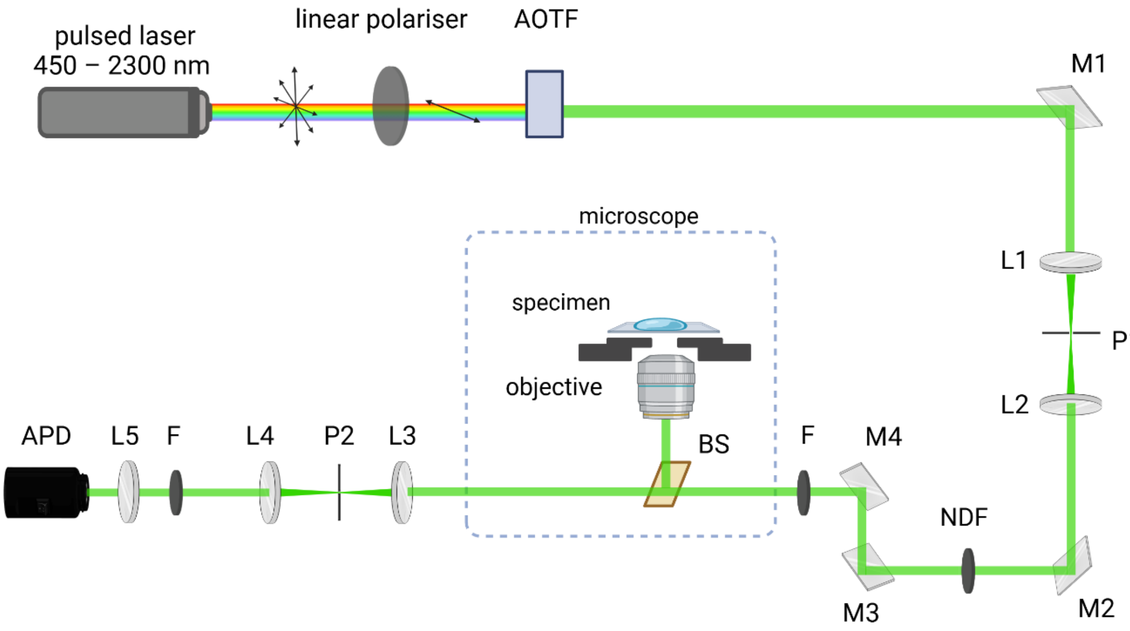

Figure 9.2 The schematic representation of the home-built optical setup based on the confocal microscope consisted of the non-polarized supercontinuum laser source, a linear polarizer, acousto-optic tunable filter (AOTF), avalanche photodiode (APD), and several optical elements such as mirrors (M), lenses (L), pinholes (P), filters (F), beam splitter (BS). Created with BioRender.com.

1.1. Principles of single-molecule measurements

Single-molecule experiments were performed using a before-described custom-built optical setup based on an inverted fluorescence confocal microscope and at the optical setup based on the fluorescence confocal microscope in Prof. Philip Tinnefeld’s group at LMU in Munich.

The setup is based on a home-built confocal microscopy system constructed around an Olympus IX71 inverted microscope. The green laser (LDH-P-FA-530B, PicoQuant) was controlled by a PDL 828 “Sepia II” driver (PicoQuant) and delivered through a polarization-maintaining fiber (FC/APC output connector). The laser output was collimated using a fiber collimator (F220APC-532, Thorlabs) and spectrally filtered with a 532/2 bandpass filter (Z532/10 X, Chroma) before passing through a dichroic mirror (640 LPXR, Chroma). This configuration also allowed optional combination with a red laser (LDH-D-C-640, PicoQuant), pre-cleaned using a Z640/10 X bandpass filter (Chroma).

A linear polarizer (WP12L-Vis, Thorlabs) and a quarter-wave plate (AQWP05M-600, Thorlabs) were employed to achieve circularly polarized light. The combined beams passed through a second dichroic mirror (zt532/640rpc, Chroma) and were focused onto the sample using an oil immersion objective (UPLSAPO 100XO, NA 1.40, Olympus). Sample scanning was performed using a piezoelectric stage (P-527.3CD, Physik Instrumente) controlled by an E-727 controller (Physik Instrumente). Emitted fluorescence was focused onto a 50 µm pinhole (Thorlabs) and collimated using a lens (AC050-150-A-ML, Thorlabs). Subsequently, the beam was cleaned with a filter set (582/75 BrightLine HC, Semrock, and LP03-532RU-25, Semrock) and then split by a 50:50 non-polarizing beam splitter cube (BS013, Thorlabs). Afterward, the beam was split using a dichroic mirror (640 LPXR, Chroma) and further cleaned with wavelength-specific filter sets (red: FESH0750, Thorlabs, and LP02-647RU-25, Semrock; green: 582/75 BrightLine HC, Semrock, and LP03-532RU-25, Semrock). The split beams were subsequently focused using lenses (red: AC080-020-B-ML; green: AC080-020-A-ML, Thorlabs) onto avalanche photodiodes (APDs, SPCM-AQRH-TR-14, Excelitas). The APD signals were processed by a HydraHarp 400 time-correlated single-photon counting module (PicoQuant) and analyzed using SymPhoTime 64 software (PicoQuant). Further data analysis was performed using custom-written routines in Matlab and LabVIEW.

The procedure described below for single-molecule measurements is consistent across all experiments in this thesis that employed confocal microscopy. All samples were prepared by immobilizing DNA nanostructures on cleaned glass coverslips and measured in an aqueous buffer environment. Specifically, a silicon chamber was assembled on the glass coverslip to create a confined space for the sample. The chamber was filled with a buffer solution containing the DNA nanostructures at the desired concentration. After an appropriate incubation period for immobilization, the sample was gently washed with buffer to remove unbound structures. This preparation ensured a stable and suitable environment for high-resolution single-molecule fluorescence measurements using confocal microscopy.

The sample is placed on an immersion objective, and scanning is conducted point-by-point using a computer-controlled piezoelectric stage. Dye molecules are excited using a supercontinuum laser (typically 532 nm and 639 nm are selected), and an avalanche photodiode collects the resulting fluorescence signal, which is then processed using custom-written software in LabView. The software generates a fluorescence intensity map of the scanned area (typically 10 μm × 10 μm), with an example map shown in Figure 9.3. Bright spots on the map correspond to fluorescence from dye molecules.

Determining whether each bright spot represents a signal from a single dye molecule or multiple molecules requires additional analysis. One commonly used approach is recording time traces (Figure 9.3), where the intensity fluctuations over time can reveal characteristic single-molecule photobleaching steps. For example, the fluorescence signal of a single molecule will typically exhibit a single photobleaching event, while signals from multiple molecules may show sequential photobleaching steps corresponding to each molecule.

Alternatively, other methods can be employed to make this distinction. Intensity histograms can provide insights by comparing the observed fluorescence intensity with the expected levels for single molecules. Additionally, fluorescence correlation spectroscopy (FCS) can analyze temporal fluctuations in fluorescence intensity, providing quantitative information about the number of emitting species [201]. Polarization-resolved measurements can also differentiate between single and multiple molecules based on the orientation of their transition dipole moments [202]. These complementary methods can often provide more robust verification, depending on the specific experimental conditions and requirements.

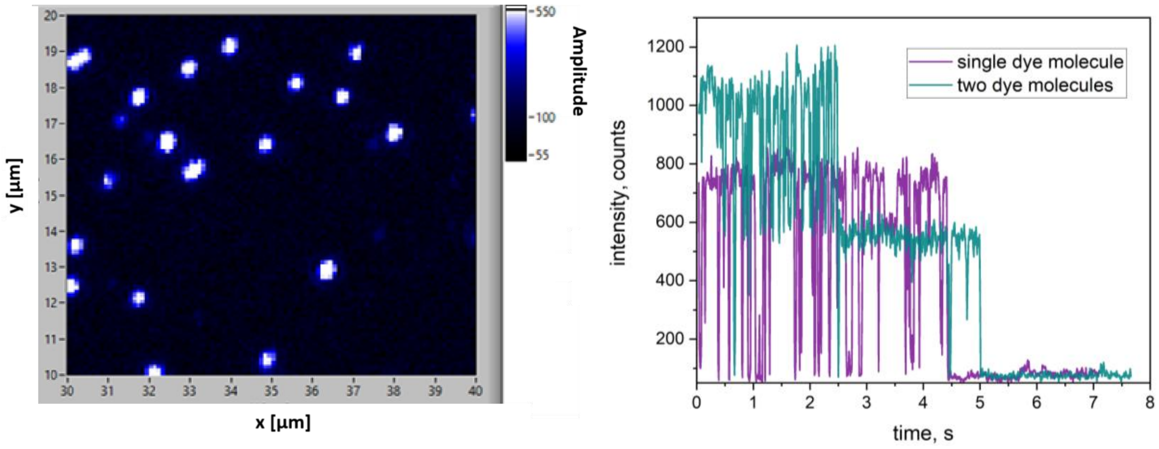

Figure 9.3 (left) Exemplary fluorescence intensity map, (right) Exemplary time traces representing the signal registered for a single molecule (purple) and more than one molecule (cyan).

A time trace captures the continuous absorption-emission cycles of a fluorophore until photobleaching occurs. An analogy to a staircase helps illustrate and distinguish the signal from individual dye molecules. Photobleaching is a discrete, irreversible, one-step process for a single dye molecule where the signal abruptly drops to the background level. In contrast, two steps are observed in the time trace for two dye molecules, with the number of steps increasing with the number of dye molecules present.

Time traces provide valuable insights into the photophysical properties of fluorophores, offering data on the total number of emitted photons, the time before photobleaching, and the average fluorescence intensity. The fluorescence lifetime (τ) is related to the average intensity. However, direct measurement of τ using time-correlated single photon counting (TCSPC), described in Chapter 3.1 of the Methods section, is more accurate and reliable.

Fluorescence lifetime is independent of the fluorophore concentration, laser intensity, and optical alignment. This makes it a reliable parameter for directly probing molecular interactions, such as energy transfer between the dye and graphene. In contrast, fluorescence intensity can be highly sensitive to experimental conditions, including excitation power, dye concentration, and optical alignment. Even slight variations in these factors can significantly alter intensity, complicating interpretation. When a dye molecule is near graphene, non-radiative energy transfer occurs, resulting in a measurable reduction in the dye’s fluorescence lifetime. This lifetime change provides a precise and direct assessment of the energy transfer efficiency.

Fluorescence intensity can decrease due to energy transfer, but it is also influenced by other factors, such as photobleaching, scattering, or quenching unrelated to energy transfer. These additional factors introduce ambiguity in intensity-based measurements. In single-molecule fluorescence studies, photobleaching results in abrupt signal loss when a dye molecule is no longer accessible rather than a gradual decrease. However, in bulk measurements, photobleaching manifests as a progressive decline in overall fluorescence intensity, which can complicate distinguishing between intensity loss due to energy transfer and that due to dye degradation. Additionally, gradual decreases in fluorescence intensity in single-molecule experiments may arise from external factors such as setup misalignment, imprecise laser power settings, or focus drift.

Fluorescence lifetime measurements, by contrast, are less affected by photobleaching. Rather than relying on signal magnitude, lifetime measurements capture the time scale of the fluorescence decay, making them robust against fluctuations in total fluorescence intensity caused by these external factors or photobleaching events

Lastly, fluorescence lifetime measurements typically offer a better signal-to-noise ratio than intensity-based measurements. Lifetime changes can be distinguished from background signals, which usually exhibit different decay kinetics. In contrast, fluorescence intensity signals can be overshadowed by background fluorescence or sample autofluorescence, making it more challenging to accurately attribute changes to energy transfer.

2. Multilayer graphene platforms for GET studies

As previously discussed, graphene is a non-bleachable broadband energy transfer acceptor, eliminating the need for additional labeling of biomolecules. This system relies on distance-dependent, nonradiative energy transfer from an excited dye molecule to graphene, as detailed in Chapter 2.1 in the Introduction. The successful preparation of graphene-on-glass substrates and the precise design of DNA origami nanostructures address several critical challenges in single-molecule studies. Their combined features, such as optical transparency, biocompatibility, conductivity, and nanoscale precision, enable groundbreaking applications in single-molecule biophysics and biosensing [3], [4], [6] and superresolution microscopy [22], [203], [204]. Examples such as graphene-based biosensors for protein detection and DNA origami scaffold for studying molecular dynamics illustrate how this platform has emerged as a powerful tool for cutting-edge research [3], [92], [205], [206], [207], [208].

Building on this foundation, exploring multilayer graphene presents a new avenue for enhancing single-molecule fluorescence studies. Unlike monolayer graphene, multilayer structures offer additional benefits, such as tailored optical and electrical properties. Methods to modify graphene’s properties extend beyond simply adjusting the number of layers. Advanced techniques, including twist-angle engineering, enable the tuning of optical, electronic, and quantum behaviors. Adjusting the twist angle between the layers can give rise to superconductivity, flat band formation, and correlated insulating states [209], [210]. Additionally, chemical doping or selective deposition of adsorbates enhances the material’s utility in sensing or photovoltaics by introducing localized electronic states [211]. Strain engineering, on the other hand, locally modifies the band structure, facilitating fine-tuned optical responses [212], [213].

A layer-by-layer assembly approach was chosen for these studies due to its ability to produce graphene samples with highly customizable sizes and a precise number of layers. While this method lacks control over twist angles, it avoids the complexities of angle alignment or high-energy processing often required in other preparation techniques. However, it is important to acknowledge the limitations of this approach, particularly in forming high-quality multilayer graphene structures with more than three layers. The primary challenges include increasing difficulties in achieving uniform and defect-free stacking as the number of layers grows, which can lead to structural imperfections, decreased reproducibility, and reduced optical and electronic performance. These challenges are exacerbated by issues such as layer delamination, contamination during transfer steps, and nonuniform stacking alignment, which compromise the quality and consistency of thicker multilayer graphene.

Due to these limitations, the focus of this study was restricted to the preparation and characterization of multilayer graphene up to three layers. Beyond this threshold, the reproducibility and quality of the layers diminished significantly, making systematic investigations of their properties impractical. Unlike CVD-grown multilayer graphene, which suffers from significant heterogeneity across the substrate, the layer-by-layer approach offers greater modularity and precise control over the number of layers, albeit with constraints on scalability for thicker structures.

Despite these limitations, this method provides a pragmatic platform to explore the interplay between the number of layers and functional properties of graphene. The dependency has been investigated precisely by placing single dye molecules at defined distances to monolayer, bilayer, and trilayer graphene. In this study, the systematical investigation of the distance dependence of graphene energy transfer (GET) in bilayer and trilayer graphene was performed by analyzing the fluorescence lifetime of single molecules.

2.1. Preparation of multilayer graphene

As discussed in Chapter 6.1.1 of the Introduction, achieving full control over the CVD growth process remains challenging, especially when targeting specific numbers of graphene layers. The difficulty intensifies as the number of layers increases, with discrepancies between the intended layer count and the actual formation of adlayers becoming more pronounced [214], [215], [216]. Such inconsistencies compromise the uniformity of the final graphene product. To address this heterogeneity, it becomes essential to conduct correlative Raman and fluorescence mapping systematically. Therefore, it has been hypothesized that the approach of multilayer formation – based on the precise, layer-by-layer stacking of graphene sheets – would enhance uniformity and significantly improve the control over the number of layers.

To fabricate the multilayer graphene platforms, a wet-transfer protocol described in Chapter 1 of the Methods section was followed. The multilayers were constructed by repeating the transfer process twice or three times to create bilayer or trilayer graphene. After removing PMMA from the initial graphene layer, an additional monolayer – pre-etched and purified – was transferred onto the substrate, ensuring complete coverage of the underlying graphene. Notably, the second (or third) layer was intentionally larger than the bottom layer, a strategy aimed at minimizing defects and ensuring higher structural integrity.

In the initial investigations, scanning electron microscopy (SEM) was employed to assess the overall quality of the multilayer graphene platforms. However, the bilayer graphene samples prepared using this method exhibited significant imperfections. As depicted in Figure 10.1, the bilayer graphene was non-uniform and exhibited numerous fractures. Additionally, an unexpected and substantial amount of polymer residue was observed on the graphene surface. This finding was particularly surprising, as previous experiments conducted on monolayer graphene had consistently demonstrated high-quality samples and successful removal of PMMA residues.

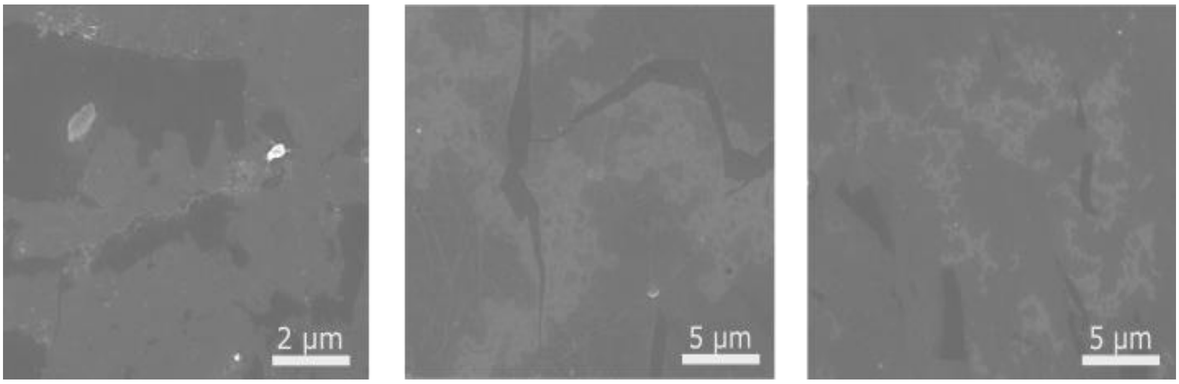

Figure 10.1 SEM images of bilayer graphene (the foils purchased from Graphenea®) prepared using the layer-by-layer method at various magnifications.

Given these observations, the quality of monolayer graphene samples was revisited, which was the foundation for the bilayer structures. Upon further inspection, SEM imaging (see Figure 10.2) revealed that the monolayer graphene contained considerable residual PMMA. This contamination likely contributed to the observed breakages in the upper graphene layer during bilayer formation.

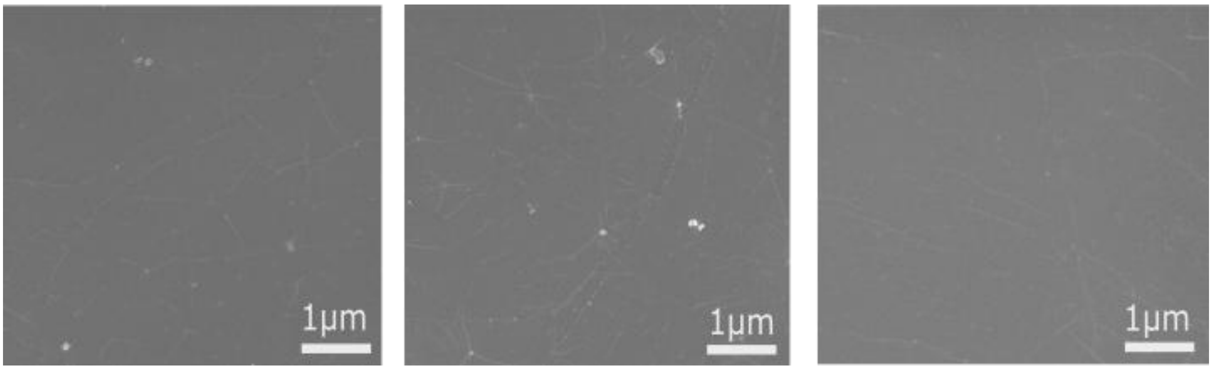

Figure 10.2 SEM images of monolayer graphene. The samples were prepared using foil purchased from Graphenea®.

The monolayer graphene used in these experiments was sourced from Graphenea®, one of several reliable suppliers of CVD-grown graphene. While previously there were no significant quality issues with their products, it is possible that this particular batch of monolayer graphene did not meet the highest quality standards, which proved critical for the success of the layer-by-layer bilayer formation.

Alternative suppliers had to be explored to address this concern. Without altering the established cleaning and transfer protocols, graphene was purchased from ACS Material®, and these samples were subjected to SEM imaging to evaluate surface quality, focusing on the presence of defects and impurities.

The comparative analysis included monolayer graphene and bilayer graphene, produced via the CVD method, and bilayer graphene, prepared using our layer-by-layer approach. Encouragingly, the samples from ACS Material® demonstrated significantly higher quality, allowing us to proceed with multilayer formation. SEM imaging (Figure 10.3) revealed that bilayer graphene produced via the layer-by-layer method exhibited a noticeably higher degree of homogeneity than that of the CVD-grown bilayer. This finding underscores the potential advantages of the proposed stacking method over conventional CVD techniques for producing high-quality multilayer graphene structures.

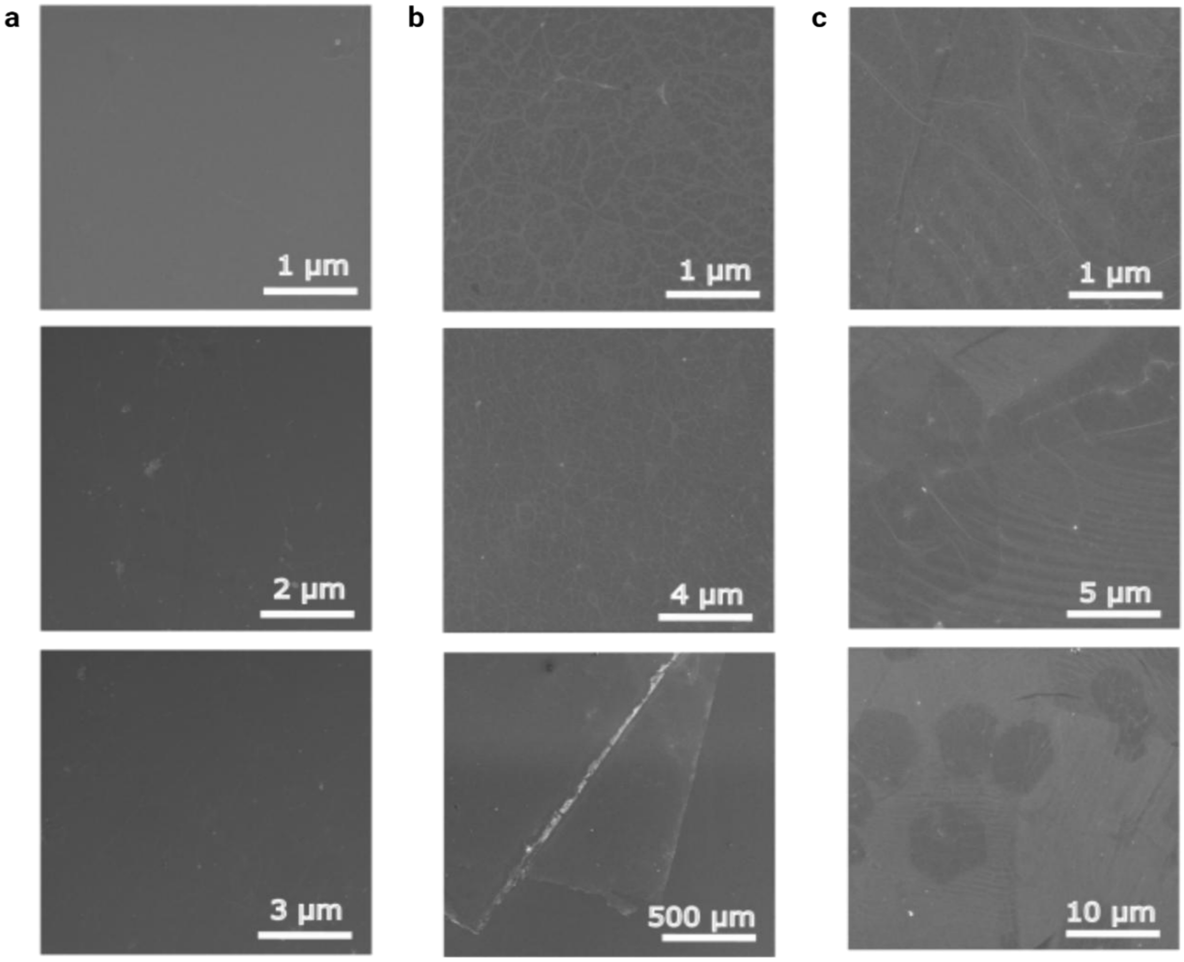

Figure 10.3 SEM images of monolayer graphene (a), bilayer graphene prepared using the layer-by-layer method (b), and bilayer graphene grown via CVD (c) at various magnifications.

2.2. Raman spectroscopy of mono- and bilayer graphene

All samples examined with SEM imaging were also imaged using Raman spectroscopy. Raman spectroscopy is an essential, non-destructive technique commonly used to verify graphene and graphene-related materials' structural and electronic properties [217], [218]. At this point, it is crucial to delve more into the origin of the Raman signal of graphene. The Raman spectrum of graphene is characterized by three prominent peaks: the G-band, the D-band, and the 2D-band, as presented on the spectrum below (Figure 10.4). Each of these three peaks provides valuable information about the material’s structure and quality.

The G-band observed at approximately 1580 cm^{-1} originates from the in-plane vibrations of sp^2-hybridized carbon atoms. In contrast, the D-band (observed around

1350 cm⁻¹) arises from structural imperfections, such as edges, dislocations, or vacancies. These defects activate the interval scattering mechanism that gives rise to the D-band peak. The intensity ratio of the D-band to the G-band (I_D/I_G) served as a measure of defect density level in graphene. A low I_D/I_G ratio indicates high quality graphene, whereas a higher ratio reflects a greater level of structural defects. The most distinctive feature of graphene's Raman spectrum is the 2D band, located ~ 2700 cm⁻¹. The peak arises from a second-order process involving the scattering of two phonons with opposite momenta, making it a double-resonance phenomenon. Unlike the D-band, the 2D-band does not require defects for activation. It is a powerful tool for characterizing the number of graphene layers, as its shape, intensity, and position are highly sensitive to the number of layers. In single-layer graphene, the 2D band is sharp and symmetric because the electronic structure consists of linearly dispersed Dirac cones at the K and K′ points in the Brillouin zone, resulting in a straightforward, unperturbed double-resonance Raman scattering process. However, as additional layers are introduced, the 2D band undergoes significant changes due to interlayer coupling and the emergence of more complex electronic band structures. These changes provide valuable information about the stacking order and uniformity of multilayer graphene.

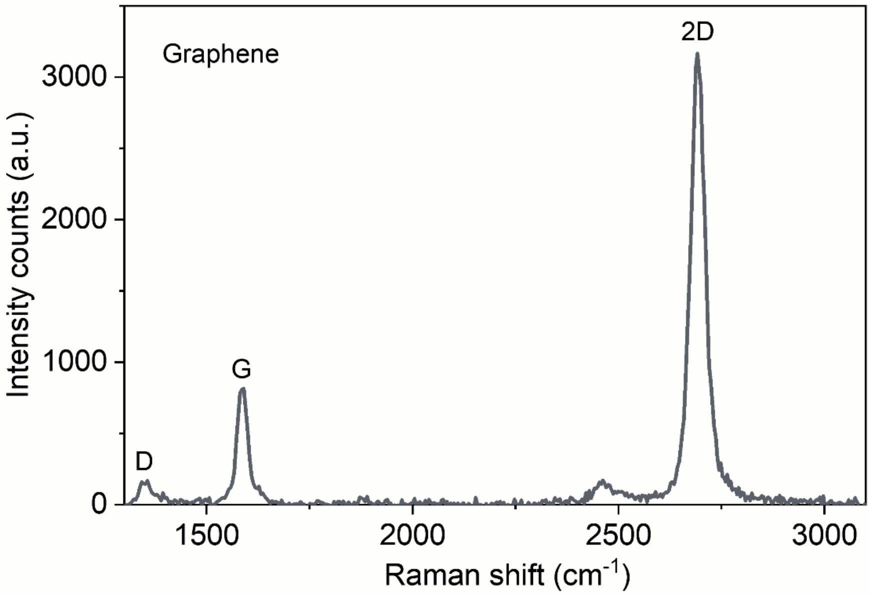

Figure 10.4 Raman spectrum of graphene.

In a multilayer system, the interlayer interactions between the graphene layers lead to splitting the π and π* electronic bands. This splitting creates multiple resonant scattering pathways, resulting in a broader and asymmetric 2D-band, typically composed of several overlapping components. As the number of graphene layers increases, the 2D-band broadens and loses its symmetry, reflecting the heightened complexity of the electronic band structure and the influence of stacking order. These variations in the 2D-band provide a reliable method for distinguishing single-layer graphene from bilayer and multilayer configurations. Several key phenomena contribute to these changes. First, the electron-phonon coupling in graphene strongly impacts the intensity and position of its Raman peaks, with the 2D-band being particularly sensitive to these interactions. Second, interlayer coupling alters the electronic band structure, modifying the double-resonance conditions responsible for the 2D-band. Finally, the stacking order of graphene layers also plays a role. For instance, specific vibrational modes and electronic transitions are activated in multilayer graphene with AB stacking, adding further complexity to the Raman spectrum. To conclude, the 2D-band is highly sensitive to the number of graphene layers. In the Raman spectrum of monolayer graphene, the 2D-band is intense, sharp, and symmetric, and the ratio between the 2D-band and G-band is greater than 2. Upon addition of the second layer, the intensity of the 2D-band is broadened, asymmetric, and generally less intense relative to the G-band, with an I2D/IG ratio close to 1. As the number of graphene layers increases further (beyond two), the 2D band continues to evolve, becoming increasingly broad and asymmetric, with the 2D/G ratio decreasing further. These changes originate from the progressive modification of the electronic band structure and the introduction of more interlayer interactions. Thus, the 2D/G ratio is a reliable indicator of the number of graphene layers.

The bilayer graphene sample, prepared using the layer-by-layer method, was prepared in a way that enabled the collection of Raman spectra from both monolayer and bilayer regions within the same sample (SEM image, insert in Figure 10.5). Since the bilayer graphene region covers a larger area than the monolayer region, Raman spectra were collected from three distinct locations within the bilayer region to account for any local variations. The spectra were averaged to provide a representative dataset for the bilayer graphene (Figure 10.5).

The Raman analysis reveals a clear distinction between the monolayer and bilayer graphene regions, particularly in the intensity ratio of the 2D and G bands

(2D/G ratio). For monolayer graphene, the 2D/G intensity ratio is 4.7, indicative of the sharp, symmetric 2D band that results from the unique electronic structure of single-layer graphene. In bilayer graphene, the 2D/G ratio decreases significantly to values of 0.97 and 0.88 for two different bilayer regions, reflecting the broadened and asymmetric nature of the 2D band as additional layers are introduced.

The observed decrease in the 2D/G ratio with the addition of a second graphene layer aligns with the well-established trends in Raman spectroscopy of graphene.

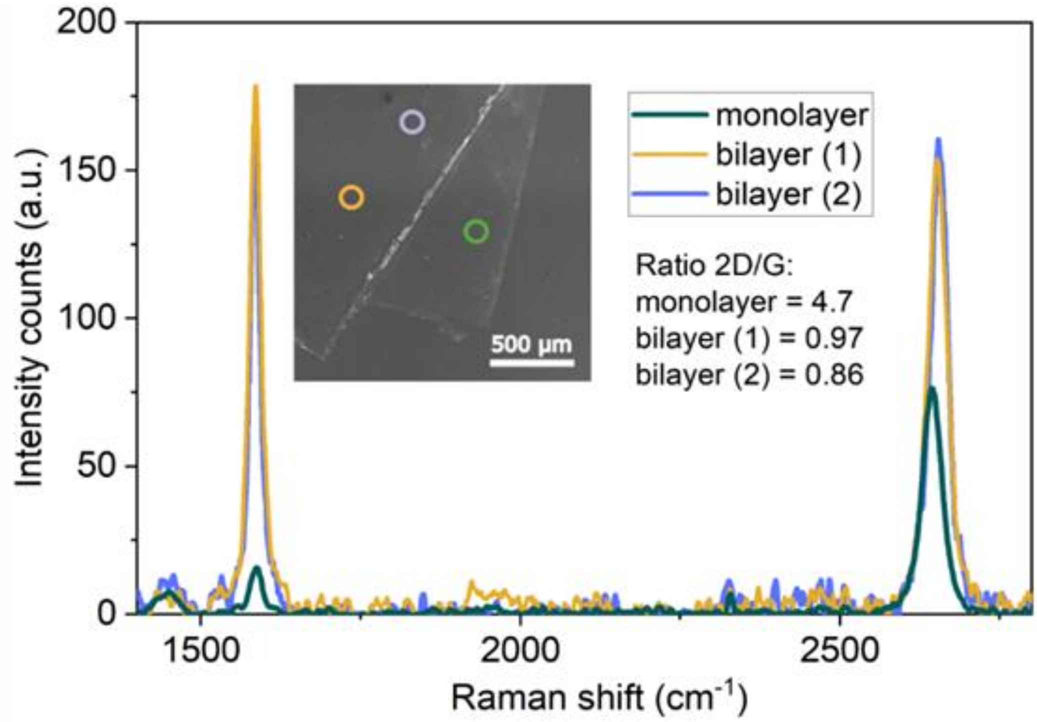

Figure 10.5 SEM-Raman measurements of graphene and layer-by-layer bilayer graphene. SEM image (insert) presents the partial overlapping of the two graphene layers. The circles mark the spots from the bilayer area (yellow and purple) and the monolayer (green) of the sample from which the Raman spectra were collected.

A similar procedure was applied to characterize bilayer graphene synthesized via CVD. Raman analysis of these samples corroborated the results obtained from SEM imaging, confirming that bilayer graphene prepared via CVD exhibits significantly higher heterogeneity than samples produced using the layer-by-layer method. Exemplary Raman spectra recorded at various positions on the CVD-grown sample (Figure 10.6) illustrate this heterogeneity.

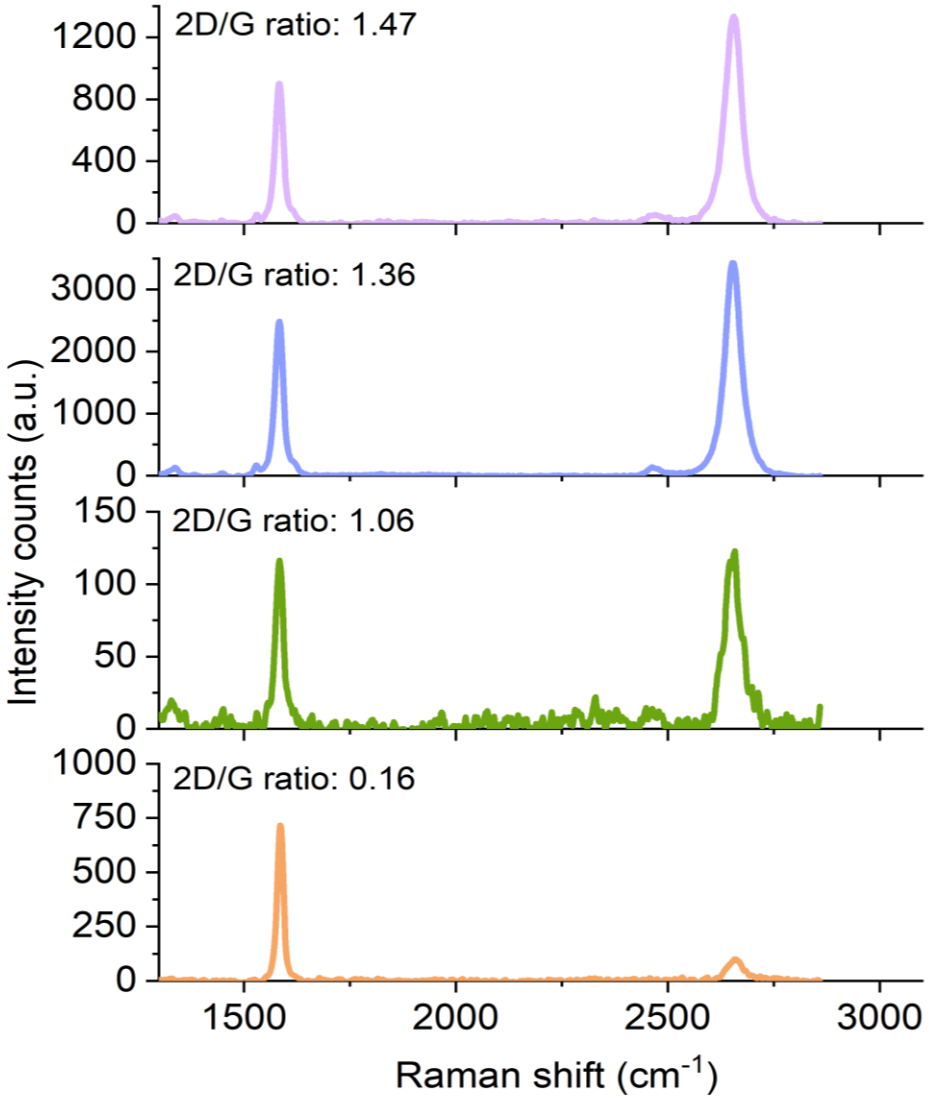

Figure 10.6 Raman spectra collected from the different spots of CVD-grown bilayer graphene present high heterogeneity in the sample.

The 2D/G intensity ratios observed in the spectra vary significantly across different sample regions, with values ranging from 1.47 to 0.16. These variations indicate the presence of regions with differing numbers of graphene layers, with higher 2D/G ratios corresponding to fewer layers and lower ratios indicating the presence of thicker or multilayer regions. For instance, the sharp 2D band and higher 2D/G ratio observed in the spectrum with a value of 1.47 suggest monolayer-like regions. In contrast, the broader 2D band and lower 2D/G ratio of 0.16 confirm regions with a higher number of layers.

This heterogeneity arises from the intrinsic technical limitations of CVD technology in growing homogeneous multilayer graphene. Specifically, CVD-grown multilayer graphene consists of micrometer-sized domains with a variable number of graphene layers, as demonstrated in the Raman analysis. These variations necessitate continuous correlative Raman and fluorescence mapping to accurately characterize the structural and optical properties across the sample, which can be both time-consuming and labor-intensive.

Given these challenges, we opted to employ the layer-by-layer assembly strategy for preparing multilayer graphene substrates. This methodology offers distinct advantages, including greater reproducibility and improved homogeneity in the resulting multilayer graphene films. In contrast to the heterogeneity of CVD-grown graphene, the layer-by-layer approach enables precise control over the number of layers and ensures uniformity across the substrate.

Additionally, a c comparative analysis of the Full Width at Half Maximum (FWHM) for the 2D graphene Raman bands was conducted for substrates prepared using the layer-by-layer method and CVD-grown graphene. The FWHM value, which represents the width of the Raman band at half its maximum intensity, was calculated by fitting the 2D band in the Raman spectra with a Lorentzian function. This calculation provides a quantitative measure of spectral sharpness. It is directly influenced by the electronic and vibrational properties of graphene, which are sensitive to the number of layers and the uniformity of the sample.

This analysis reveals that the layer-by-layer method produces graphene substrates with more excellent uniformity, as evidenced by a smaller maximum variation in FWHM values across the sample, measured at 2.5 cm^{-1}. In contrast, the CVD-grown graphene exhibited a significantly more significant maximum difference in FWHM values, reaching 5.5 cm^{-1}. The narrower and more consistent FWHM values observed in the layer-by-layer method indicate better control over the number of graphene layers and fewer structural or electronic inhomogeneities across the substrate. The larger variations in FWHM observed in CVD-grown graphene reflect the intrinsic challenges of achieving homogeneous layer thickness and defect-free domains with this method. These findings underscore the advantages of the layer-by-layer approach in producing substrates with higher quality and homogeneity

2.3. Influence of the number of Graphene Layers on Fluorophore–Graphene Interactions

Previous paragraphs demonstrated that the transfer and cleaning method optimized for preparing graphene-on-glass coverslips could effectively form more complex platforms consisting of (as tested so far) two or three graphene layers. The project's next step aimed to quantify the relation between GET and the number of graphene layers. To this end, pillar-shaped DNA origami nanostructures were employed and positioned vertically on the graphene substrate to investigate energy transfer to multilayer graphene. The DNA origami nanostructure was labeled with two dye molecules, ATTO 542 (green) and ATTO 647N (red), that were incorporated at specific heights spanning from 12 to 53 nm (the exact dye positions are listed in the next subchapter). The constructs were examined on monolayer, bilayer, and trilayer graphene.

2.3.1. Measurements on glass

In order to extract the reference values of the fluorescence lifetime for every dye molecule positioned at various heights, every DNA origami construct was immobilized and measured on a glass surface (in the absence of graphene). These reference measurements further confirmed the proper folding of DNA origami nanostructures and optimized concentrations for single-molecule readout.

As described in the previous chapter, the DNA origami constructs were immobilized on glass substrates using biotin-neutravidin interactions, ensuring precise and controlled nanostructure attachment. This approach is particularly suited for single-molecule imaging and biosensing applications. The preparation begins by assembling an incubation chamber on the surface of a cleaned glass coverslip, providing a controlled functionalization environment. The chamber is filled with a solution of biotinylated bovine serum albumin (BSA-biotin, 1 mg/mL) prepared in TAE-Mg^{2+} buffer, ensuring even distribution across the surface. The coverslip is then incubated in this solution for approximately 30 minutes to allow uniform adsorption of the biotinylated protein onto the glass surface. This step ensures efficient functionalization, which is critical for the subsequent immobilization of biomolecules or nanostructures. The biotinylated BSA serves a dual purpose: introducing biotin functionalities to the surface and blocking non-specific adsorption of molecules.

After incubation, the chamber is gently washed with buffer to remove any unbound BSA-biotin, ensuring a clean and functionalized surface. Next, a neutravidin solution (0.5 mg/mL) is introduced into the incubation chamber and allowed to interact with the BSA-biotin-coated surface for approximately 30 minutes at room temperature. This step ensures the specific binding of neutravidin to the biotin functionalities, creating a stable platform for further functionalization. After that, the surface is washed with buffer to remove unbound neutravidin. Biotin-labeled DNA origami nanostructures (functionalized with dye molecules) prepared in a TAE-Mg^{2+} buffer were incubated on the BSA-biotin-neutravidin-coated glass. Biotin-labeled DNA origami nanostructures, functionalized with dye molecules and prepared in TAE-Mg^{2+} buffer, were incubated on the BSA-biotin-neutravidin-coated glass surface for 5–10 minutes at room temperature. This incubation time is sufficient to allow the biotin moieties on the DNA origami to form strong non-covalent interactions with the neutravidin. After incubation, the surface was gently washed with TAE-Mg^{2+} buffer to remove any unbound DNA origami, leaving stably immobilized constructs ready for further experiments. The biotin-neutravidin interaction, characterized by its extraordinary binding strength (with a dissociation constant in the femtomolar range), provides a robust platform for immobilizing DNA origami nanostructures on the functionalized glass surface. After the incubation step, the surface is gently rinsed with TAE-Mg^{2+} buffer to remove any unbound or weakly adhered DNA origami structures. This washing step ensures that only stably immobilized constructs remain on the surface, providing a uniform and reproducible platform for subsequent single-molecule experiments

The measurements were carried out for a series of DNA origami nanostructures immobilized on the glass to get information about the fluorescence properties of the incorporated emitters. The sample (a glass coverslip with the incubation chamber) was placed on the microscope stage, and scanning was conducted point-by-point using a computer-controlled piezoelectric stage. The probes were excited using pulsed interleaved laser excitation at 532 and 639 nm, and both fluorescent emitters were excited quasi-simultaneously. The resulting fluorescence signal was collected using an avalanche photodiode and processed with custom-written software developed in LabView. This process generated a fluorescence intensity map of the scanned area, typically 10 μm × 10 μm. Exemplary maps and a more detailed description of the principles of single-molecule measurements can be found in Chapter 1.1 of the Results. The presence of both molecules (in the green and red channels) on the fluorescence intensity maps confirms the proper folding of the DNA origami nanostructures. The fluorescence signal from individual molecules was measured sequentially by recording the fluorescence intensity time traces. Afterward, the fluorescence decays of hundreds of single dye molecules were collected. They were further analyzed by applying a mono-exponential fitting model to determine the fluorescence lifetime of each emitter.

The fluorescence lifetime distributions were analyzed by fitting them with a Gaussian function to determine the mean value and standard deviation, offering detailed insights into the photophysical properties of the emitters. The results for the DNA origami nanostructure immobilized on a glass coverslip are shown in the histograms in Figure 2.7. This structure was functionalized with two dye molecules: ATTO 542 (green), positioned 16 nm above the substrate, and ATTO 647N (red), positioned 24 nm above the substrate (as depicted in Figure 10.7).

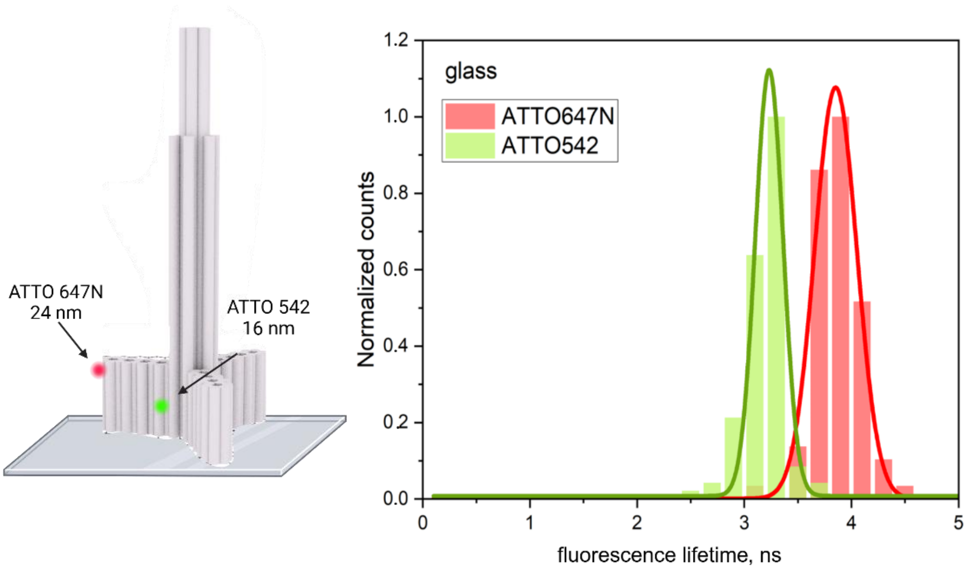

Figure 10.7 Left: the schematic representation of a pillar-shaped DNA origami nanostructure immobilized on glass coverslip, functionalized with two dye molecules: a dye ATTO 542 (green) positioned at the height of 16 nm and a dye ATTO 647N (red) at the height of 24 nm from the surface of the substrate. It is the exemplary dye combination; all DNA nanostructures, spanning the range of the positions of the dyes from 12 to 53 nm, were tested and resulted in the same values of the fluorescence lifetimes. Right: reference measurements of fluorescence lifetime registered for two dye molecules attached to the pillar-shaped DNA origami nanostructures immobilized on glass. The fluorescence lifetime of ATTO 647N (🟥) equals 3.81 ± 0.15 ns, and ATTO 542 (🟩) equals 3.27 ± 0.19 ns.

Since the reference measurements yielded satisfactory results, it was possible to begin the studies on graphene, with dye molecules being at the distances of graphene covering most of the effective region of GET.

2.3.2. Energy transfer studies for mono-, bi-, and trilayer graphene

The pillar-shaped DNA origami nanostructures, equipped with two dye molecules (at various heights ranging from 12 nm to 53 nm above the graphene surface), were immobilized on monolayer graphene, bilayer graphene, and trilayer graphene using single-stranded extensions (the method is described in Chapter 2.1 of the Methods section). Ten height combinations were used for the placement of ATTO 542 and ATTO 647N, respectively: (12 nm, 24 nm), (16 nm, 16 nm), (16 nm, 24 nm), (16 nm, 30 nm), (24 nm, 16 nm), (24 nm, 30 nm), (24 nm, 40 nm), (30 nm, 53 nm), (40 nm, 24 nm), and (53 nm, 30 nm).

The measurements were conducted according to the established protocol for experiments on glass. Figure 10.8 summarizes the results for pillar-shaped DNA origami nanostructures functionalized with ATTO 542 and ATTO 647N dyes, positioned at the height of 16 nm and 24 nm, respectively. They were immobilized on glass, monolayer graphene, and bilayer graphene. The schematic in Figure 2.8a depicts the nanostructures, while Figures 10.8b and 10.8c illustrate the impact of substrate type on fluorescence lifetime.

Exemplary fluorescence decay curves (Figure 10.8b) and lifetime maps (Figure 10.8c) reveal a systematic shortening of fluorescence lifetime with increasing graphene layers. The fluorescence lifetimes are visualized using a color-coded scale bar, where warmer colors (e.g., orange and yellow) represent longer lifetimes and cooler colors (e.g., green and blue) represent shorter lifetimes. The longest fluorescence lifetimes are observed on glass, as indicated by the prevalence of warm colors (e.g., orange and yellow) in the lifetime maps. This reflects no quenching due to the inert nature of the glass substrate. In contrast, monolayer graphene induces shorter lifetimes, evident from faster decay rates and the shift to cooler colors (e.g., green and blue), signifying effective quenching due to energy transfer to graphene’s surface. Bilayer graphene shows the most substantial quenching effect, with the shortest fluorescence lifetimes for ATTO 542 and ATTO 647N, attributed to the enhanced density of electronic states and interlayer coupling.

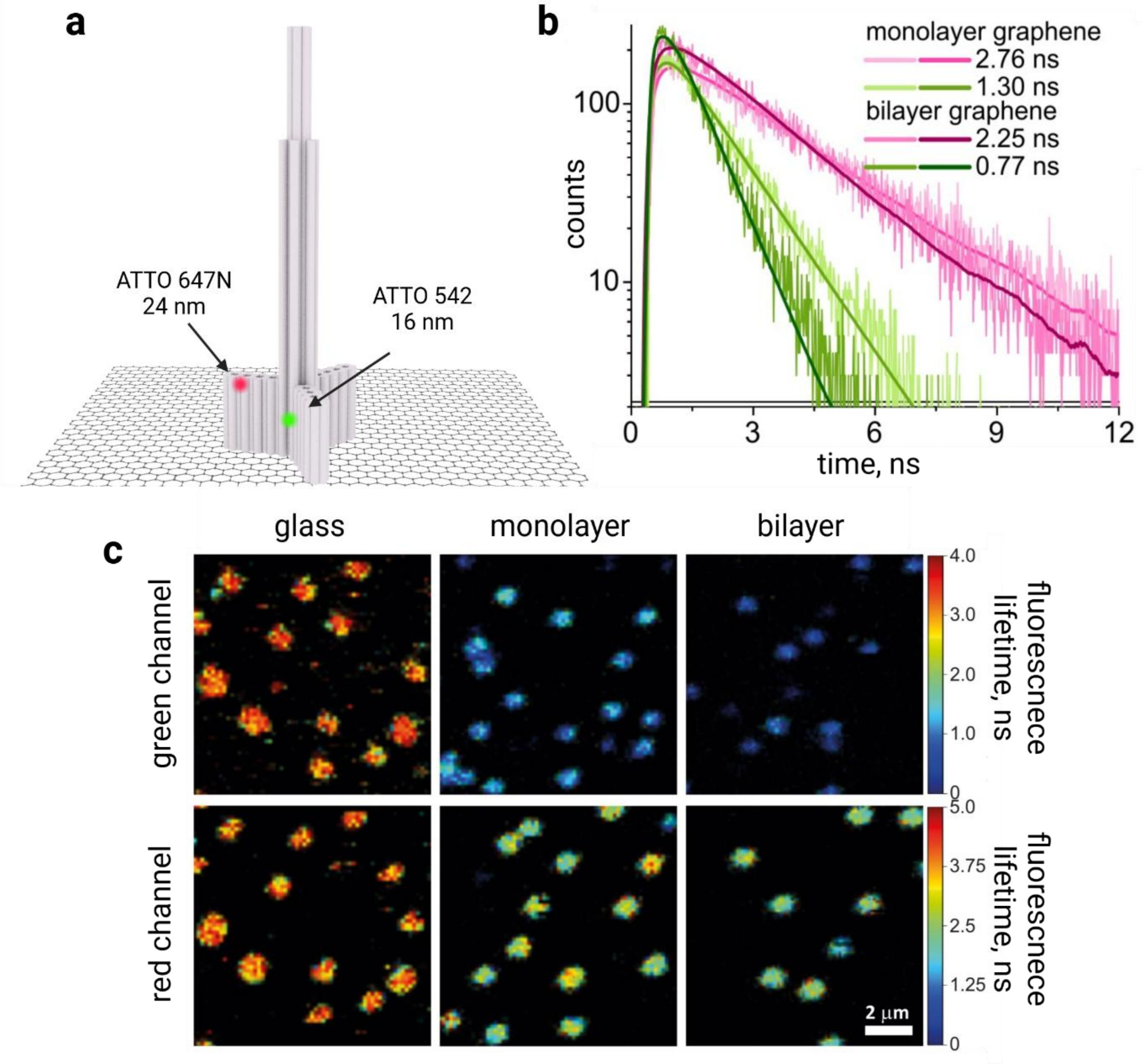

Figure 10.8 (a) Schematic representation of a pillar-shaped DNA origami nanostructure immobilized on a graphene substrate. The structure is functionalized with two dye molecules: ATTO 542 (green), positioned 16 nm above the substrate, and ATTO 647N (red), positioned 24 nm above the substrate. (b) Representative fluorescence decay curves for colocalized dye molecules (ATTO 542 in green and ATTO 647N in pink) within DNA origami nanostructures. Decays are shown for structures immobilized on monolayer graphene (light shades) and bilayer graphene (dark shades). They are fitted with a monoexponential model (c) Exemplary fluorescence lifetime map (10 × 10 µm) of DNA origami nanostructures. The green channel corresponds to ATTO 542, while the red channel corresponds to ATTO 647N. Measurements were performed on glass (left panel), monolayer graphene (middle panel), and bilayer graphene (right panel).

As discussed, ten height combinations were used to accurately define the relationship between fluorescence quenching and the number of graphene layers. For each sample, fluorescence lifetime measurements were performed for 120 to 270 individual molecules. The resulting fluorescence lifetime distributions, including mean values and standard deviations (summarized in Table 9), were fitted with

Table 9 The mean fluorescence lifetimes (τ, ns) and standard deviations for ATTO542 and ATTO647N molecules at varying distances (d, nm) from monolayer and bilayer graphene. The measurements highlight the influence of graphene on fluorescence lifetimes, with distinct trends observed for monolayer and bilayer configurations.

	ATTO542		ATTO647N	
	Monolayer graphene	Bilayer graphene	Monolayer graphene	Bilayer graphene
Distance (*d, nm*)	Lifetime (τ, ns)		Lifetime (τ, ns)	
12	0,42 ± 0.01	-	-	-
16	1,14 ± 0.01	0.63 ± 0.01	1.25 ± 0.01	0.60 ± 0.01
24	2,35 ± 0.01	-	2.66 ± 0.01	-
30	2,81 ± 0.01	2.54 ± 0.01	3.20 ± 0.02	2.78 ± 0.01
40	3,26 ± 0.01	-	3.70 ± 0.01	-
53	-	3,26 ± 0.01	3.97 ± 0.01	3.76 ± 0.01

The histograms illustrate the fluorescence lifetime-distance dependency for the dye molecules ATTO 542 (green) and ATTO 647N (red) immobilized on monolayer graphene (Figure 10.9, top panels) and bilayer graphene (Figure 2.9, bottom panels). For monolayer graphene, the distributions exhibit distinct fluorescence lifetimes across increasing distances (12–40 nm for ATTO 542 and 16–53 nm for ATTO 647N), demonstrating the expected reduction in quenching efficiency with increasing dye-to-graphene separation.

In contrast, the fluorescence lifetimes are shifted for bilayer graphene, with longer lifetimes observed at equivalent distances than monolayer graphene. This trend is particularly pronounced at larger distances (e.g., 30–53 nm), where bilayer graphene exhibits reduced quenching efficiency, indicating a weaker interaction range than monolayer graphene. These differences underscore the distinct quenching profiles of monolayer and bilayer graphene and highlight the role of graphene layer thickness in modulating fluorescence responses.

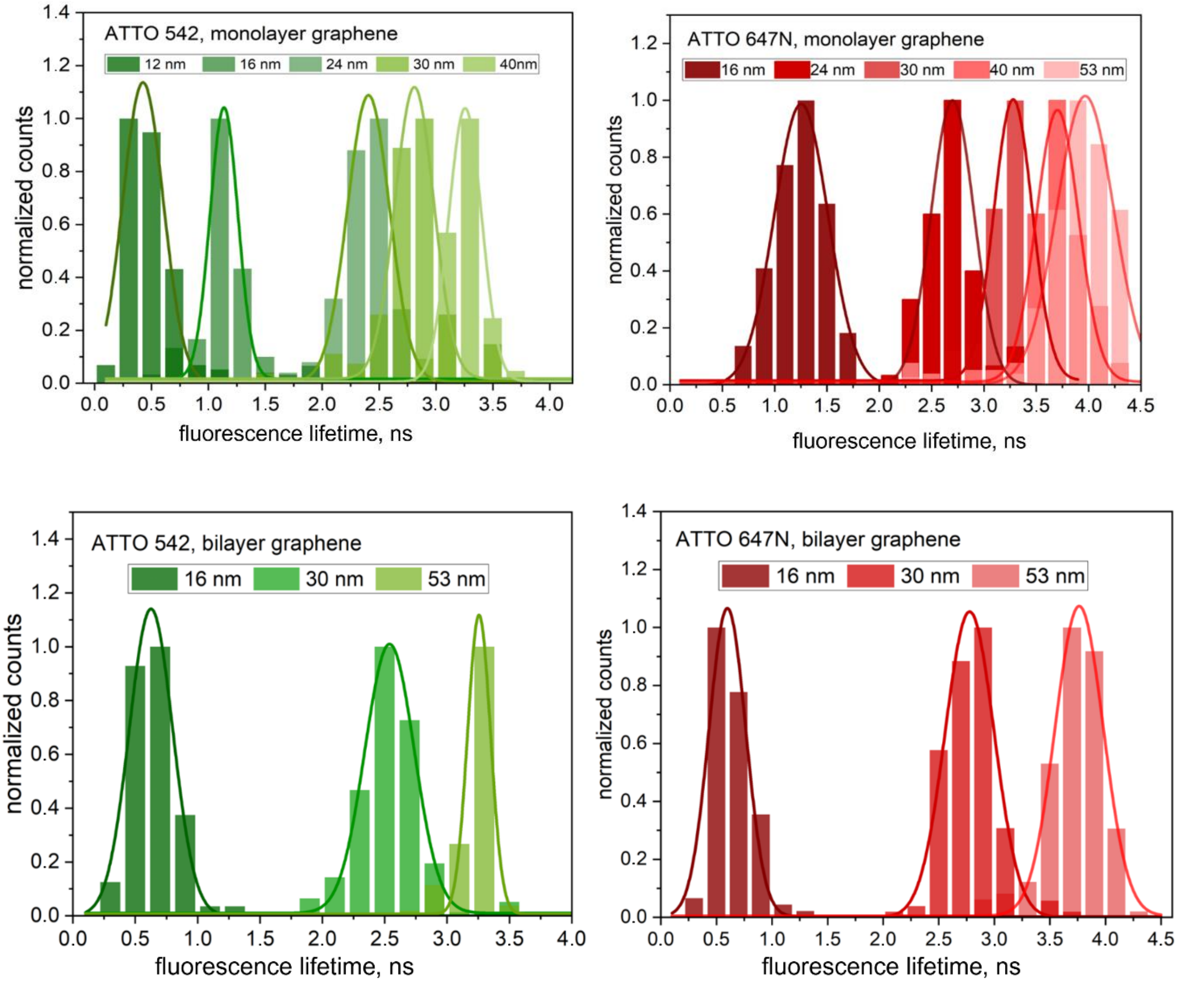

Figure 10.9 Histograms of the fluorescence lifetime of dye molecules ATTO 542 (green) and ATTO 647N (red) positioned in DNA origami nanostructures immobilized on a monolayer (top panel) and bilayer graphene (bottom panel) fitted with a Gaussian function.

The results obtained for monolayer graphene agree with those of previously published studies [3], [6], [20] However, a notable observation is that introducing additional graphene layers leads to enhanced fluorescence quenching, which matches findings presented by others [7], [8], [19], [23]. To better visualize the impact of the number of graphene layers on GET, fluorescence lifetime values were compared for identical distances between the graphene and the fluorophore for one type of DNA origami nanostructure immobilized on either monolayer or bilayer graphene (Figure 10.10).

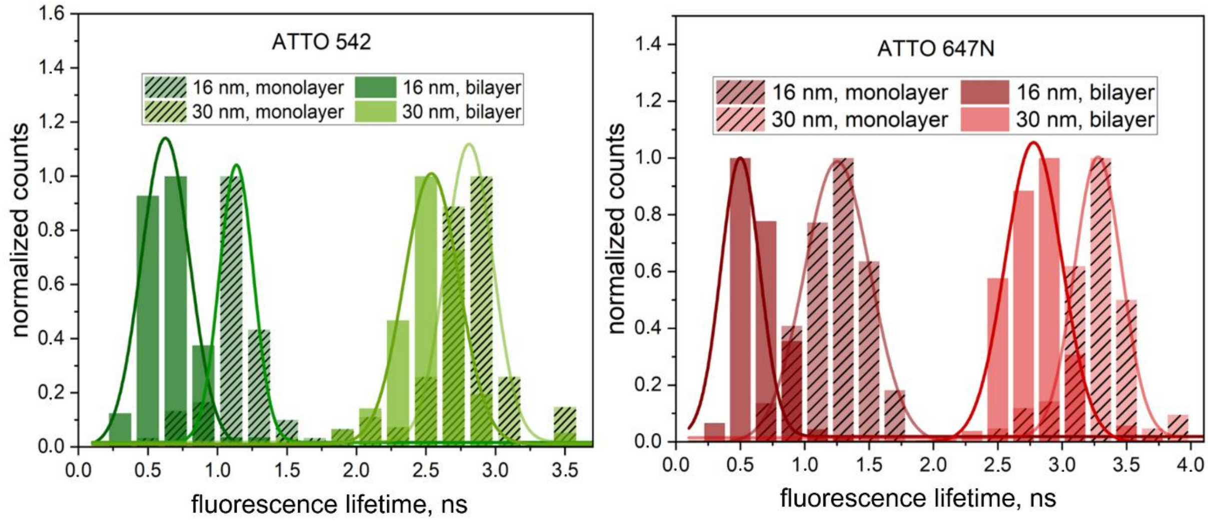

Figure 10.10 Histograms presenting the comparison between the fluorescence lifetime of dye molecules ATTO 542 (green) and ATTO 647N (red) positioned in DNA origami nanostructures immobilized on monolayer (dashed) and bilayer graphene fitted with a Gaussian function.

The data reveal that the impact of the second graphene layer on the energy transfer efficiency is more pronounced for the dye molecule positioned at a height of 16 nm. This observation is consistent with graphene energy transfer (GET) theory, which predicts that quenching efficiency is most sensitive near d_0, the characteristic distance at which 50% energy transfer efficiency occurs.

2.3.3. GET model for multilayer graphene

Building on the above results, we sought to develop a model incorporating the number of graphene layers (n) as a key factor influencing energy transfer from fluorophores to graphene. As described in the Introduction in Chapter 2.1, graphene energy transfer (GET) from a fluorescent emitter to graphene is determined by the distance between the graphene surface and fluorophore (d), energy transfer rates (k), and the structural characteristics of graphene layers. The dependency of η on the number of graphene layers emerges from fundamental physical principles underlying fluorescence quenching. Energy transfer efficiency quantifies the proportion of energy transferred from an emitter to the graphene acceptor relative to other competing depopulation pathways. Mathematically, it is defined by the energy transfer rates:

$$\eta = \frac{k_{GET}}{k_{GET} + \sum k_i} \tag{2.1}$$

where k_{GET} stands for the graphene energy transfer rate, and $\sum k_i$ represents all other depopulation rates unaffected by graphene.

The relation between k_{GET} and the emitter-graphene distance d is given by the following equation:

$$k_{GET} = \frac{1}{\tau_{ref}}\left(\frac{d}{d_0}\right)^4 \qquad (2.2)$$

Where τ_{ref} is the donor lifetime without the acceptor, and d_0 is the distance at which the energy transfer efficiency is 50%. Substitution of k_{GET} into the efficiency equation results in the following formula:

$$\eta = \frac{\frac{1}{\tau_{ref}}\left(\frac{d}{d_0}\right)^4}{\frac{1}{\tau_{ref}}\left(\frac{d}{d_0}\right)^4 + \sum k_i} \qquad (2.3)$$

The equation can be further simplified since $\tau_{ref} = 1/\sum k_i$, and it is reduced to:

$$\eta = \frac{1}{1 + \left(\frac{d}{d_0}\right)^4} \qquad (2.4)$$

Based on the assumption that the interaction between graphene layers is weak and the interlayer spacing is negligible, multilayer graphene can be modeled as a sum of individual monolayer contributions. Therefore, the energy transfer rate should scale linearly for n layers:

$$k_{GET} = n \cdot \frac{1}{\tau_{ref}}\left(\frac{d}{d_0}\right)^4 \qquad (2.5)$$

It results in the following modification of the formula describing energy efficiency:

$$\eta = \frac{n \cdot k_{GET}}{n \cdot k_{GET} + \sum k_i} = \frac{1}{1 + \frac{1}{n}\left(\frac{d}{d_0}\right)^4} \qquad (2.6)$$

The equation underscores the layer dependence, predicting an increase in energy transfer efficiency upon adding more graphene layers. Notably, when n = 1, the equation reduces to the abovementioned form (Equation 2.1, Chapter 2.1 of the Introduction).

To verify whether the model agrees with the experimental results, we calculated the energy transfer rate constants for monolayer, bilayer and trilayer graphene using the equation:

$$k_{GET} = \frac{1}{\tau_G} - \frac{1}{\tau_{ref}} \qquad (2.7)$$

This allowed us to analyze the ratio of energy transfer rates for multilayer graphene relative to monolayer graphene as a function of distance. For each dye and each distance measured on monolayer graphene, we normalized the energy transfer rate constant by the corresponding rate constant for monolayer graphene. The results are presented in Figure 10.11.

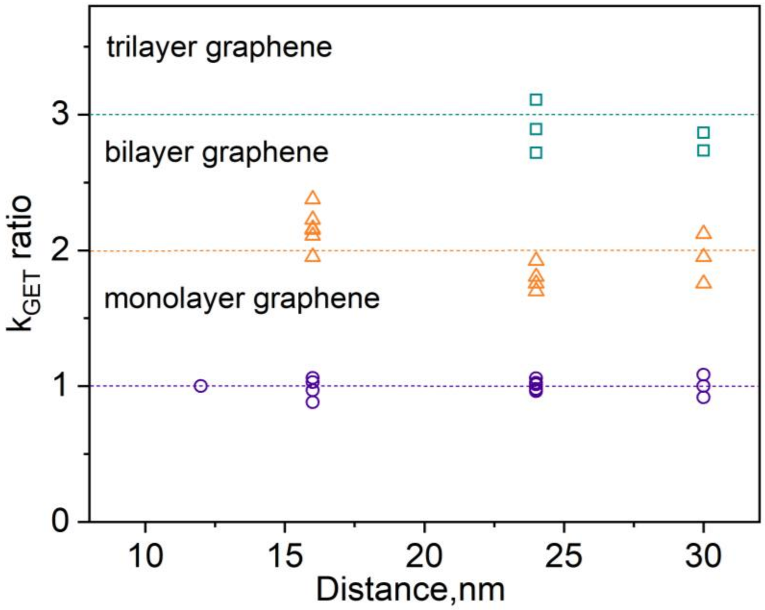

Figure 10.11 The ratio of the energy transfer rates of multilayer graphene to monolayer graphene as a function of the distance calculated from the fluorescence lifetimes registered on monolayer, bilayer, and trilayer graphene.

The results show that all data points consistently align at a ratio of one for monolayer graphene, two for bilayer graphene, and three for trilayer graphene, independent on the distance. This uniformity suggests that each additional graphene layer contributes equally to fluorescence quenching, with energy transfer rates being additive across layers. Consequently, multilayer graphene functions as a stack of independent monolayer graphene sheets, with each layer contributing an equivalent incremental quenching effect.

To further confront the proposed model against experimental data, the mean fluorescence lifetime (τ_G) values were acquired from colocalized emitters across all measured samples, with heights ranging from 12 to 53 nm. Figure 10.12 presents the mean fluorescence lifetime values and corresponding standard deviations for colocalized emitters on monolayer and bilayer graphene. The experimental data were fitted to the distance dependence curves using the following function:

$$\tau_G = \tau_{ref} \cdot \left(\frac{1}{1 + \left(\frac{d}{d_0}\right)^4} \right) \tag{2.8}$$

where τ_{ref} represents the fluorescence lifetime of the reference sample measured on glass. The mean reference fluorescence lifetimes averaged across all DNA origami nanostructures measured on glass were determined to be 3.27 ± 0.19 ns for ATTO 542 and 3.81 ± 0.15 ns for ATTO 647N. The parameter d_0 equals 17.7 ± 0.5 nm for ATTO 542 and 18.5 ± 0.7 nm for ATTO 647N [6].

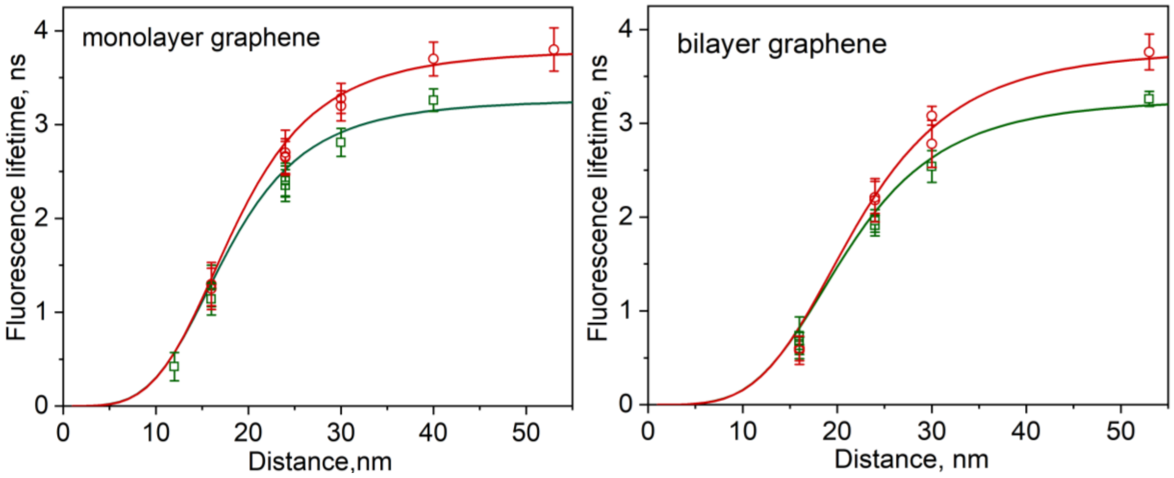

Figure 10.12 Mean fluorescence lifetimes of colocalized dye molecules within DNA origami nanostructures, along with their standard deviations. The lifetimes of ATTO 542 (green) and ATTO 647N (red) were analyzed as a function of their distance from the surface: monolayer graphene (left) and bilayer graphene (right).

The model fits in Figure 10.12 demonstrate good agreement with the experimental fluorescence lifetime values measured for both monolayer and bilayer graphene substrates. The results obtained for monolayer graphene are consistent with those of prior studies [6], [20].

The results obtained for trilayer graphene also fit into this trend, demonstrating a similar pattern (Figure 10.13).

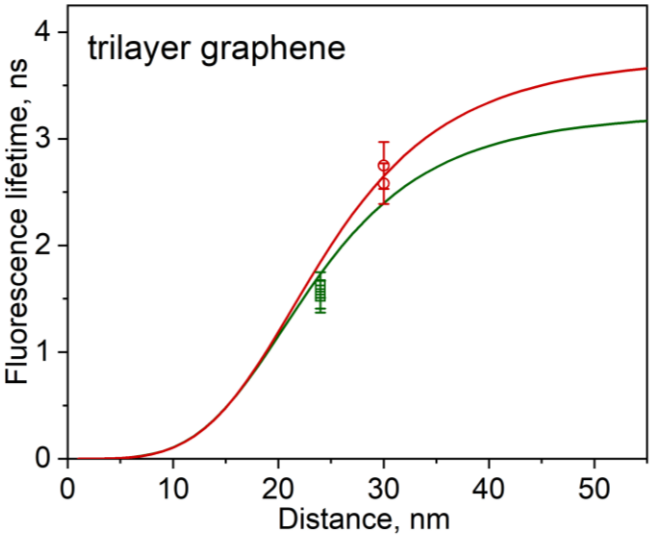

Figure 10.13 Mean fluorescence lifetimes of colocalized dye molecules within DNA origami nanostructures, along with their standard deviations. The lifetimes of ATTO 542 (green) and ATTO 647N (red) were analyzed as a function of their distance from the surface of trilayer graphene.

The results align closely with the calculated dependencies, further validating the accuracy of our model. While only two distances were tested for trilayer graphene, each distance was measured and verified through multiple independent experiments to ensure the reliability and consistency of the observed trends.

Nonetheless, challenges associated with sample preparation for trilayer graphene partially constrained the scope of tested distances. As the number of graphene layers increases, reproducibility becomes increasingly difficult due to the methodology of the layer-by-layer approach used for multilayer formation. Each additional layer introduces potential defects, such as wrinkles, holes, or misaligned stacking, which compromise the uniformity and quality of the samples. These factors collectively constrained the distances tested for trilayer graphene while allowing to observe and confirm the expected trends.

2.3.4. Probing Molecular Dynamics Using Monolayer and Bilayer Graphene Energy Transfer

The preceding chapter examined the effect of the number of graphene layers on graphene energy transfer (GET) efficiency. A theoretical model was introduced to describe the relationship between the number of graphene layers and the observed GET, with experimental results aligning closely with the model's predictions.

Building on these insights, this chapter expands the application of GET by utilizing multilayer graphene substrates in dynamic assays, creating a system capable of resolving dynamic processes over distances greater than those achievable with monolayer graphene. To investigate this expanded dynamic range in single-molecule biophysical experiments, we utilized pillar-shaped DNA origami nanostructures equipped with a protruding single-stranded DNA (ssDNA) "pointer" of 24 nucleotides (nt), labeled with indocarbocyanine Cy3B (the shorter name “Cy3B” will be used from now on) at its terminus.

To ensure the photostability of Cy3B, a combination of ROXS (reducing and oxidizing system) and an oxygen scavenging system was employed. Photostability is a measure of how well a fluorescent dye resists photobleaching and blinking under light exposure, enabling reliable and extended fluorescence imaging and measurements. Photostabilization protocol utilized two complementary buffers: the first consisted of an aqueous solution of aged Trolox and PCA (protocatechuic acid), referred to as PCA/Trolox12, while the second was a concentrated 50× Pyranose Oxidase-Catalase-Deoxygenated (PCD) buffer. For measurements, these buffers were mixed in a 1:50 ratio (50× PCD/Trolox12) to create the optimized stabilization environment [106], [107], [219].

There are several reasons behind using Cy3B in single-molecule studies of the dynamic bioassay. These are photostability, brightness, and environmental stability, among others. Cy3B is highly photostable, meaning it is less prone to photobleaching during prolonged illumination than ATTO 542. This is crucial for dynamic studies, where tracking a single molecule over time requires consistent fluorescence without degradation. Moreover, Cy3B, especially when paired with an appropriate stabilization system like ROXS, shows reduced blinking behavior compared to ATTO 542. This results in more reliable data for single-molecule dynamic studies. It is important since fluorescence blinking can hinder accurate tracing of the dynamic changes in the investigated system.

The pointer was positioned at 28 or 35 nm above the graphene surface (abbreviated as P28 and P35, respectively). Each pointer dynamically interacts with two docking sites, each located 7 nm above and below the pointer's default position on the DNA origami nanostructure. Additionally, the red dye (ATTO 647N) incorporated in all DNA origami nanostructures at 16 nm serves as a reference label to monitor the quality of graphene substrates and to ensure the number of graphene layers, providing the accuracy of fluorescence lifetime measurements. The scheme of the structure is illustrated in Figure 10.14. Both configurations of the pointer were measured on glass, monolayer, and bilayer graphene substrates using pulsed interleaved laser excitation at 532 and 639 nm.

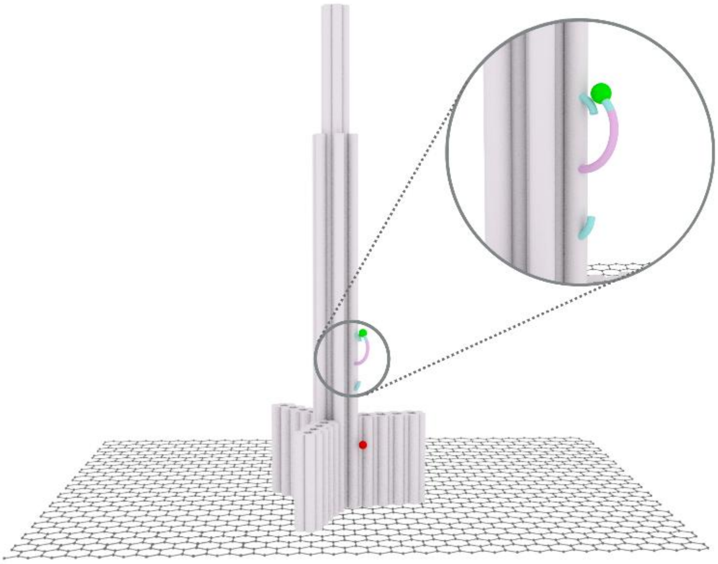

Figure 10.14 A schematic representation of the dynamic assay integrated into the pillar-shaped DNA origami nanostructure immobilized on the graphene substrate. The ssDNA pointer is positioned at a height of 35 nm above the substrate (depicted in purple and turquoise) and labeled with the Cy3B dye molecule (represented as a green sphere). The scheme presents the binding of the pointer to the upper biding site (turquoise) located 7 nm above the initial position. Additionally, the reference red dye ATTO 647N (red sphere) is placed at a height equal to 16 nm from the substrate.

At first, the fluorescence lifetime maps were measured on glass. The procedure was the same as in the studies described in the previous chapter (Chapter 2.3.1). The results indicate the correct folding of the DNA origami nanostructures, as evidenced by the presence of the dye molecules in both red and green channels. Additionally, they provide the reference values of the fluorescence lifetime of both dye molecules without the quencher (Figure 10.15).

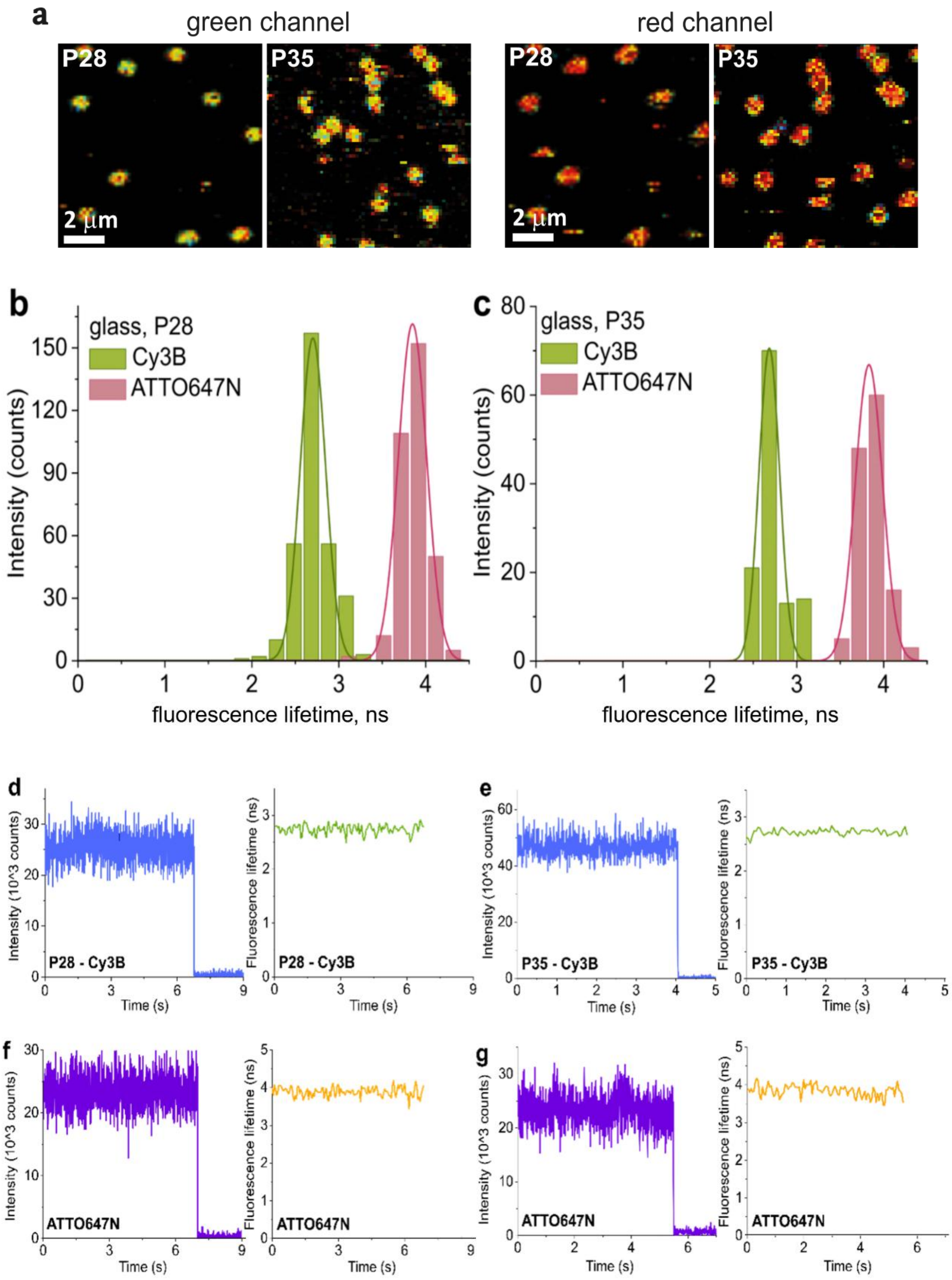

Figure 10.15 (a) Reference fluorescence lifetime intensity maps (10 × 10 mm) were obtained for pointers positioned at heights of 28 nm (P28) and 35 nm (P35). These pointers were labeled with the dyes Cy3B (red channel, left panel) and ATTO 647N (green channel, right panels) within DNA origami nanostructures immobilized on glass. (b, c) Histograms of fluorescence lifetimes for colocalized dye molecules Cy3B (green) and ATTO 647N (red), positioned at heights of 28 nm (b) and 35 nm (c) within pillar-shaped DNA origami nanostructures immobilized on glass, were fitted with Gaussian functions. The fluorescence lifetime of Cy3B equals to 2.70 ± 0.12 ns (b) and 2.69 ± 0.10 ns (c), while that of ATTO 647N was determined to be 3.85 ± 0.14 ns (b) and 3.83 ± 0.13 ns (c), (d-g) Examples of fluorescence intensity (blue and purple) and corresponding fluorescence lifetime (green and orange) time traces registered for ssDNA positioned at heights of 28 nm (P28, panels d and f) and

35 nm (P35, panels e and g). The ssDNA is labeled with the dye Cy3B (panels d and e) and incorporated into pillar-shaped DNA origami nanostructures immobilized on a glass surface. The colocalized dye ATTO 647N is positioned at a height of 16 nm (panels f and g).

Among the various possible heights suitable for investigating the dynamic assays, we selected 28 and 35 nm. Calculations based on Equation 2.9 reveal that a pointer positioned at 28 nm offers the most significant distinction in fluorescence lifetime between monolayer and bilayer graphene (Figure 10.16).

$$\eta = \frac{1}{1 + \frac{1}{n}\left(\frac{d}{d_0}\right)^4} \qquad (2.9)$$

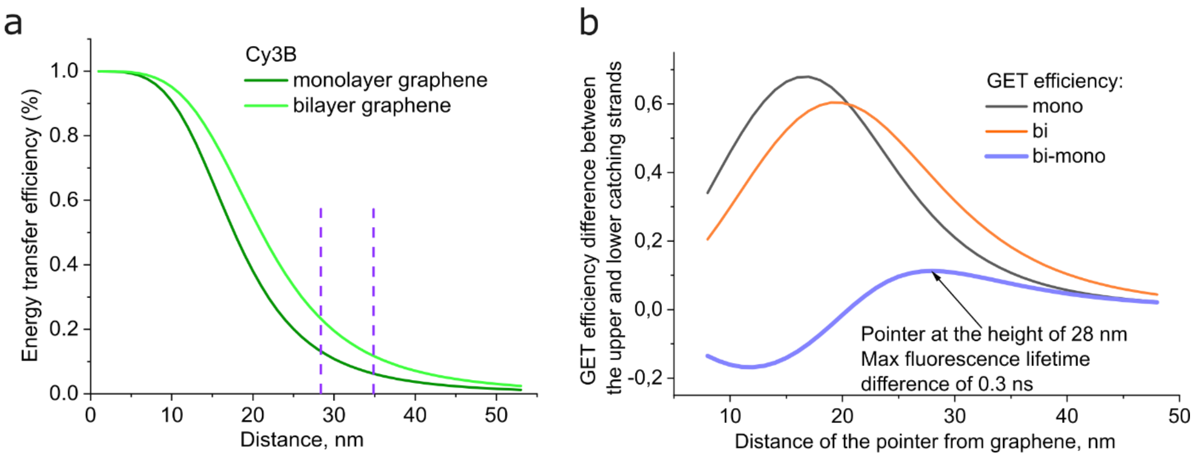

Figure 10.16 (a) Graphene energy transfer efficiency as a distance function was calculated using Equation 2.9 for monolayer and bilayer graphene. The purple dashed lines represent the heights of 28 nm and 35 nm, chosen for the investigation of dynamic assay systems. (b) calculated graphene energy transfer efficiency difference between the upper and lower catching strand (in the function of a distance) for monolayer and bilayer graphene. The purple (bi-mono) curve illustrates the difference between the GET of mono- and bilayer graphene (for the lower and upper position of the pointer), showing that at 28 nm, the difference between mono- and bilayer graphene is the highest yielding the maximum possible difference of the energy transfer efficiency value reaching 11% that corresponds to the 0.3 ns difference of the fluorescence lifetime.

Single-molecule fluorescence measurements were performed for both pointers incorporated into DNA origami nanostructures immobilized on monolayer and bilayer graphene to investigate the dynamic transitions between the two binding states. Fluorescence lifetime maps were recorded (Figure 10.17), followed by registering fluorescence intensity time traces for selected spots. These measurements allowed us to evaluate the fluorescence lifetime distributions and analyze the transitions between binding states.

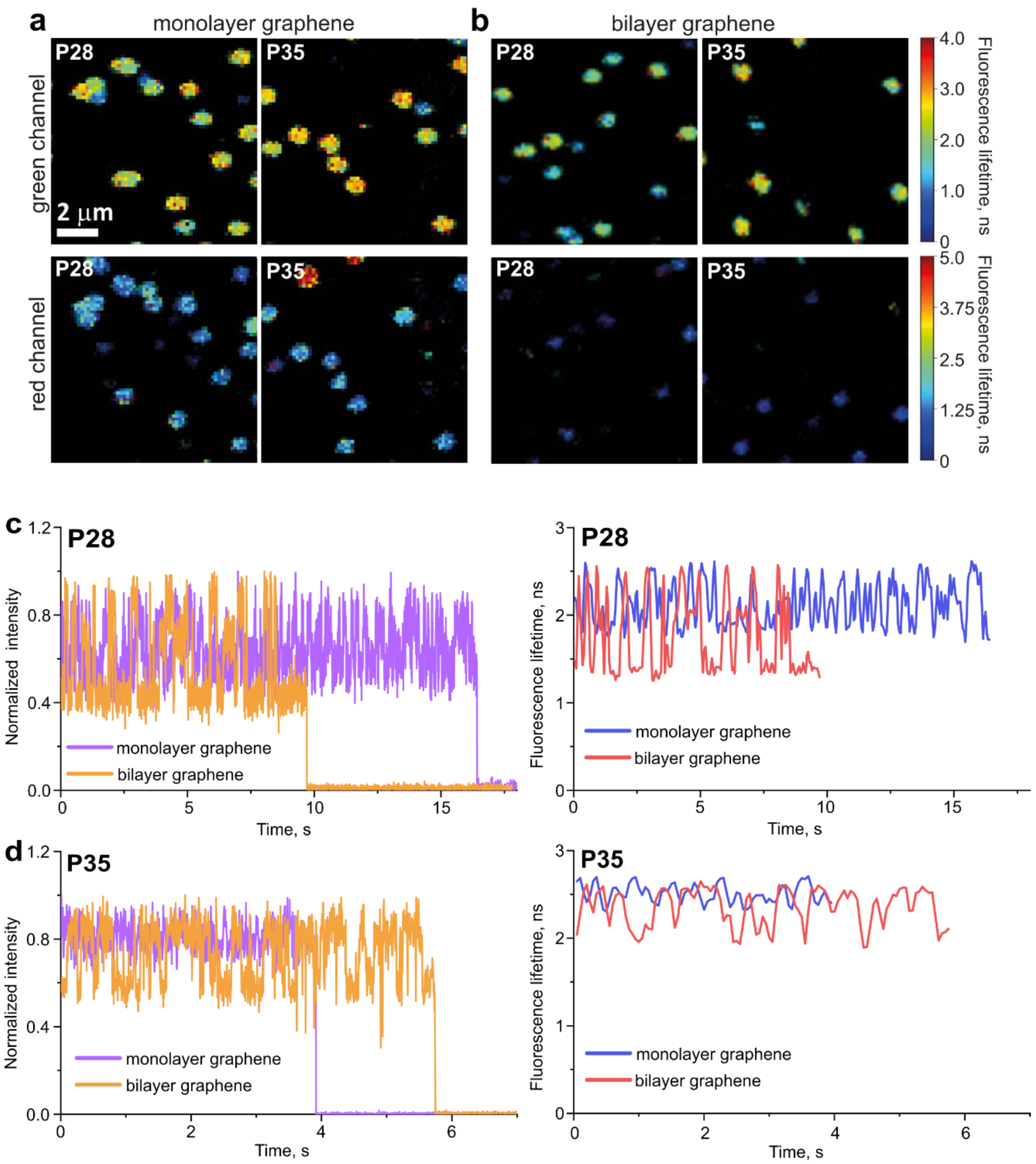

Figure 10.17 (a, b) Exemplary fluorescence lifetime intensity maps (10 × 10 μm) obtained for pointers positioned at heights of 28 nm (P28) and 35 nm (P35), labeled with the dye Cy3B (green channel, upper panels) in DNA origami nanostructures immobilized on monolayer (a) and bilayer (b) graphene. In all constructs, ATTO 647N, positioned at a height of 16 nm, was used as an internal reference to monitor the quality of the graphene (red channel, lower panels). Panels (c) and (d) present examples of measured fluorescence intensity (orange and purple traces) and the corresponding fluorescence lifetime (blue and red traces) time traces for the pointer assay (ssDNA) positioned at heights of 28 nm and 35 nm, labeled with the dye molecule Cy3B and incorporated into pillar-shaped DNA origami nanostructures immobilized on monolayer (purple to blue) and bilayer (orange to red) graphene.

While highly informative, fluorescence lifetime values capture a time-averaged view of molecular interactions and provide insights into energy transfer efficiency and quenching effects. However, the time traces reveal additional dynamic details, enabling the observation of transitions between molecular states. By examining the fluorescence intensity fluctuations and lifetime variations, it was possible to track binding kinetics and identify system heterogeneity.

Time traces allow the observation of how fluorescence changes over time, capturing dynamic processes such as molecular interactions, conformational changes, or environmental shifts in real time.

For P28, the transient binding of the pointer between the two binding sites can be resolved on both monolayer and bilayer graphene substrates (Figure 10.17c). Notably, in the case of bilayer graphene, the contrast — defined as the difference in fluorescence lifetime values between the two conformations — increases from approximately 0.7 to 1.0 ns.

In the case of P35, measured on monolayer graphene, the fluorescence time traces (Figure 10.17d) display intensity oscillations comparable to those recorded on glass (Figure 10.15), indicating a limited capacity to resolve the transient binding events. The histogram analysis confirms that the fluorescence lifetime values overlap, making it impossible to distinguish between the lower and upper binding conformations under these conditions. This limitation underscores the challenges of achieving sufficient resolution on monolayer graphene for DNA nanostructures positioned at greater distances (35 nm) from the graphene surface.

However, when the same P35 construct is immobilized on bilayer graphene, the transient binding events between the lower and upper binding sites become resolvable (Figure 10.17d). The fluorescence lifetime values alternate distinctly between 2.1 and 2.6 ns, indicating clear transitions between the two conformations. This improvement demonstrates the capacity of bilayer graphene to extend the measurable dynamic range and resolve molecular interactions that are challenging to observe on monolayer graphene. The enhancement observed with bilayer graphene can be attributed to its increased interaction surface, which amplifies energy transfer efficiency and improves sensitivity for detecting conformational changes.

These findings highlight the advantage of bilayer graphene over monolayer graphene in resolving transient molecular interactions, particularly for DNA nanostructures positioned at greater distances from the surface.

3. Graphene – hexagonal boron nitride heterostructures in single-molecule studies

Utilizing the optimized protocols for transferring and cleaning CVD graphene (Chapter 2 of the Methods), high-quality, ultraclean graphene-on-glass substrates were produced. These methodologies were further adapted to transfer hexagonal boron nitride (hBN) from copper foil onto glass or graphene, depending on whether hBN served as a substrate, a protective layer, or both. The initial objective was to determine whether DNA nanostructures – specifically DNA origami nanostructures and ssDNA/dsDNA hybrid – could be immobilized and remain stable on hBN surface. Subsequent investigations explored how atomically smooth hBN, free of charge traps and dangling bonds, enhances the quality of overlaying graphene and influences its acceptor properties when used as a substrate. In a similar vein, hBN was applied on top of graphene to examine its effect on the interaction between single dye molecules and the graphene surface.

3.1. Preparation of high-quality hBN-on-glass

Monolayer hBN on copper foil was transferred on a glass coverslip using the previously elaborated protocol (Chapter 2 of the Methods). Despite similarities in the structure and the growing process (both materials are grown on Cu foil using chemical vapor deposition) between graphene and hBN, the same transfer and cleaning protocol did not apply to hBN. It yielded ununiform samples, as presented in Figure 11.1.

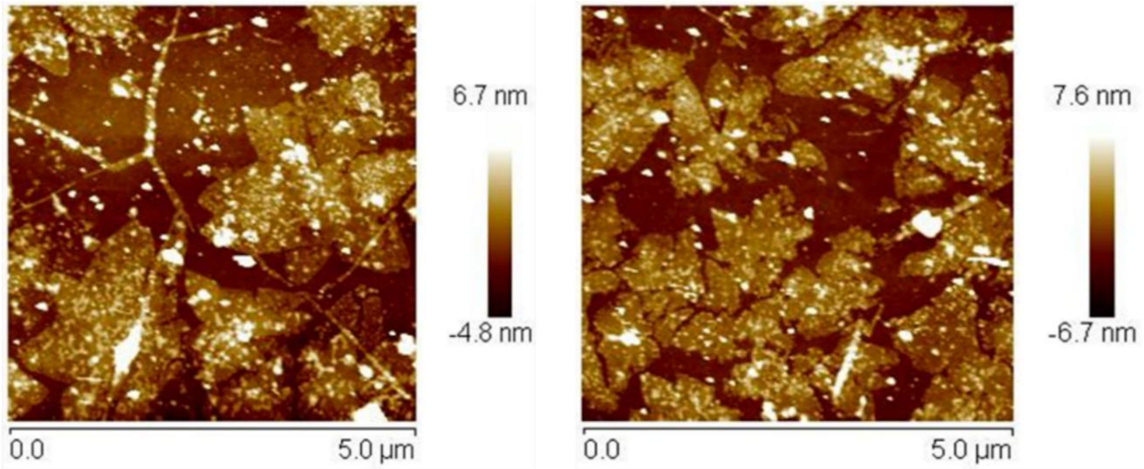

Figure 11.1 AFM images of hexagonal boron nitride prepared according to the procedure optimized for graphene [4].

Therefore, finding the "weakest spot" in the procedure was crucial. To this end, SEM imaging was performed on the pristine sample (PMMA-coated hBN on copper foil) (Figure 11.2a). Following the removal of the PMMA layer, SEM imaging was repeated (Figure 11.2b). The results indicated that neither the sample itself (initial quality of the sample purchased from Merck) nor the PMMA layer negatively impacted the quality of the 2D material.

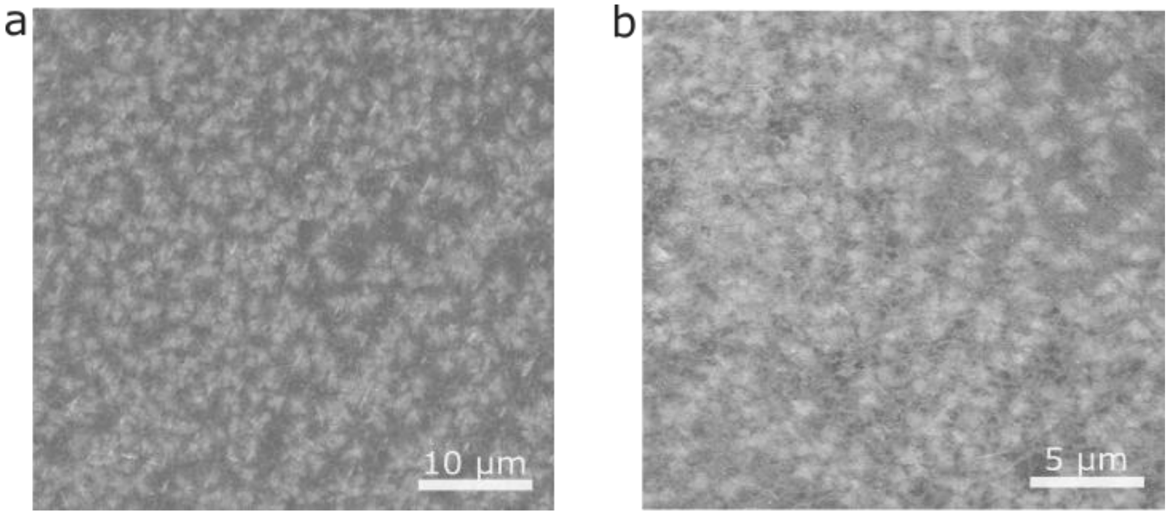

Figure 11.2 SEM images of hexagonal boron nitride on copper foil (a) with PMMA layer on top, (b) after PMMA removal, at different magnifications.

Based on the results discussed above, the etching of the copper foil was identified as a critical limiting factor in the transfer process of hBN, resulting in damage to the hBN layer. Several strategies were explored to address this issue. In the first attempt, the copper substrate was etched using iron chloride (1 mol/L), with samples immersed in the solution for 12 hours. Following etching, the substrates were thoroughly rinsed three times with deionized water, following the protocol from Zhou et al., 2013. However, this method did not significantly improve the quality of the hBN layer. As with the previous method, the rinsing involved transferring the samples into fresh deionized water using glass coverslips. An alternative technique was implemented to refine the process further [221]. In this method, Kapton tape was used to facilitate the rinsing of hBN (coated with PMMA) in deionized water, as illustrated in Figure 11.3. Afterward, the PMMA was removed using acetone, followed by rinsing with isopropyl alcohol. Despite these modifications, the results remained unsatisfactory, as the quality of the hBN layer did not show significant improvement.

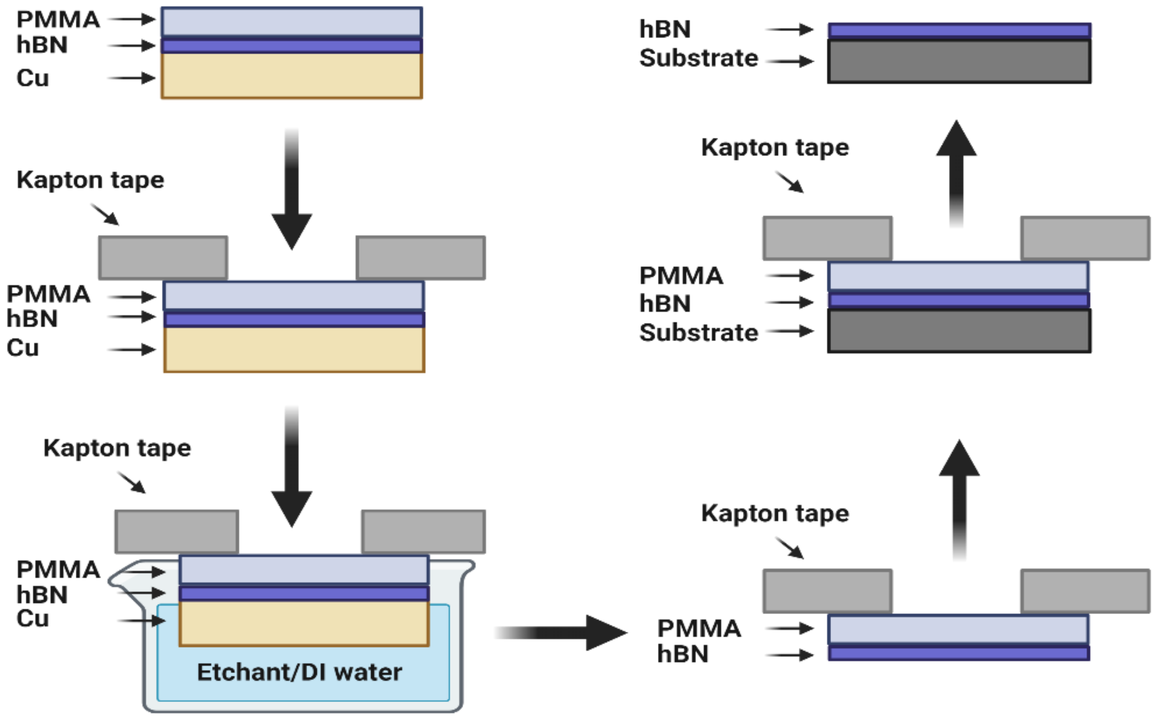

Figure 11.3 Schematic representation of the hexagonal boron nitride (hBN) transfer. To ensure the integrity of the stacking sequence and prevent damage to the sample, an additional thick layer of poly (methyl methacrylate) (PMMA) was applied to the hBN/copper foil substrate (which was pre-coated with a thin PMMA layer by the supplier). This was achieved through spin-coating at a 7% PMMA solution concentration, with a rotational speed of 2500 rpm for 60 seconds. Subsequently, a Kapton tape frame was affixed to the PMMA/hBN/Cu assembly to facilitate the dry transfer process. After etching the copper foil and performing the necessary rinsing steps, the PMMA/hBN stack was carefully retrieved from deionized water and dried at 60 °C for 1 hour. Finally, the PMMA layer was removed by dissolution in acetone, followed by rinsing with isopropyl alcohol (IPA) [221].

Since damage to the hBN layer appeared unavoidable under the transfer protocols explored thus far, a commercially available 'trivial transfer hBN' (tt-hBN) kit was utilized and tested in subsequent experiments. The term tt-hBN refers to a CVD-grown hBN layer, pre-coated with PMMA and prepared for direct transfer onto any substrate without the need for an etching process. In this case, the supplier pre-removed the copper foil, and the hBN is provided on a polymer support that can be easily detached. To handle this sample, we followed the transfer and cleaning procedures recommended by the supplier, as illustrated schematically in Figure 11.4 and Figure 11.5.

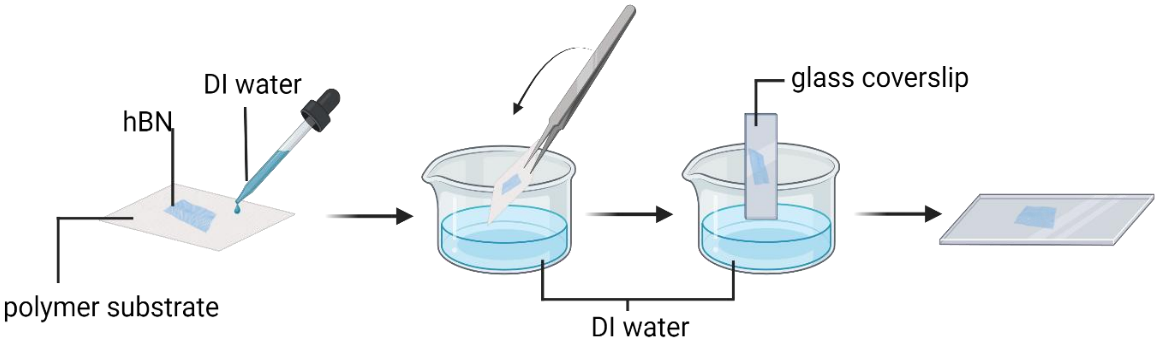

Figure 11.4 Schematic representation of the transfer protocol of tthBN that ACS Material recommends. A water droplet is added to the polymer substrate around the tthBN film, avoiding direct contact with hBN. The hBN layer can roll up if the droplet is on the edge. After the polymer substrate absorbs the water, the sample is carefully picked up with tweezers and immersed in DI water as slowly as possible. Otherwise, the hBN layer may roll up. Once hBN is released from the substrate, it is left for 2 hours to be sure it is fully soaked before the transfer to the new substrate. After this time, hBN can be transferred to the new substrate, such as a glass coverslip. Created with BioRender.com.

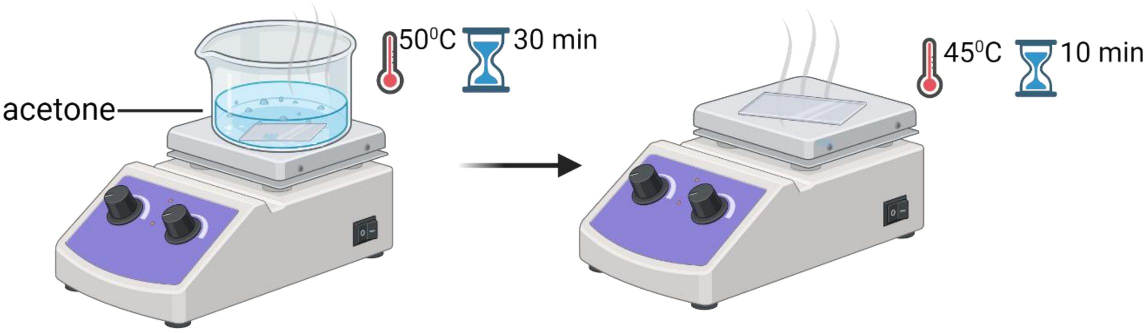

Figure 11.5 Schematic representation of the cleaning protocol of tthBN that ACS Material recommends. The substrate is immersed in the acetone preheated to 50^0C. After 30 minutes, when PMMA is rinsed off, the substrate is baked on a hotplate at 45^0C for 10 minutes. Created with BioRender.com.

The imaging performed with Raman spectroscopy (Figure 11.6) and scanning electron microscopy (Figure 11.7) were used to verify the quality of the hBN substrate.

Raman spectroscopy was performed on 'trivial transfer hBN' at two stages: first, on the pristine sample supported by the polymer substrate as received from the supplier, and then after its transfer onto a glass coverslip. To aid in interpreting the spectra, reference Raman spectra of the polymer substrate and PMMA were also acquired, as shown in Figure 11.6. The Raman peak at approximately 1370 cm^{-1}, characteristic of hexagonal boron nitride (hBN), is assigned to the E_2g mode, which corresponds to the in-plane vibrational motion of boron and nitrogen atoms within the hexagonal lattice [222].

The Raman spectra provide insights into the structural integrity and transfer process of the hBN layer (Figure 11.6). The E_2g peak of hBN on the polymer substrate is sharp and well-defined, indicating minimal strain and high crystallinity in the pristine material. However, after transferring the hBN onto a glass coverslip, subtle broadening and a slight shift of the E_2g peak are observed. These changes suggest the introduction of mechanical strain or interaction with the underlying glass substrate during the transfer process. The comparison with the polymer and PMMA spectra confirms that these additional features are not artifacts from the residual polymer but rather intrinsic to the hBN-glass system. The data further highlight the robustness of the hBN lattice structure, as the E_2g peak remains prominent and distinct in all measurements, demonstrating that the essential properties of hBN are preserved during the transfer.

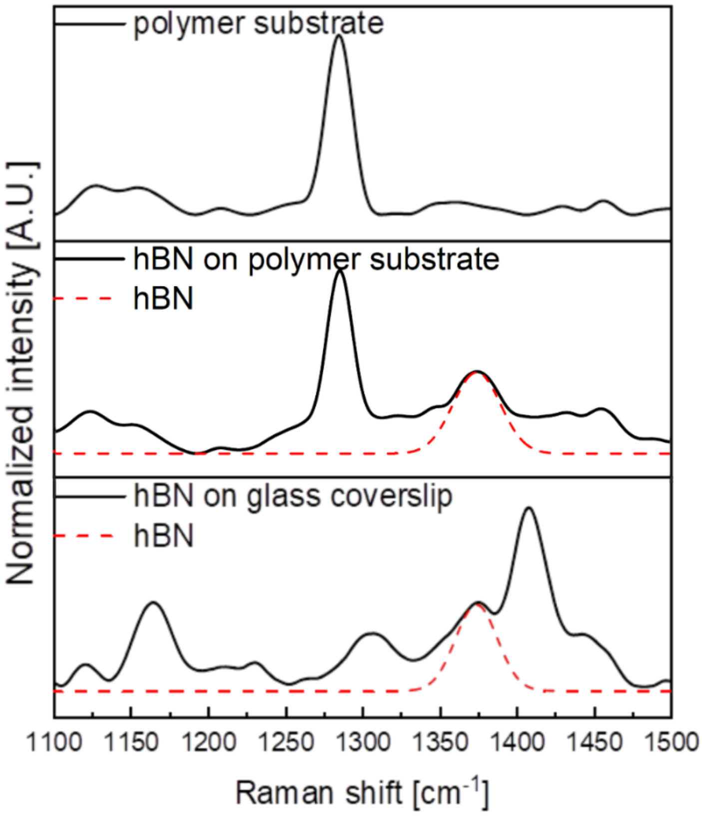

Figure 11.6 Raman spectra of the polymer substrate (top), the tthBN on polymer substrate (middle), and tthBN transferred on glass coverslip (bottom). The red dotted line in middle and bottom panels represents the Raman signal attributed to hBN.

Additionally, SEM images were systematically acquired from multiple locations across the sample to assess the effectiveness of the applied transfer and cleaning protocols for hBN (Figure 11.7). Three independent samples were tested to ensure the reliability and reproducibility of the results.

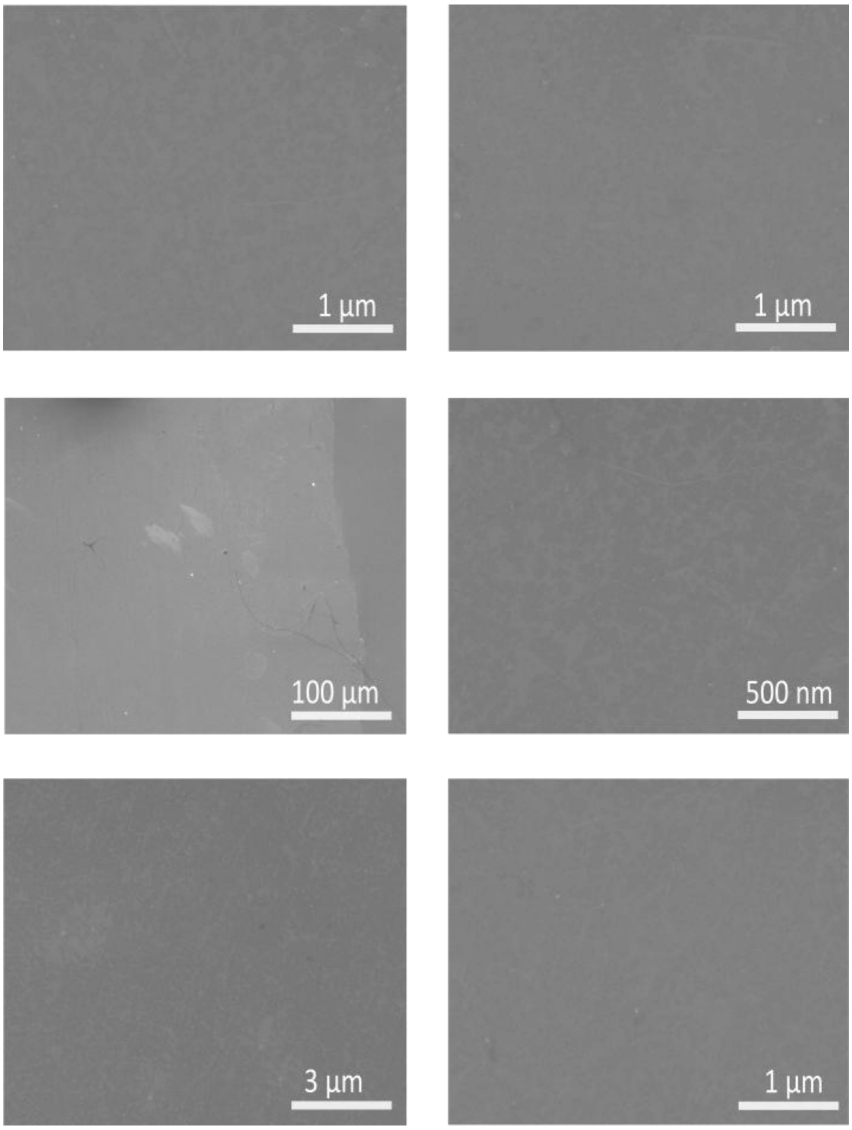

Figure 11.7 SEM images of hexagonal boron nitride at different magnifications.

The results reveal that the surface of hexagonal boron nitride is free from any visible defects or impurities, demonstrating the success of the employed procedures.

This chapter highlighted the significant challenges in obtaining high-quality hexagonal boron nitride (hBN) on glass coverslips. Before moving forward with the fabrication of heterostructures comprising hBN and graphene, it is essential to investigate the interactions between hBN and DNA nanostructures. This study is crucial, as this project's primary objective is to develop platforms based on hBN and graphene that will serve as substrates for the immobilization of DNA nanostructures. Ensuring the stability and preservation of the individual components and their properties is vital to maintaining the integrity of the final construct. Therefore, a comprehensive understanding of the interaction between hBN and DNA nanomaterials is necessary to guarantee that the assembly process does not compromise the desired performance of the system.

3.2. DNA nanostructures immobilized on hBN

Chapter 6.3.3 of the Introduction provides an analysis of the interactions between hexagonal boron nitride (hBN) and both single- and double-stranded DNA, placing these findings in the context of other widely studied two-dimensional (2D) materials, such as graphene, molybdenum disulfide (MoS_2), and tungsten disulfide (WS_2). This chapter highlights the most crucial aspects of the hBN implementation in this context.

Graphene and hexagonal boron nitride (hBN) have similar crystal structures and uniquely interact with biomolecules (Introduction, Chapter 6.3.1). However, their interactions with DNA molecules differ significantly. Notably, hBN demonstrates a strong affinity for nucleotides, with an average interaction energy of -29 kcal mol^{-1} per nucleotide [175], compared to the approximately -23 kcal mol^{-1} per nucleotide interaction energy observed for graphene. This higher affinity for DNA on hBN is attributed to the stacking of nucleobases on the surface of hBN [173]. These strong interactions have been harnessed in nanopore sequencing applications, where they reduce DNA translocation time, improving the temporal resolution necessary for accurate DNA sequencing [182].

Furthermore, the interaction of hBN with double-stranded DNA (dsDNA) shares certain similarities with graphene. Specifically, while hBN shows a strong affinity for single-stranded DNA (ssDNA), its interaction with dsDNA is notably weaker. Nevertheless, mathematical models suggest that the binding affinity between hBN and dsDNA surpasses that observed for other 2D materials, such as graphene, MoS_2, or WS_2 [181]. Despite these insights, the interactions between hBN and more complex DNA constructs remain largely unexplored.

This chapter aims to fill this gap by investigating the immobilization of DNA nanostructures on hBN. The methodology used for hBN follows the established protocol for immobilizing DNA nanostructures on graphene (as outlined in Chapter 2, Methods), with the procedures consistent with the initial tests conducted to achieve high-quality hBN on glass substrates. In the experiments presented here, a pillar-shaped DNA origami nanostructure – functionalized with the red dye ATTO 647N was successfully immobilized on the surface of hBN.

The detailed procedure for sample preparation and single-molecule experiments utilizing a fluorescence confocal microscope setup is thoroughly outlined in Chapter 1 of the Results. A brief summary of the key steps is provided here. The experiment began by placing a silicon chamber onto the hBN-coated glass coverslip platform. The chamber was then filled with a buffer solution containing pillar-shaped DNA origami nanostructures functionalized with ATTO 647N and pyrene molecules at a concentration of 50 picomolar. After incubation for approximately three minutes, fluorescence intensity mapping was performed using dedicated software written in LabVIEW to assess the distribution and concentration of the nanostructures. Once the fluorescence signal confirmed that the dye molecules were evenly distributed, without aggregation, and the number of individual points met the required criteria, the sample was washed with 1x TAE buffer containing 12 mM $MgCl_2$.Subsequently, the spots representing single molecules were selected on the fluorescence intensity maps, and their fluorescence lifetimes were measured using Becker & Hickl software.

Fluorescence lifetime data were recorded for more than 200 single dye molecules. The results were consistent with those obtained from reference sample measurements performed on glass (Figure 11.8). Given the dielectric nature of hBN, it was hypothesized that the substrate would not significantly alter the photophysical properties of the dye molecules. The recorded fluorescence lifetimes supported this assumption, as no substantial deviations were observed compared to the glass reference measurements. This indicates that hBN provides an inert and stable platform for immobilizing DNA nanostructures, preserving their intrinsic optical properties. The results underscore the advantages of using hBN as a substrate in single-molecule experiments. Unlike metallic substrates, which can introduce quenching or energy transfer effects, hBN's dielectric properties minimize such interactions, making it an ideal choice for applications requiring precise optical measurements. Furthermore, the atomically flat surface of hBN facilitates uniform adsorption of DNA nanostructures, enhancing reproducibility and reducing variability in experimental results. These findings validate the use of hBN as a reliable platform for fluorescence-based experiments, paving the way for further exploration of its potential in advanced biosensing and molecular imaging applications.

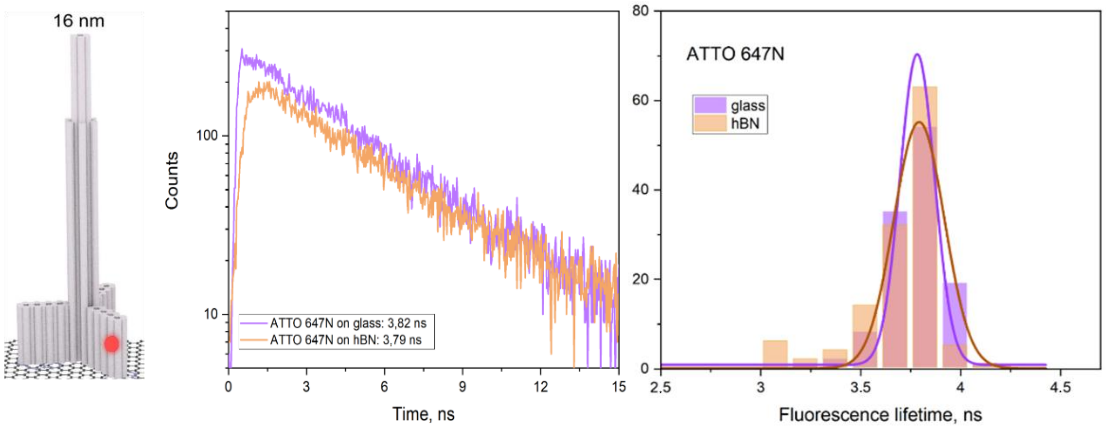

Figure 11.8 Measurements of the fluorescence lifetime of ATTO 647N dye molecules in the pillar-shaped DNA origami nanostructures immobilized on hBN compared with analogical measurements on glass (215 dye molecules positioned at 16 nm). (a) Exemplary fluorescence decays of dye molecules positioned in DNA origami nanostructures immobilized on glass (🟪) and hBN (🟧) fitted with the monoexponential function. The fluorescence lifetime of ATTO 647N on glass and hBN is equal to 3.82 ns and 3.79 ns, respectively. (c) Histograms fitted with a Gaussian function of the fluorescence lifetime. The mean fluorescence lifetime of ATTO 647N on glass (🟪) equals 3.82 ± 0.09 ns, and 3.79 ± 0.12 ns for ATTO 647N on hBN (🟧).

3.3. Van der Waals heterostructure formation

As previously described, this project also aimed to fabricate a heterostructure composed of monolayer graphene and hexagonal boron nitride (hBN). Two configurations were tested, where hBN was either placed as the top or bottom layer. The wet transfer procedures described previously (Chapter 3.1, Results) were applied to achieve this. Namely, the hBN layers were transferred onto glass or graphene substrates according to the transfer protocol recommended by ACS Material. In contrast, graphene was transferred using the protocol described in the Methods section. A schematic illustration of the heterostructure formation process is shown in Figure 11.9. Following a layer-by-layer approach similar to that used for multilayer graphene formation, the heterostructures were successfully fabricated, with both configurations exhibiting promising results for further exploration of their properties.

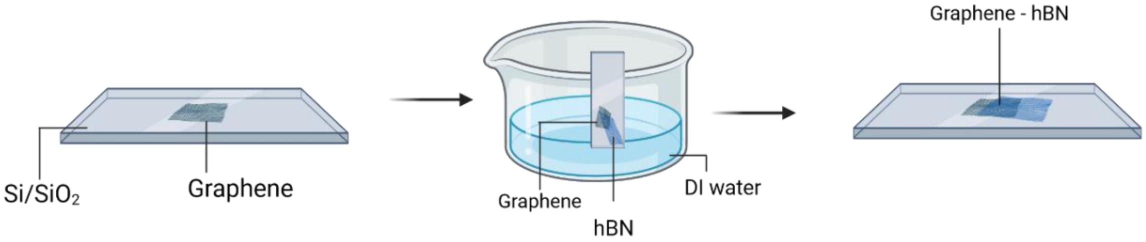

Figure 11.9 Schematic representation of the graphene/hBN heterostructures formation.

Both types of heterostructures were employed as platforms for the immobilization of DNA origami nanostructures. As a first step, similar to the studies on multilayer graphene, we examined the surface topography of the fabricated platforms. Three independent samples, representing both configurations of heterostructures, were imaged using scanning electron microscopy (SEM). Multiple locations across each sample were analyzed, and as illustrated by the exemplary images in Figure 11.10, the samples were free of breakages, defects, or impurities. These results indicate that the transfer procedures effectively preserved the integrity of the heterostructures, providing a suitable foundation for subsequent experiments involving DNA origami immobilization.

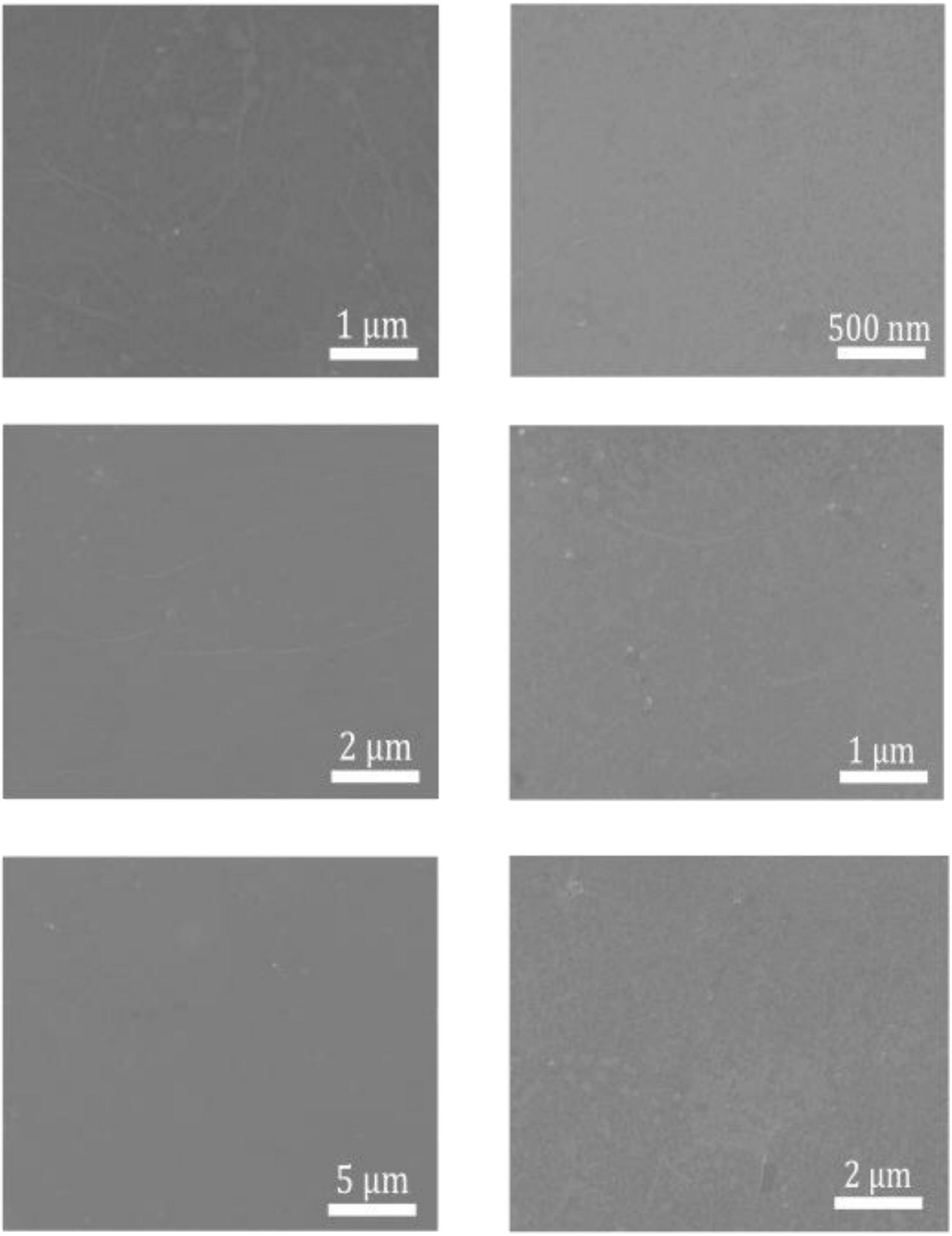

Figure 11.10 SEM images of graphene/hBN heterostructure configurations at different magnifications. (left) graphene as a top layer (hBN on bottom), and (right) graphene as a bottom layer (hBN on top).

3.4. Graphene-hBN heterostructures for single-molecule fluorescence studies

In the next step, these platforms were used to immobilize the pillar-shaped DNA origami nanostructure, labeled with an ATTO 647N dye molecule positioned at the height of 16 nm (the same nanostructure was used in the experiments on glass and hBN). Fluorescence lifetime time traces were recorded for over 800 individual dye molecules and compared with the values obtained from graphene-based measurements, which serve as the reference in this study. The experiments on graphene and on both types of heterostructures were conducted in precisely the same manner as the measurements on hBN that were described before (Chapter 3.2, Results).

Figure 11.11 presents a comparative analysis of the fluorescence lifetime values of the ATTO 647N dye molecules in the pillar-shaped DNA origami nanostructures immobilized on graphene (green) and the heterostructure (yellow) in which hBN serves as the substrate for graphene. The first histogram shows the distribution of fluorescence lifetimes recorded for individual dye molecules. The second histogram depicts the corresponding distances between the dye molecules and the graphene substrate, calculated from the fluorescence lifetime data using a theoretical model of graphene energy transfer presented before (Chapter 2.1, Introduction). These distances were calculated by correlating the measured fluorescence lifetimes with established decay-distance relationships for graphene-induced quenching. The results conclusively demonstrate the stability of DNA origami nanostructures on the heterostructure. The deposition of graphene onto hexagonal boron nitride (hBN) does not appear to significantly affect the graphene energy transfer (GET) efficiency, as the measured values are nearly identical to those obtained from the reference samples (measurements on graphene). This suggests that, within the sensitivity limits of the experimental setup, the deposition of graphene on hBN does not alter the acceptor properties of graphene. Moreover, no substantial differences in graphene quality were observed after its transfer onto hBN, compared to the results obtained for graphene-on-glass substrates.

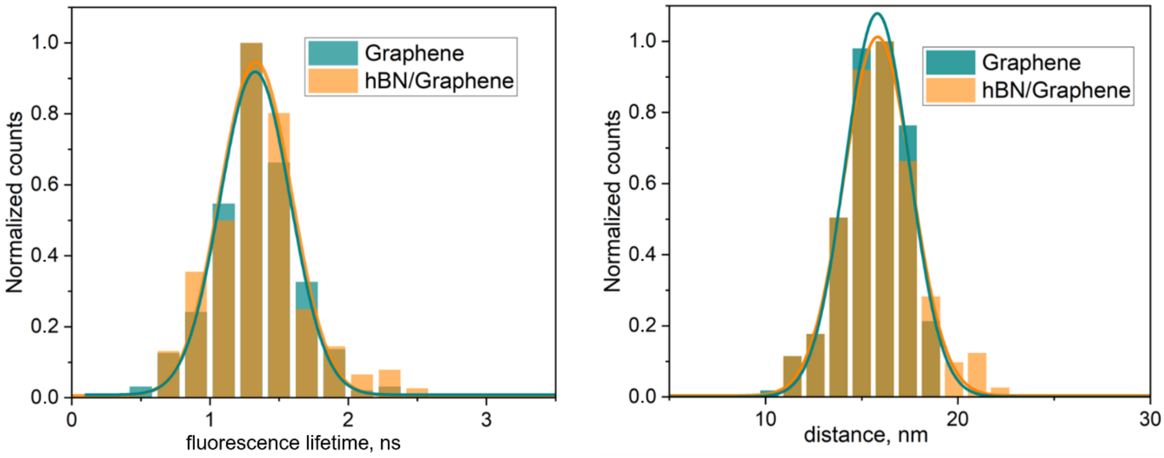

Figure 11.11 Histograms of the ATTO 647N dye molecules in the pillar-shaped DNA origami nanostructures immobilized on graphene (green) and the heterostructure (yellow) in which hBN serves as the substrate for graphene. Histograms fitted with a Gaussian function of the fluorescence lifetime (a). The mean fluorescence lifetime of ATTO 647N on graphene (🟩) equals 1.32 ± 0.11 ns and 1.33 ± 0.09 ns for ATTO 647N on hBN (top) – Graphene (bottom) (🟧). (b) Histograms fitted with a Gaussian function of the distance between graphene and the single dye molecule, calculated from the fluorescence lifetime values. The mean value of the distance between graphene and ATTO 647N (🟩) equals 15,81 ± 0.04 nm and 15.82 ± 0.08 ns for ATTO 647N on hBN (bottom) – Graphene (bottom) (🟧).

As discussed previously in Chapter 1, which focuses on single-molecule experiments, the quality of graphene can be inferred indirectly through the variability in the experimental data. Specifically, a narrower distribution of results indicates higher graphene quality and structural stability of the incorporated DNA origami nanostructures. While other factors may influence the system's overall quality, the high reproducibility of our samples allows us to reasonably attribute the primary variable affecting the outcome to the change in substrate from glass to hBN. The consistency of these results across multiple samples further supports the idea that introducing hBN does not undermine the inherent properties of graphene.

Figure 11.12 illustrates the data obtained for the reversed configuration. The deposition of hBN on graphene results in a slight shift in fluorescence lifetime value. The observed shift corresponds to an approximate 0.3 nm increase in the distance between the graphene and the dye molecules, suggesting that the monolayer of hBN acts as an ultra-thin spacer, increasing the separation between the dye and the graphene surface. Specifically, the hBN layer behaves as a buffer between graphene and the dye molecules, reducing the direct interaction and partially mitigating the quenching effect typically observed with graphene alone. To further validate this, a second layer of hBN was transferred on top of the existing hBN layer. The results obtained for a platform with bilayer hBN were consistent with the monolayer hBN data, as the distance between the dye molecules and the graphene effectively doubled.

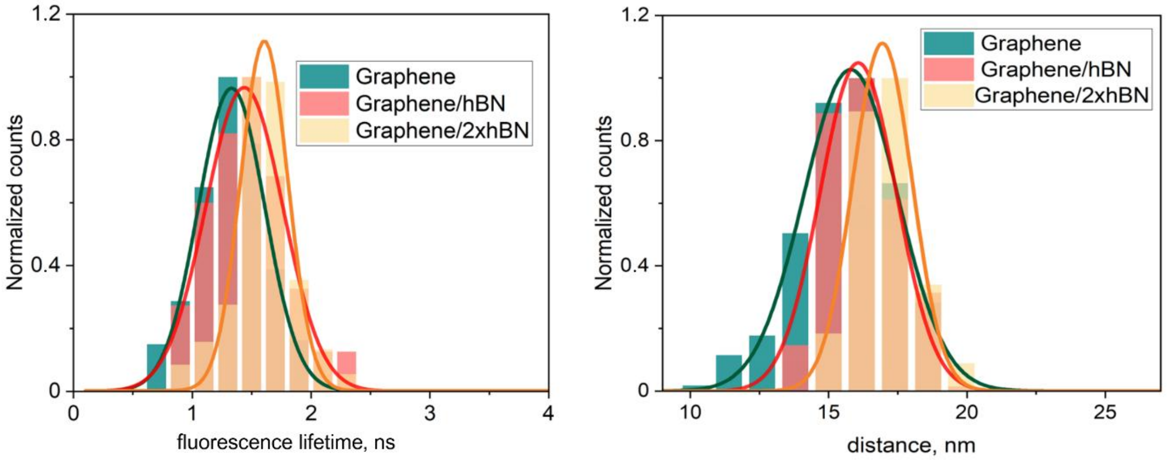

Figure 11.12 Histograms of the ATTO 647N dye molecules in the pillar-shaped DNA origami nanostructures immobilized on graphene (green), heterostructure with monolayer hBN (red) and bilayer hBN (yellow) in which hBN is deposited on top for graphene. Histograms fitted with a Gaussian function of the fluorescence lifetime (a), and of the distance between graphene and the single dye molecule, calculated from the fluorescence lifetime values (b). The mean fluorescence lifetime of ATTO 647N on graphene (🟩) equals 1.32 ± 0.11 ns, 1.43 ± 0.08 ns for ATTO 647N on Graphene (bottom) – hBN (top) (🟥), and 1,61 ± 0.14 ns for Graphene (bottom) – bilayer hBN (top) (🟧). Histograms fitted with a Gaussian function of the distance between graphene and the single dye molecule, calculated from the fluorescence lifetime values. The mean graphene – ATTO 647N on graphene (🟩) equals 15.81 ± 0.04 ns, 16.07 ± 0.06 ns for ATTO 647N on Graphene (bottom) – hBN (top) (🟥), and 16.94 ± 0.12 ns for Graphene (bottom) – bilayer hBN (top) (🟧).

Building on the findings from Figure 11.12, which suggested that hBN acts as a spacer reducing dye-graphene interactions (Figure 11.13). It is presented to demonstrate the effect of hBN in the studied constructs more clearly. This figure highlights the mean fluorescence lifetime values and their corresponding standard deviations for emitters on three platforms: monolayer graphene, heterostructure with monolayer hBN, and heterostructure with bilayer hBN. The data were fitted to the theoretical distance-dependence curve using Equation 2.8. The progressive increase in fluorescence lifetime underscores the impact of hBN as an ultra-thin buffer. This trend demonstrates the effectiveness of hBN in mitigating fluorescence quenching, primarily by increasing the spatial separation between the dye molecules and the graphene surface.

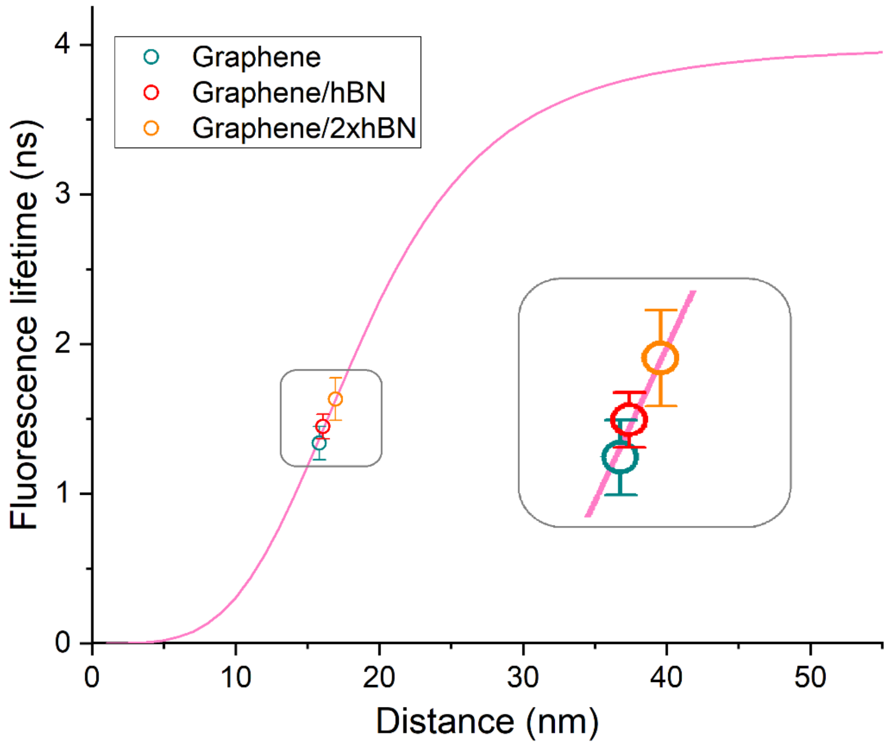

Figure 11.13 The mean fluorescence lifetime values and corresponding standard deviations for colocalized emitters on monolayer graphene (⬛), heterostructure with monolayer hBN on top of graphene (🟥), and heterostructure with bilayer hBN on top of graphene (🟧). The experimental data were fitted to the distance dependence curves using Equation 2.8. The mean fluorescence lifetime of ATTO 647N on graphene (⬛) equals 1.32 ± 0.11 ns, 1.43 ± 0.08 ns for ATTO 647N on Graphene (bottom) – hBN (top) (🟥), and 1,61 ± 0.14 ns for Graphene (bottom) – bilayer hBN (top) (🟧).

It is important to note that all comments and conclusions discussed above are based solely on the fluorescence response of the dye molecules. Other potential effects of hBN on graphene upon heterostructure formation have been neglected in this analysis. To mention only a few, hexagonal boron nitride (hBN) significantly enhances graphene's electronic properties, particularly its carrier mobility, by minimizing interactions with charge traps, surface roughness, and phonon scattering, thus facilitating more unrestricted electron movement [164], [223], [224], [225]. This improvement makes hBN/graphene heterostructures ideal for high-performance electronic and quantum devices. Additionally, the interaction between graphene and hBN can induce a small band gap in graphene, which is crucial for its application in semiconductor technologies [226]. When graphene is rotationally aligned with hBN [227], the resulting Moiré pattern modulates its electronic band structure, leading to phenomena such as minibands and secondary Dirac points, which are essential for studying new quantum phases. Moreover, the excellent thermal conductivity of hBN enhances heat dissipation, benefiting high-frequency and optoelectronic devices where efficient thermal management is critical [162].

Nevertheless, this study focuses on applying these platforms in systems with fluorescent readouts. As such, the only parameter investigated is GET and its possible changes in the presence of hBN. While noteworthy, the electronic and quantum properties of hBN/graphene heterostructures fall outside the scope of this particular analysis.

Initially, hBN was introduced to enhance the overall quality of graphene in our platforms. While it did not drastically alter graphene's intrinsic properties, we discovered that the monolayer of hBN provided valuable benefits as an ultra-thin spacer. Specifically, hBN improved the flatness of the graphene surface by reducing corrugations and suppressing charge inhomogeneities caused by underlying substrates, thereby minimizing electronic disorder. Additionally, its dielectric nature helped to reduce substrate-induced fluorescence quenching and preserved the photophysical properties of dye molecules immobilized on the surface. These attributes make hBN a valuable component for stabilizing graphene and optimizing its performance in optoelectronic and biosensing applications. Simultaneously, we demonstrate its potential as a platform on which complex biomolecular structures, such as DNA origami nanostructures, can be immobilized. This finding opened up new possibilities for its application in fluorescence-based studies. Building on this, our interest in the versatility of hBN extended beyond its role in graphene quality improvement. We also sought to investigate whether simpler DNA configurations, such as our newly designed hybrid DNA, could be applied to systems incorporating hBN.

Various configurations and lengths of the hybrid DNA constructs have been described previously [92]. In this study, we utilized nanostructures comprising a 51mer single-stranded DNA (ssDNA) labeled with a dye molecule at the 51st base pair (approximately 17.5 nm) and hybridized to unlabeled 136mer complementary strands (S0) (Figure 11.14). This distance was selected as it falls within the most sensitive range for detecting dye-graphene distance variations, similar to the DNA origami nanostructures explored in previous studies. By setting the dye at this position, even minor variations in its photophysical properties due to the interactions with graphene could be detected, facilitating a comprehensive investigation of the system.

From this point forward, the investigated hybrid DNA will be referred to as '51bp dsDNA.' The following experiments were conducted analogously to the studies performed with DNA origami nanostructures. Specifically, three types of samples were examined at the single-molecule level using a fluorescence confocal microscope. These three samples consisted of 51bp dsDNA immobilized: on graphene, on graphene deposited on hBN, and on hBN deposited on graphene. The desired solution containing hybrid DNA was incubated for 1 minute. Following incubation, the chamber was thoroughly rinsed with 1× TAE buffer + Mg to remove any unbound material and fix the proper concentration of the sample.

The results of these experiments are presented in Figure 11.14, demonstrating a significant advancement in integrating DNA nanostructures with two-dimensional materials. Our findings align with those obtained from DNA origami nanostructures, confirming that hexagonal boron nitride (hBN) serves effectively as an ultra-thin spacer between dye molecules and the graphene surface.

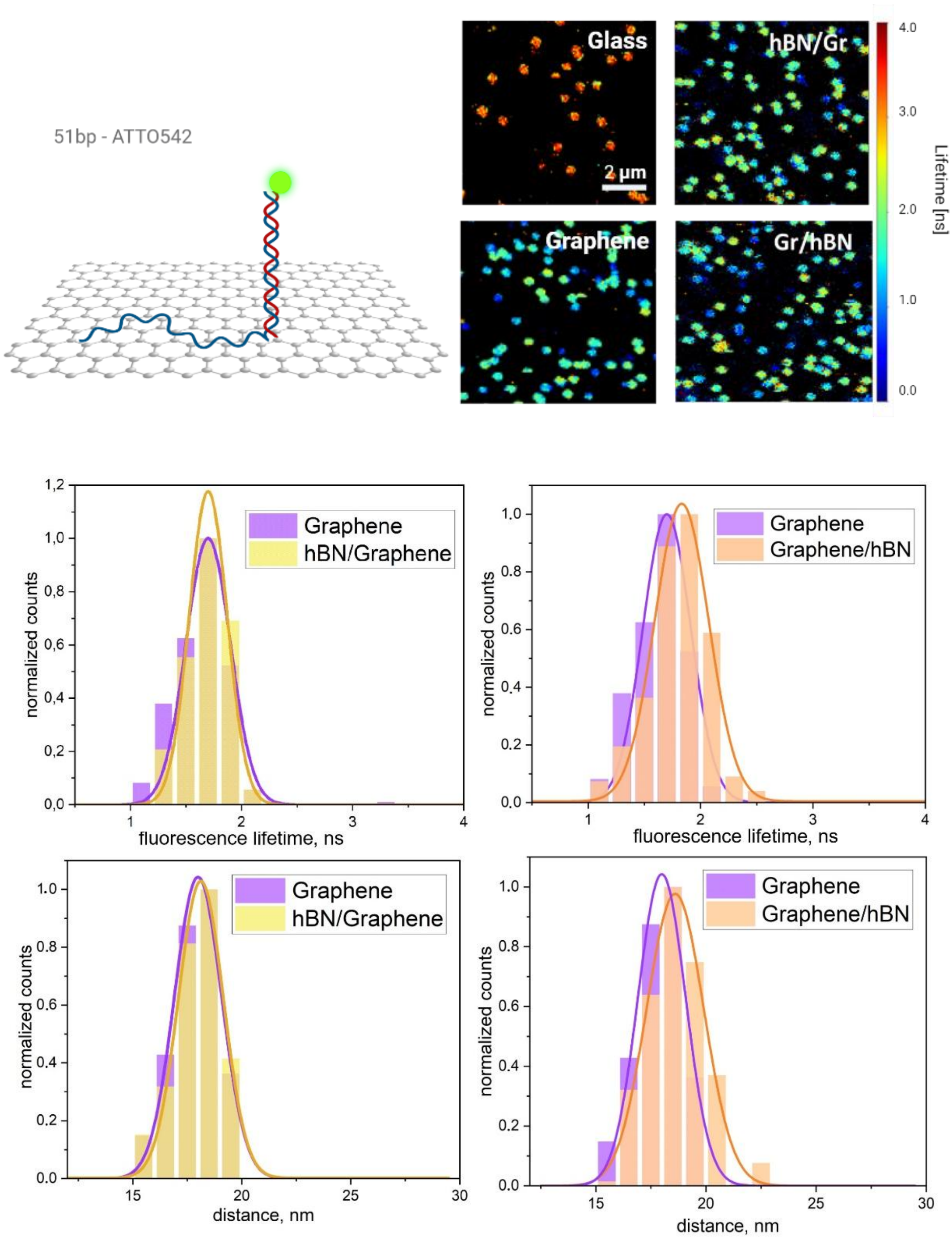

Figure 11.14 Measurements of the fluorescence lifetime of ATTO 542 dye molecules in 51bp DNA immobilized on two types of heterostructures consisting of graphene and hBN in which graphene was either a top (hBN/Graphene) or a bottom layer (Graphene/hBN). The results are compared with analogical measurements on graphene. (a) Schematic representation of 51bp DNA functionalized with ATTO 542 (b) Exemplary fluorescence intensity maps, (c) Histograms fitted with a Gaussian function of the fluorescence lifetime. The mean fluorescence lifetime of ATTO 542 on graphene (🟪) equals 1.68 ± 0.09 ns, 1,70 ± 0.11ns for ATTO 647N on hBN/Graphene (🟧), and 1.83 ± 0.13 ns for Graphene/hBN (🟨). d) Histograms fitted with a Gaussian function of the distance between graphene and ATTO 542. The mean distance on graphene (🟪) equals 18.06 ± 0.18nm, 18.12± 0.07 nm for ATTO 647N on hBN/Graphene (🟧), and 18,57 ± 0.12 nm for Graphene/hBN (🟨).

Notably, our study is the first to successfully immobilize hybrid DNA structures perpendicularly on hBN and graphene/hBN heterostructures. This perpendicular orientation is a substantial breakthrough, as previous research primarily focused on parallel alignments of double-stranded DNA (dsDNA) on graphene [82], [228], [229]. The perpendicular arrangement facilitates more efficient interactions and functionalization, enhancing the potential of these nanostructures in various applications [230], [231].

The stability and structural integrity of the hybrid DNA on hBN were meticulously assessed, with results indicating that hBN provides a robust platform for such assemblies. This stability is crucial for the development of reliable nanoscale devices and sensors. Our observations validate the applicability of hybrid DNA in systems incorporating hBN, thereby broadening the potential scope of hBN-based nanostructures in fluorescence-based studies and beyond.

In light of recent findings on the diffusion of DNA on atomically flat 2D materials, such as hBN [232], it is noteworthy that no evidence of DNA diffusion was observed during our experiments. The fluorescence lifetime measurements from 10x10 µm maps, which lasted several minutes, revealed no noticeable diffusion effects or positional shifts when the same map was re-registered in the exact location. This suggests that the DNA remained immobilized within the timescale of our measurements.

This pioneering work opens new avenues for designing advanced nanodevices, particularly in biosensing and molecular electronics, where DNA molecules' precise orientation and stability are paramount. The integration of hBN as a spacer not only enhances the functional properties of the hybrid structures but also offers a versatile platform for future explorations in nanotechnology.

Summary and Outlook

This work presents the advancements in the development and application of graphene-based platforms for fluorescence-based assays and nanoscale studies. By investigating graphene energy transfer (GET) efficiency across monolayer, bilayer, and trilayer graphene substrates, the study has validated the d^{-4} distance scaling law for GET alongside the characteristic distance d_0 for 50% energy transfer efficiency. These findings were achieved through precise measurements using DNA origami nanostructures labeled with dye molecules positioned at varying distances from the graphene surface. The findings demonstrate that fluorescence quenching efficiency increases progressively with each additional graphene layer, extending the dynamic working range of GET. A theoretical model was also validated, closely aligning with experimental data and providing insights into tuning of GET for fluorescence-based applications.

A dynamic assay utilizing bilayer graphene substrates was introduced, demonstrating enhanced GET resolution capable of detecting binding events at distances beyond the operational range of monolayer graphene. This extended resolution underscores the potential of bilayer graphene for achieving higher precision in dynamic fluorescence assays at larger distances. Collectively, these findings highlight the potential of tuning graphene layers for biosensing and super-resolution microscopy.

In parallel, the integration of graphene with hexagonal boron nitride (hBN) to create robust heterostructures has been achieved. Challenges in hBN transfer were addressed using optimized wet transfer techniques, enabling the reliable preparation of constructs in two configurations: graphene on hBN and hBN on graphene. These heterostructures exhibited excellent structural integrity and reproducibility, as confirmed by scanning electron microscopy. Fluorescence lifetime measurements revealed hBN’s role as an ultra-thin spacer, preserving the photophysical properties of dye-labeled molecules while maintaining their structural stability. It was shown that hBN does not impact graphene’s energy transfer properties, highlighting its complementary nature in nanoscale precision studies.

Furthermore, the interaction of these heterostructures with biomolecules was explored, successfully demonstrating the immobilization of DNA origami nanostructures and dsDNA constructs. Notably, hBN enabled the perpendicular alignment of dsDNA structures, marking a significant advancement over prior studies focused on parallel alignments. This orientation facilitates more efficient interactions and functionalization, broadening the potential applications of these nanostructures in biosensing and optoelectronics.

The findings of this study have established hBN-graphene heterostructures as versatile platforms for fluorescence-based assays and advanced nanoscale applications. The stability, tunability, and reproducibility of these constructs present a robust foundation for further innovations in nanotechnology, materials science, and molecular biology.

Building on these achievements, several exciting directions for future research are proposed:

- **Dynamic Molecular Studies**: The operational range of bilayer and trilayer graphene could be further exploited to monitor dynamic molecular interactions and conformational changes with high temporal and spatial precision.
- **Expanded Configurations**: Novel configurations, such as hybrid or multilayered hBN structures, could be investigated to optimize fluorescence quenching efficiency and energy transfer properties. Variations in the number of hBN layers and graphene arrangements may offer enhanced control over fluorescence responses.
- **Multi-Modal Platforms**: The integration of hBN-graphene heterostructures with electronic, optical, or mechanical sensing modalities could enable the development of versatile multi-modal platforms for detecting diverse biomolecular interactions.
- **High-Throughput Systems**: Incorporating these constructs into lab-on-a-chip or microfluidic devices could facilitate real-time, high-throughput analysis of molecular interactions and enable diagnostics and molecular biology applications.
- **Broader Biomolecular Studies**: The universality and adaptability of hBN-based systems could be tested with a wider range of biomolecules, including

proteins, nucleic acids, and synthetic nanostructures, expanding their applicability to new domains.

- **Quantum and Optoelectronic Applications**: The unique electronic and thermal properties of hBN and graphene could be leveraged in quantum sensing and optoelectronic devices, offering breakthroughs in spatial and temporal resolution.

The findings presented in the thesis open up promising avenues for enhancing the precision and reliability of fluorescence-based experiments. Future studies are expected to refine these approaches further, unlocking the full potential of hBN-graphene platforms in nanoscale research and technology.

Appendix

Table 3 Fundamental staples in constructing the pillar-shaped DNA origami structure, sequenced from the 5’ end to the 3’ end.

Staple ID	Sequence (5’ to 3’)
P1	GAGAAGGCATCTGCAATGGGATAGGTCAAAAC
P2	AACCGTGTCATTGCAACGGTAATATATTTTAAATGAAAGGGT
P3	ATCGGTCAGATGATATTCACAAACCAAAAGA
P4	GCTGGCATAGCCACATTATTC
P5	CTGTATGGGATTACCGTTAGTATCA
P6	CCATAATGCCAGGCTATCAAGGCCGGAGACATCTA
P7	CTCATCGGGATTGAGTGAGCGAGTAACAACCCGTC
P8	TAGCCAGCTTTCATCCAAAAATAAACGT
P9	TAGCCTCAGAGCATACCCTGT
P10	AATACCCCAACATTCATCAAAAATAATTCGCGTCT
P11	GGCTAAAACTTCAGAAAAGTTTTGCGGGAGATAGAACC
P12	CCCGGTTGATAAAGCATGTCAATC
P13	ATCGATGCTGAGAGTCTACAAGGAGAGGGAACGCCAAAAGGA
P14	GACAATTACGCAGAGGCATTTTCGAG
P15	TAAGTTGGCATGATTAAAGAA
P16	CCAATGTTTAAGTACGGTGTCCAAC
P17	CGGAATAGAAAGGAATGCCTTGCTAAACAACTTTCAAC
P18	GAGTTAAAAGGGTAATTGAGCGCTAATATCAGAGGAACTGAACACC
P19	TTTAGCGATACCAACGCGTTA
P20	TTTTTGCGGATGCTCCTAAAATGTTTAGATGAATTTTGCAAAAGAAGTT
P21	AATAAAACGAACTATGACCCCACCAAGC
P22	AATATCGTTAAGAGAGCAAAGCGGATTGTGAAAAATCAGGTCTTT
P23	ATTACGAGATAAATGCCAGCTTTGAGGGGACGACGACAG
P24	ACAACGCCTGTAGCATTTACCGTATAGGAAG
P25	TTACCATTAGCAAGGCCTTGAATTAGAGCCAGCCCGACTTGAGC
P26	CAGCAGCGCCGCTTGTTTATCAGCTTCACGAAAAA
P27	CTTACGGAACAGTCAGGACGTTGGGAAGAAA
P28	AGCTCTTACCGAAGCCCAATA
P29	TATTACGAATAATAAACAAATCAGATATGCGT
P30	CACGGCAACAATCCTGATATACTT

Staple ID	Sequence (5’ to 3’)
P31	CATCGAGATAACGTCAAACATAAAAGAGCAAAAGAATT
P32	CAAGCCCAATAGGAACCACCCTCACCCGGAA
P33	CATTTCGCAAATGTCATCTGCGAACGAGAGATTCACAATGCC
P34	GGCGCAGACGGTCAATCATCGAGACCTGCTCCATGTGGT
P35	CAAACGGAATAGGAAACCGAGGAATAAGAAATTACAAG
P36	ACCAACAAACCAAAATTAACAATTTCATTTGAATTACCGAGG
P37	CATTTGAGATAACCCACGAAACAATG
P38	AGGACAGATGAACGGTGTAACATAAGGGAACCGAAGAAT
P39	TGGCTTTTTACCGTAGAATGGAAAGCG
P40	GTTAAAGGAAAGACAGCATCTGCCTATTTAAGAGGCAGGAGGTTTA
P41	AGTAGGTATATGCGTTATACA
P42	CGAACACCAAATAAAATAGCAGCCAAGTTTGCCTTTAGCGTCAGA
P43	GCGAAACAAAGTGTAAAACACATGGCCTCGATTGAACCA
P44	AAGAAAGCTTGATACCGCCACGCATACAGACCAGGCGCTGAC
P45	CTGAATATAGAACCAAATTATTTGCACGTAAAACAACGT
P46	AGACAGCAGAAACGAAAGAGGAAATAAATCGAGGTGACAGTTAAAT
P47	CGAGGGTACTTTTTCATGAACGGGGTCATAATGCCGAGCCACCACC
P48	TAAAGCCTCCAGTACCTCATAGTTAGCG
P49	AATATGCAACTACCATCATAGACCGGAACCGC
P50	AGAAATCGTTAGACTACCTTTTTAAGGCGTTCTGACCTTTTTGCA
P51	CTAAATCGGTCAGAATTAGCAAAATTAAGCAATAAAATAATA
P52	AAATCAGCTCATTTTTTAACCATTTTGTTAAAATTCGCATTA
P53	ATAGCGAGAGGCTATCATAACCAAATCCCAAAGAAAATTTCATCCTCAT
P54	GAACTGGCTCATTACAACTTTAATCATTCTTGAGATTACTTA
P55	ACGCGAGAGAAGGCCATGTAATTTAGGCCAGGCTTAATTGAGAATCGC
P56	TAATATCAAAGGCACCGCTTCTGGCACT
P57	TTTCCATGGCACCAACCTACGTCATACA
P58	AAGACAAATCAGCTGCTCATTCAGTCTGACCA
P59	CCGTAATCAGTAGCGACAGAATCTAATTATTCATTAAAAAGG
P60	CTGGCATTAGGAGAATAAAATGAAGAAACGATTTTTTGAGTA
P61	CGCGCCGCCACCAGAACAGAGCCATAAAGGTGGAA
P62	TAGCCCGGAATAGGTGTAAGGATAAGTGCCGTCGA
P63	AAGGCTCCAAAAGGAGCCTTTATATTTTTTCACGTGCTACAGTCACCCT

Staple ID	Sequence (5’ to 3’)
P64	CAAAATCACCGGAACCAGAGCCAGATTTTGTCACAATCACAC
P65	AATTGTGTCGAAATCCGCGGCACACAACGGAGATTTGTATCA
P66	CCTCGTCTTTCCACCACCGGAACCGCCTCCCTCA
P67	CCGTGTGATAAATAACCTCCGGCTGATG
P68	CCCAGCTACAATGACAGCATTTGAGGCAAGTTGAGAAATGAA
P69	TATTTAAATTGCAGGAAGATTG
P70	AAGGGATATTCATTACCGTAATCTATAGGCT
P71	ACCAGACCGGATTAATTCGAGC
P72	AAGGCCTGTTTAGTATCATGTTAGCTACCTC
P73	AGCAACAAAGTCAGAAATAATATCCAATAATCGGCTCAGGGA
P74	TGAGTAAAGGATAAGTTTAGCTATATCATAGACCATTAGATA
P75	GAGTCTGGATTTGTTATAATTACTACATACACCAC
P76	TTCGGTCCCATCGCATAGTTGCGCCGACATGCTTTCGAGGTG
P77	CGTGTCAAATCACCATCTAGGTAATAGATTT
P78	GGAACCATACAGGCAAGGCAAATCAAAAAGACGTAGTAGCAT
P79	ATTTGGAAGTTTCATGCCTCAACATGTTTTA
P80	AATTTCTTAAACCCGCTTAATTGTATCGTTGCGGGCGATATA
P81	GAGCATTTATCCTGAATCAAACGTGACTCCT
P82	TTATAAGGGTATGGAATAATTCATCAATATA
P83	TAACGACATTTTTACCAGCGCCAAAGAAAGTTACCAGAACCCAAA
P84	AAAGATTACAGAACGGGAGAAGGAAACGTCACCAATGAAACCA
P85	GCTGTAGTTAGAGCTTAATTG
P86	AGTTTCCAACATTATTACATTATAC
P87	GGGATATTGACGTAGCAATAGCTAAGATAGC
P88	AACAAGAGCCTAATGCAGAACGCGC
P89	AGTTTATTGTCCATATAACAGTTGATTC
P90	TATTGAAAGGAATTGAGGTAG
P91	AATAGAAAAAAATAAACGTCTGAGAGGAATATAAGAGCAACACTATGAT
P92	TCGTGCCGGAGTCAATAGTGAATTTGCAGAT
P93	TTAGTTTGAGTGCCCGAGAAATAAAGAAATTGCGTAGAGATA
P94	TTGGTAGAACATTTAATTAAGCAAC
P95	TAACATCCAATAAATGCAAAGGTGGCATCAACATTATGAAAG
P96	TAAGTTTACACTGAGTTTCGT

Staple ID	Sequence (5’ to 3’)
P97	AGAACTTAGCCTAATTATCCCAAGCCCCCTTATTAGCGTTTGCCA
P98	ACCGCCACCCTCAGAACCCGTACTCTAGGGA
P99	TTAGCCCTGACGAGAAACACCAGAAATTGGGGTGAATTATTTTAA
P100	ATAAAGTCTTTCCTTATCACT
P101	ATTTCCTGATTATCAGATGATGGCTTTAAAAAGACGCTAAAA
P102	ACATAAGTAGAAAAATCAAGAAGCAAAAGAAGATGTCAT
P103	TTCATCGGCATTTTCGGTCATATCAAAA
P104	GAACCGCCACCCTCCATATCATACC
P105	ACTAATGCCACTACGAATAAA
P106	CAAGCCGCCCAATAGCAAGTAAACAGCCATATTATTTTGCCATAAC
P107	TGAAAATCCGGTCAATAACCTAAATTTTAGCCTTT
P108	CCTCGTTTACCAGAAACCAAA
P109	CAAATTATTCATTTCAATTACCTGAGTA
P110	ATTTCAACCAAAAATTCTACTAATAGTTAGTTTCATTTGGGGCGCGAGC
P111	AGGCTTGCGAGACTCCTCAAGAGAAAAGTATTCGGAAC
P112	AATATTCATTGAATCCATGCTGGATAGCGTCCAAT
P113	CTAGTCAGTTGGCAAATCAACAGTCTTTAGGTAGATAACAAA
P114	TATGACTTTATACATTTTTTTTTAATGGAAACAGTACACCGT
P115	ACTAAAGAGCAACGTGAAAATCTCCACCCACAACTAAAGGAA
P116	TTGCGAATAATATTTACAGCGGAGTGAGGTAAAATTTTGAGG
P117	CCGACTTGTTGCTAAAATTTATTTAGTTCGCGAGAGTCGTCTTTCCAGA
P118	ATTGTTATCTGAGAAGAAACCAGGCAAAGCGCCATTCGTAGA
P119	AGTACCGCATTCCACAACATGTTCAGCCTTAAGGTAAAGTAATTC
P120	AAACTCACAGGAACGGTACGCCAGTAAAGGGGGTGAGGAACC
P121	CGCTTTCCAGTTAGCTGTTTAAAGAACGT
P122	GGCGAAGCACCGTAATAACGCCAGGGTTTTCCCAGTCATGGG
P123	TTTACCAGTCCCGGCCTGCAGCCCACTACGGGCGCACCAGCT
P124	GGCAACACCAGGGTCTAATGAGTGAGCTCACAACAATAGGGT
P125	GAAGGAGCGGAATTATCATCATATATCATTTACATAGCACAA
P126	CGCGCTACAGAGTAATAAAAGGGACATTCTGATAGAACTTAG
P127	GTAATTAATTTAGAATCTGGGAAGGGCGATCGGTGCGGCAAA
P128	GGATGTGGTTTGCCCCAGCAG
P129	GCCAGCAGTTGGGCGCAAATCAGGTTTCTTGCCCTGCGTGGT

Staple ID	**Sequence (5’ to 3’)**
P130	TATCAGCAACCGCAAGAATGCCAATGAGCCTGAGGATCTATC
P131	GAGAACAATATACAAAATCGCGCAGAGGCGATTCGACAAATCCTTTAAC
P132	GTAAAACGACGGCCCATCACCCAAATCAGCGC
P133	ACGGGCCGATAATCCTGAGAAGTGTTTTTATGGAGCTAACCG
P134	TGCTAAATCGGGGAGCCCCCGATTTAGAGCTAGCAGAACATT
P135	ACGCGGTCCGTTTTTGGGTAAGTGA
P136	GCGTCCACTATTCCTGTGTGAAATGCTCACTGCC
P137	CGTACTATGGTAACCACTAGTCTTTAATGCGCGAACTGAATC
P138	AGAATTTTAGAGGAAAACAATATTACCGCCAGCTGCTCATTT
P139	TTGGGCGGCTGATTTCGGCAAAATCCCT
P140	TGGTGGTTGTTCCAGTTTGGAACA
P141	AGTCGCCTGATACTTGCATAACAGAATACGTGGCACAGCTGA
P142	TGCTGATTGCCGTTGTCATAAACATCGGGCGG
P143	TGAGTGTTCCGAAAGCCCTTCACCGCCTAGGCGGTATTA
P144	TGAGCAAATTTATACAGGAATAACATCACTTGCCTGAGTCTT
P145	CCTGCGCTGGGTGGCGAGAAAGGAAGGGAAGGAGCGGGGCCG
P146	CGTACAGGCCCCCTAACCGTCCCCGGGTACCGAGCGTTC
P147	TTTAGATTCACCAGTCACACGACCGGCGCGTGCTTTCCCAGA
P148	CCCCGCTAGGGCAACAGCTGGCGAAAGGGGGATGTGCTTATT
P149	TCACAGCGTACTCCGTGGTGAAGGGATAGCTAAGAGACGAGG
P150	TGCGTGTTCAGGTTGTGTACATCG
P151	AGGGAGCCGCCACGGGAACGGATAGGCGAAAGCATCAGCACTCTG
P152	AAGAAAGCGCTGAACCTCAAATATTCTAAAGGAAAGCGTTCA
P153	AGCGCAGCTCCAACCGTAATCATGGTCACGGGAAACCT
P154	CCTCATCACCCCAGCAGGCCTCTTCGCTATTACGCCAGTGCC
P155	GTCGCGTGCCTTCGAATTGTCAAAG
P156	TTCGGGGTTTCTGCCAGGCCTGTGACGATCC
P157	AGAGAAAATCCAGAGAGTTGCAGCAAATC
P158	TGCCATCCCACGCAGGCAGTTCCTCATTGCCGTTTTAAACGA
P159	GCCCGAGTACGAGCCGGAAGC
P160	GAGGCCAAGCTTTGAATACCAAGTACGGATTACCTTTTCAAA
P161	ACGTAAGAATTCGTTCTTAGAAGAACTCAAACTATCGGATAA
P162	TAAAACCGTTAAAGAGTCTGTCCATCCAGAAACCACACAATC

Staple ID	Sequence (5’ to 3’)
P163	ACGAGCGGCGCGGTCAGGCAAGGCGATTAAGTTGGGTAAAAC
P164	TTTTCCAGCATCAGCGGGGCTAAAGAACCTCGTAGCACGCCA
P165	CAAAGCACTAGATAGCTCCATTCAGGCTGCGCAACTGTCTTG
P166	ATTGCGTTGCTGTTATCCGCTCACAATTCCAAACTCACTTGCGTA
P167	GAGAGATAGACTTTACGGCATCAGA
P168	TGACCGCGCCTTAATTTACAATATTTTTGAATGGCTATCACA
P169	CCTAATTTAACAAACCCTCAATCAATATCTGATTCGCTAATC
P170	TTAACTCGGAATTAGAGTAAATCAATATATGTGAGTGATTCT
P171	ATGAAGGGTAAAGTTCACGGTGCGGCCATGCCGGTCGCCATG
P172	ACATAAAGCCCTTACACTGGTCGGGTTAAATTTGT
P173	AAATGCGGAAACATCGGTTTTCAGGTTTAACGTCAGATTAAC
P174	GTCGCAGAAAAACTTAAATTTGCC
P175	GAATTCGTCTCGTCGCTGGGTCTGCAATCCATTGCAACACGG
P176	GCGAAAATCCCGTAAAAAAAGCCGTGGTGCTCATACCGGCGTCCG
P177	CTTGTAGAACGTCAGCGGCTGATTGCAGAGTTTTTCGACGTT
P178	TCATACATTTAATACCGATAGCCCTAAAACATCGAACGTAAC
P179	TACGGCTGGAGGTGCGCACTCGTCACTGTTTGCTCCCGGCAA
P180	AAATGACGCTAAATGGATTATTTACATTGGCGAATACCTGGA
P181	AACAACAGGAAGCACGTCCTTGCTGGTAATATCCAGAAACGC
P182	TGCATTAATGAGCGGTCCACGCTCACTGCGCCACGTGCCAGC
P183	ACCTGACGGGGAAAGCCGGCGAACCAAGTGTCTGCGCGTTGC
P184	CCAGCCTCCGATCCTCATGCCGGA
P185	GCTGGTCTGGTCAGGAGCCGGAATCCGCCGTGAACAGTGCCA
P186	GCGAATCAGTGAGGCCACCGAGTAGTAGCAACTGAGAGTTGA
P187	GGCCAACGCGCGGGGAGGGCCCTGTGTTTGA
P188	AGCTTTCAGAGGTGGCGATGGCCAGCGGGAAT
P189	ATTAGCGGGGTTTTGCTCAGTACCAGGCTGACAACAAGCTG
P190	TGCCCGTATAAACAGTGTGCCTTCTGGTAA
P191	AGAAAACGAGAATGACCATAAATCTACGCCCCTCAAATGCTTTA
P192	ATAACTATATGTAAATGCTTAGGATATAAT
P193	AGGAATCATTACCGCGTTTTTATAAGTACC
P194	GATTAGAGAGTACCTTAACTCCAACAGG
P195	CCTTAAATCAAGATTAGCGGGAGGCTCAAC

Staple ID	Sequence (5’ to 3’)
P196	GCATGTAGAAACCAATCCATCCTAGTCCTG

Table 4 Biotin-modified staples from the 5' to the 3' ends employed in constructing the pillar-shaped DNA origami nanostructure.

Sequence (5’ to 3’)	Function	Replace
Biotin- AGAAAACGAGAATGACCATAAATCTACGCCCCTCAAATGCTTTA	Immobilization on glass	P189
Biotin- ATTAGCGGGGTTTTGCTCAGTACCAGGCTGACAACAAGCTG	Immobilization on glass	P190
Biotin- GCATGTAGAAACCAATCCATCCTAGTCCTG	Immobilization on glass	P191
Biotin-GATTAGAGAGTACCTTAACTCCAACAGG	Immobilization on glass	P192
Biotin- TGCCCGTATAAACAGTGTGCCTTCTGGTAA	Immobilization on glass	P193
Biotin- CCTTAAATCAAGATTAGCGGGAGGCTCAAC	Immobilization on glass	P194
Biotin- AGGAATCATTACCGCGTTTTTATAAGTACC	Immobilization on glass	P195
Biotin-ATAACTATATGTAAATGCTTAGGATATAAT	Immobilization on glass	P196

Table 5 Staples for the pillar-shaped DNA origami nanostructure with extensions for immobilization on graphene from the 5’ to the 3’ end.

Sequence (5’ to 3’)	Function	Replace
ATATTTCCTCTACCACCTACATCACTAATTAGCGGGGTTTTGCTCAGTACCAGGCTGACAACAAGCTG	Immobilization on graphene	P189
ATATTTCCTCTACCACCTACATCACTAAGAAAACGAGAATGACCATAAATCTACGCCCCTCAAATGCTTTA	Immobilization on graphene	P190
ATATTTCCTCTACCACCTACATCACTAATAACTATATGTAAATGCTTAGGATATAAT	Immobilization on graphene	P191
ATATTTCCTCTACCACCTACATCACTAGCATGTAGAAACCAATCCATCCTAGTCCTG	Immobilization on graphene	P192

Sequence (5’ to 3’)	Function	Replace
ATATTTCCTCTACCACCTACATCACTATGCCCGTATAAACAGTGTGCCTTCTGGTAA	Immobilization on graphene	P193
ATATTTCCTCTACCACCTACATCACTAAGGAATCATTACCGCGTTTTTATAAGTACC	Immobilization on graphene	P194
ATATTTCCTCTACCACCTACATCACTAGATTAGAGAGTACCTTAACTCCAACAGG	Immobilization on graphene	P195
ATATTTCCTCTACCACCTACATCACTACCTTAAATCAAGATTAGCGGGAGGCTCAAC	Immobilization on graphene	P196

Table 6 Staples from the 5’ to the 3’ end for the pillar-shaped DNA origami structure for distance determination and distance scaling law for mono- and multilayer graphene.

Sequence (5’ to 3’)	Function	Replace
AGACAGCAGAAACGAAAGAGGAAATAAATCGAGGTGACAGTTAAAT-**ATTO 542**	Dye ATTO 542 at 3’ (12 nm)	P46
AATATGCAACTACCATCATAGACCGGAACCGC- **ATTO 542**	Dye ATTO 542 at 3’ (16 nm)	P49
AATATGCAACTACCATCATAGACCGGAACCGC- **ATTO 647N**	Dye ATTO 647N at 3’ (16 nm)	P49
AAGGGATATTCATTACCGTAATCTATAGGCT- **ATTO 542**	Dye ATTO 542 at 3’ (24 nm)	P70
AAGGGATATTCATTACCGTAATCTATAGGCT-**ATTO 647N**	Dye ATTO 647N at 3’ (24 nm)	P70
ATTGTTATCTGAGAAGAAACCAGGCAAAGCGCCATTCGTAGA-**ATTO 542**	Dye ATTO 542 at 3’ (30 nm)	P118
ATTGTTATCTGAGAAGAAACCAGGCAAAGCGCCATTCGTAGA-**ATTO 647N**	Dye ATTO 647N at 3’ (30 nm)	P118
TAAAACCGTTAAAGAGTCTGTCCATCCAGAAACCACACAATC-**ATTO 542**	Dye ATTO 542 at 3’ (40 nm)	P162
TAAAACCGTTAAAGAGTCTGTCCATCCAGAAACCACACAATC-**ATTO 647N**	Dye ATTO 647N at 3’ (40 nm)	P162
ACGGGCCGATAATCCTGAGAAGTGTTTTTATGGAGCTAACCG- **ATTO 542**	Dye ATTO 542 at 3’ (53 nm)	P133
ACGGGCCGATAATCCTGAGAAGTGTTTTTATGGAGCTAACCG-**ATTO 647N**	Dye ATTO 647N at 3’ (53 nm)	P133

Table 7 Staples from the 5’ to the 3’ end for the pillar-shaped DNA origami structure used to study dynamic assays for monolayer and bilayer GET.

Sequence (5’ to 3’)	Function	Replace
Cy3B-**ATTTACG**GGCTTTTTTTTTTTTTATTGAAAGGAATTGAGGTAG	Pointer P28 at 5’	P90
CGTAAATTTTGATACATAAGTAGAAAAATCAAGAAGCAAAAGAAGATGTCAT	Low binding strand for P28	P102
CGTAAATTTTCTAGTCAGTTGGCAAATCAACAGTCTTTAGGTAGATAACAAA	High binding strand for P28	P113
Cy3B-**ATTTACG**GGCTTTTTTTTTTTTCTAGTCAGTTGGCAAATCAACAGTCTTTAGGTAGATAACAAA	Pointer P35 at 5’	P113
CGTAAATTTTTATTGAAAGGAATTGAGGTAG	Low binding strand for P35	P90
CGTAAATTTTTAACAAACCCTCAATCAATATCTGATTCGCTAATC	High binding strand for P35	P169
TAAAACCGTTAAAGAGTCTGTCCATCCAGAAACCACACAATCCCTAATT	Exchange staple	P162
AATATGCAACTACCATCATAGACCGGAACCGC-**ATTO 647N**	Reference dye ATTO 647N at 3’ (16 nm)	P49

References

[1] K. S. Novoselov, A.K. Geim, S.V. Morozov, D.E. Jiang, Y. Zhang, S.V. Dubonos, I.V. Grigorieva, and A.A. Firsov, “Electric Field Effect in Atomically Thin Carbon Films Science,” Science, vol. 306, no. 5696, pp. 666-669, 2004.

[2] A. K. Geim and K. S. Novoselov, “The rise of graphene,” Nat Mater, vol. 6, no. 3, pp. 183-191, 2007.

[3] I. Kamińska, J. Bohlen, R. Yaadav, P. Schüler, M. Raab, T. Schröder, J. Zähringer, K. Zielonka, S. Krause, and P. Tinnefeld, “Graphene Energy Transfer for Single-Molecule Biophysics, Biosensing, and Super-Resolution Microscopy,” Advanced Materials, vol. 33, no. 21, 2101099, 2021.

[4] S. Krause, E. Ploetz, I. Bohlen, P. Schuler, R. Yaadav, F. Selbach, I. Kamińska, P. Tinnefeld, “Graphene-on-Glass Preparation and Cleaning Methods Characterized by Single-Molecule DNA Origami Fluorescent Probes and Raman Spectroscopy,” ACS Nano, vol. 15, no. 4, pp. 6430-6438, 2021.

[5] A. Ghosh, A. Sharma, A.I. Chizhik, S. Isbaner, D. Ruhlandt, R. Tsukanov, I. Gregor, N. Karedla, and J. Enderlein, “Graphene-based metal-induced energy transfer for sub-nanometre optical localization,” vol. 13, no. 12, pp. 860-865, 2019.

[6] I. Kaminska, J. Bohlen, S. Rocchetti, F. Selbach, G. P. Acuna, and P. Tinnefeld, “Distance Dependence of Single-Molecule Energy Transfer to Graphene Measured with DNA Origami Nanopositioners,” Nano Lett, vol. 19, no. 7, pp. 4257-4262, 2019.

[7] Z. Chen, S. Berciaud, C. Nuckolls, T. F. Heinz, and L. E. Brus, “Energy transfer from individual semiconductor nanocrystals to graphene,” ACS Nano, vol. 4, no. 5, pp. 2964-29682010, 2010.

[8] A. Raja, A. Montoya− Castillo, J. Zultak, J, X.X Zhang, Z. Ye, C. Roquelet, D.A> Chenet, A.M. van der Zande, P. Huang, S. Jackusch, J. Hone, D.R. Reichnman, L.E. Brus, and T.F. Heinz, “Energy Transfer from Quantum Dots to Graphene and MoS2: The Role of Absorption and Screening in Two-Dimensional Materials,” Nano Lett, vol. 16, no. 4, pp. 2328-2333, 2016.

[9] R. N. Day, “Measuring protein interactions using Förster resonance energy transfer and fluorescence lifetime imaging microscopy,” Methods, vol. 66, no. 2, pp. 200-207, 2014.

[10] C. Bücherl, J. Aker, S. de Vries, and J. W. Borst, “Probing protein-protein Interactions with FRET-FLIM.,” Methods Mol Biol, vol. 655, pp. 389-399, 2010.

[11] Y. Qiao, Y. Luo, N. Long, Y. Xing, and J. Tu, “Single-molecular Förster resonance energy transfer measurement on structures and interactions of biomolecules,” Micromachines, vol. 12, no. 5, pp. 492, 2021.

[12] J. Phiri, P. Gane, and T. C. Maloney, “General overview of graphene: Production, properties and application in polymer composites,” Mat Sci Eng: B, vol. 215, pp. 9-28, 2017.

[13] B. Dziejarski, J. Serafin, K. Andersson, and R. Krzyżyńska, “CO2 capture materials: a review of current trends and future challenges,” Mater Today Sustain, vol. 100483, 2023.

[14] E. Abbasi, A. Akbarzadeh, M. Kouhi, and M. Milani, “Graphene: Synthesis, bio-applications, and properties,” vol. 44, no. 1, pp. 150-156, 2016.

[15] A. C. Ferrari, F. Bonaccorso, V. Fal'Ko, K.S. Novoselov, S. Roche, P. Bøggild, S. Borini, F.H.L. Koppens, V. Palermo, N. Pugno, J.A. Garrido, R. Sordan, A. Bianco, L. Ballerini, M. Prato, E. Lidorikis, J. Kivioja, C. Marinelli, T. Ryhanen, A. Morpurgo, J.N. Coleman, V. Nicolosi, L. Colombo, A. Fert, M. Garcia-Hernandez, A. Bachtold, G.F. Schneider, F. Guinea, C. Dekker, M. barbone, Z. Sun, C. Galiotis, A.N. Grigorenko, G. Konstantatos, A. Kis, M. Katsnelson, L. Vandersypen, A. Loiseau, V. Morandi, D. Neumaier, E. Treossi, J-H. Ahn, J. M. Kim, H. Zirath, B.J. van Wees, H. van der Zant, L. Occhipinti, A. Di Matteo, I.A. Kinloch, T. Seyller, E. Quesnel. X. Feng, K. Teo, N. Rupesinghe, P. Hakonen, S.R.T. Neil, Q. Tannock, T. Lofwander, and J. Kinaret, “Science and technology roadmap for graphene, related two-dimensional crystals, and hybrid systems,” Nanoscale, vol. 7, no. 11, pp. 4598-4810, 2015.

[16] H. Döscher, T. Schmaltz, C. Neef, A. Thielmann, and T. Reiss, “Graphene Roadmap Briefs (No. 2): industrialization status and prospects 2020,” Materials, vol. 8, no. 2, 022005, 2021.

[17] R. R. Nair, P. Blake, A.N. Grigorenko, K.S. Novoselov, T.J. Booth, T. Stauber, “Fine structure constant defines visual transparency of graphene,” Science, vol. 320, no. 5881, pp. 1308-1308, 2008.

[18] F. Federspiel, G. Froehlicher, M. Nasilowski, S. Pedetti, A. Mahmood, B. Doudin, S. Park, J.O. Lee, D. Halley, B. Dubertet, P. Gilliot, and S. Berciaud, “Distance dependence of the energy transfer rate from a single semiconductor nanostructure to graphene,” Nano Lett, vol. 15, no. 2, pp. 1252-1258, 2015.

[19] R. S. Swathi and K. L. Sebastian, “Resonance energy transfer from a dye molecule to graphene,” J Chem Phys, vol. 129, no. 5, 2008.

[20] L. Gaudreau, K. J. Tielrooij, G. E. D. K. Prawiroatmodjo, J. Osmond, F. J. G. De Abajo, and F. H. L. Koppens, “Universal distance-scaling of nonradiative energy transfer to graphene,” Nano Lett, vol. 13, no. 5, pp. 2030-2035, 2013.

[21] S. K. Murthy, “Nanoparticles in modern medicine: state of the art and future challenges.,” Int J Nanomedicine, vol. 2, no. 2, pp. 129-141, 2007.

[22] A. M. Szalai, G. Ferrari, L. Richter, J. Hartmann, M.Z. Kesici, B. Ji, K. Coshic, M.R.J. Dagleish, A. Jaeger, A. Aksimentiev, I. Tessmer, I. Kamińska, A.M. Vera, and P. Tinnefeld “Single-molecule dynamic structural biology with vertically arranged DNA on a fluorescence microscope,” Nat Methods, vol. 22, pp. 135-144, 2024.

[23] R. S. Swathi and K. L. Sebastian, “Long range resonance energy transfer from a dye molecule to graphene has (distance)-4 dependence,” Journal of Chemical Physics, vol. 130, no. 8, 2009.

[24] D. Mathur, A. Samanta, M.G. Ancona, S.A. Díaz, Y. Kim, J.S. Melinger, E.R. Goldman, J.P. Sadowski, L.L. Ong, P. Yin, and I.L. Medintz “Understanding Förster Resonance Energy Transfer in the Sheet Regime with DNA Brick-Based Dye Networks,” ACS Nano, vol. 15, no. 10, pp. 16452-16468, 2021.

[25] J. Chen and N. C. Seeman, “Synthesis from DNA of a molecule with the connectivity of a cube,” Nature, vol. 350, no. 6319, pp. 631-633, 1991.

[26] N. R. Kallenbach, R. I. Ma, and N. C. Seeman, “An immobile nucleic acid junction constructed from oligonucleotides,” Nature, vol. 305, no. 5937, pp. 829-831, 1983.

[27] M. McCarty and O. T. Avery, “Studies on the chemical nature of the substance inducing transformation of pneumococcal types,” J Exp Med, vol. 83, no. 2, pp. 97-104, 1946.

[28] J. Berg, J. Tymoczko, and L. Stryer, Biochemistry, 5th edition. 2002.

[29] J. D. Watson and F. H. C. Crick, “Molecular structure of nucleic acids: A structure for deoxyribose nucleic acid,” Nature, vol. 171, no. 4356, pp. 737-738, 1953.

[30] L. Mazzola, “Commercializing nanotechnology,” Nat Biotechnol, vol. 21, no. 10, pp. 1137-1143, 2003.

[31] M. L. Zhang, K.Q. Peng, X. Fan, J.S. Jie, R.Q. Zhang, S.T. Lee, S. T, and N.B. Wong, “Preparation of large-area uniform silicon nanowires arrays through metal-assisted chemical etching,” J Phys Chem C, vol. 112, no. 12, pp. 4444-4450, 2008.

[32] P. W. K. Rothemund, “Folding DNA to create nanoscale shapes and patterns,” Nature, vol. 440, no. 7082, pp. 297-302, 2006.

[33] P. Pitikultham, Z. Wang, Y. Wang, Y. Shang, Q. Jiang, and B. Ding, “Stimuli-Responsive DNA Origami Nanodevices and Their Biological Applications,” ChemMedChem, vol. 17, no. 1, e202100635, 2022.

[34] H. D. Li, P. Q. Ma, J. Y. Wang, B. C. Yin, and B. C. Ye, “A DNA Nanodevice-Based Platform with Diverse Capabilities,” Small, vol. 19, no. 37, 2302301, 2023.

[35] A. Jabbari, E. Sameiyan, E. Yaghoobi, M. Ramezani, M. Alibolandi, K. Abnous, and S.M. Taghdisi, “Aptamer-based targeted delivery systems for cancer treatment using DNA origami and DNA nanostructures,”Int J Pharm, 123448, 2023.

[36] Q. Jiang, Y. Shang, Y. Xie, and B. Ding, “DNA Origami: From Molecular Folding Art to Drug Delivery Technology,” Adv Mat, vol. 36, no. 22, 2301035, 2024.

[37] J. Marrs, Q. Lu, V. Pan, Y. Ke, and J. Hihath, “Structure-Dependent Electrical Conductance of DNA Origami Nanowires,” ChemBioChem, vol. 24, no. 2, e202200454, 2023.

[38] H. Lv, N. Xie, M. Li, M. Dong, C. Sun, Q. Zhang, L. Zhao, J. Li, X. Zuo, H. Chen, F. Wang, and C. Fan, “DNA-based programmable gate arrays for general-purpose DNA computing,” Nature, vol. 622, no. 7982, pp. 292-300, 2023.

[39] T. Tørring, N. V. Voigt, J. Nangreave, H. Yan, and K. V. Gothelf, “DNA origami: A quantum leap for self-assembly of complex structures,” Chem Soc Rev, vol. 40, no. 12, pp. 5636-5646, 2011.

[40] A. Gopinath, C. Thachuk, A. Mitskovets, H. A. Atwater, D. Kirkpatrick, and P. W. K. Rothemund, “Absolute and arbitrary orientation of single-molecule shapes,” Science, vol. 371, no. 6531, eabd6179, 2021.

[41] T. Zheng, C. O’Neill, J. F. Marshall, T. Iskratsch, and M. Palma, “Selective placement of functionalised DNA origami via thermal scanning probe lithography patterning,” Mater Adv, vol. 5, no. 23, pp. 9376-9382, 2024.

[42] K. Stokes, K. Clark, D. Odetade, M. Hardy, and P. Goldberg Oppenheimer, “Advances in lithographic techniques for precision nanostructure fabrication in biomedical applications,” Discover Nano, vol. 18, no. 1, 153, 2023.

[43] F. Pisano, A. Balena, M.F. Kashif, M. Pisanello, A. Qualtieri, L. Sileo, T. Stomeo, A. D’Orazio, M. De Vittorio, F. Pisanello, and M. Grande “Plasmonic sensing with FIB-milled 2D micro-arrays of truncated gold nano-pyramids,” arXiv preprint, 1910.06398, 2019.

[44] L. Sala, A. Zerolová, V. Vizcaino, A. Mery, A. Domaracka, H. Rothard, P. Boduch, D. Pinkas, and J.Kocišek “Ion beam processing of DNA origami nanostructures,” Beilstein J Nanotechnol, vol. 15, pp. 207-214, 2024.

[45] P. Li, S. Chen, H. Dai, Z. Yang, Z. Chen, Y. Wang, Y. Chen, W. Shan, W. Peng, and H. Duan, “Recent advances in focused ion beam nanofabrication for nanostructures and devices: fundamentals and applications,” Nanoscale, vol. 13, no. 3, pp. 1529-1565, 2021.

[46] N. C. Seeman, “Nucleic acid junctions and lattices,” J Theor Biol, vol. 99, no. 2, pp. 237-247, 1982.

[47] N. C. Seeman, “DNA engineering and its application to nanotechnology,” Trends Biotechnol, vol. 17, no. 11, pp. 437-443, 1999.

[48] T. H. LaBean, H. Yan, J. Kopatsch, F. Liu, E. Winfree, J.H. Reif, and N.C. Seeman, “Construction, analysis, ligation, and self-assembly of DNA triple crossover complexes,” J Am Chem Soc, vol. 122, no. 9, pp. 1848-1860, 2000.

[49] P. Yin, R.F. Hariadi, S. Sahu, H.M. Choi, S.H. Park, T.H. LaBean, and J.H. Reif, “Programming DNA tube circumferences,” Science, vol. 321, no. 5890, pp. 824-826, 2008.

[50] B. Wei, M. Dai, and P. Yin, “Complex shapes self-assembled from single-stranded DNA tiles,” Nature, vol. 485, no. 7400, pp. 623-626, 2012.

[51] Y. Ke, L. L. Ong, W. M. Shih, and P. Yin, “Three-dimensional structures self-assembled from DNA bricks,” Science, vol. 338, no. 6111, pp. 1177-1183, 2012.

[52] L. L. Ong, N. Hanikel, O.K. Yaghi, C. Grun, M.T. Strauss, P. Bron, J. Lai-Kee-Him, F. Schueder, B. Wang, P. Wang, J.Y. Kishi, C. Myhrvold, A. Zhu, R. Jungmann, G. Bellot, Y. Ke, and P. Yin, “Programmable self-assembly of three-dimensional nanostructures from 10,000 unique components,” Nature, vol. 552, no. 7683, pp. 72-74, 2017.

[53] B. Jeon, M.M. Guareschi, J.M. Stewart, E. Wu, A. Gopinath, N. Arroyo-Currás, P. Dauphin-Ducharme, K.W. Plaxco, P.S. Lukeman, and P.W.K. Rothemund, “Modular DNA

origami-based electrochemical detection of DNA and proteins,"Proc Natl Acad Sci, vol. 122, no. 1, e2311279121, 2023.

[54] S. H. Suh, Y. Xing, A. Rottensteiner, R. Zhu, Y.J. Oh, S. Howorka, and P. Hinterdorfer, "Molecular Recognition in Confined Space Elucidated with DNA Nanopores and Single-Molecule Force Microscopy," Nano Lett, vol. 23, no. 10, pp. 4439-4447, 2023.

[55] A. Y. Koyfman, G. B. Braun, and N. O. Reich, "Cell-targeted self-assembled DNA nanostructures," J Am Chem Soc, vol. 131, no. 40, pp. 14237-14239, 2009.

[56] J. I. Cutler, E. Auyeung, and C. A. Mirkin, "Spherical nucleic acids," J Am Chem Soc, vol. 134, no. 3, pp. 1376-1391, 2012.

[57] D. S. Seferos, A. E. Prigodich, D. A. Giljohann, P. C. Patel, and C. A. Mirkin, "Polyvalent DNA nanoparticle conjugates stabilize nucleic acids," Nano Lett, vol. 9, no. 1, pp. 308-311, 2009.

[58] N. L. Rosi, D. A. Giljohann, C. S. Thaxton, A. K. R. Lytton-Jean, M. S. Han, and C. A. Mirkin, "Oligonucleotide-modified gold nanoparticles for intracellular gene regulation," Science, vol. 312, no. 5776, pp. 1027-1030, 2006.

[59] S. H. Alamudi, X. Liu, and Y.-T. Chang, "Azide-based bioorthogonal chemistry: Reactions and its advances in cellular and biomolecular imaging," Biophys Rev, vol. 2, no. 2, 2021.

[60] A. H. El-Sagheer and T. Brown, "Click chemistry with DNA," Chem Soc Rev, vol. 39, no. 4, pp. 1388-1405, 2010.

[61] Q. Jiang, C. Song, C., J. Nangreave, X. Liu, L. Lin, D. Qiu, Z-G. Wang, G. Zou, X. Liang, H. Yan, and B. Ding, "DNA origami as a carrier for circumvention of drug resistance," J Am Chem Soc, vol. 134, no. 32, pp. 13396-13403, 2012.

[62] Q. Zhang, Q. Jiang, N. Li, L. Dai, Q. Liu, L. Song, J. Wang, Y. Li, J. Tian, B. Ding, and Y. Du, "DNA origami as an in vivo drug delivery vehicle for cancer therapy," ACS Nano, vol. 8, no. 7, pp. 6633-6643, 2014.

[63] Y. Amir, E. Ben-Ishay, D. Levner, S. Ittah, A. Abu-Horowitz, and I. Bachelet, "Universal computing by DNA origami robots in a living animal," Nat Nanotechnol, vol. 9, no. 5, pp. 353-357, 2014.

[64] S. M. Douglas, I. Bachelet, and G. M. Church, "A logic-gated nanorobot for targeted transport of molecular payloads," Science, vol. 335, no. 6070, pp. 831-834, 2012.

[65] L. Shen, P. Wang, and Y. Ke, “DNA Nanotechnology-Based Biosensors and Therapeutics,” Adv Healthc Mater, vol. 10, no. 15, 2002205, 2021.

[66] M. Scheckenbach, J. Bauer, J. Zähringer, F. Selbach, and P. Tinnefeld, “DNA origami nanorulers and emerging reference structures,” APL Mater, vol. 8, no. 11, 2020.

[67] E. Büber, R. Yaadav, T. Schröder, H. G. Franquelim, and P. Tinnefeld, “DNA Origami Vesicle Sensors with Triggered Single-Molecule Cargo Transfer,” Angew Chem Int Ed, vol. 63, no. 49, e202408295, 2024.

[68] V. Glembockyte, L. Grabenhorst, K. Trofymchuk, and P. Tinnefeld, “DNA Origami Nanoantennas for Fluorescence Enhancement,” Acc Chem Res, vol. 54, no. 17, pp. 3338-3348, 2021.

[69] A. Puchkova, C. Vietz, E. Pibiri, B. Wünsch, M. Sanz Paz, G. Acuna, and P. Tinnefeld, “DNA Origami Nanoantennas with over 5000-fold Fluorescence Enhancement and Single-Molecule Detection at 25 μm,” Nano Lett, vol. 15, no. 12, pp. 8354-8359, 2015.

[70] Y. T. E. Chiu, H. Li, and C. H. J. Choi, “Progress toward Understanding the Interactions between DNA Nanostructures and the Cell,” Small, vol. 15, no. 26, 1805416, 2019.

[71] S. M. Douglas, H. Dietz, T. Liedl, B. Högberg, F. Graf, and W. M. Shih, “Self-assembly of DNA into nanoscale three-dimensional shapes,” Nature, vol. 459, no. 7245, pp. 414-418, 2009.

[72] E. S. Andersen, M. Dong, M.M. Nielsen, K. Jahn, R. Subraman, W. Mamdouh, M.M. Golas, B. Sander, H. Stark, C.L.P. Oliverira, J.S. Pedersen, V. Birkedal, F. Basenbacher, K.V. Gothelf, and J. Kjems, “Self-assembly of a nanoscale DNA box with a controllable lid,” Nature, vol. 459, no. 7243, pp. 73-76, 2009.

[73] S. M. Douglas, A. H. Marblestone, S. Teerapittayanon, A. Vazquez, G. M. Church, and W. M. Shih, “Rapid prototyping of 3D DNA-origami shapes with caDNAno,” Nucleic Acids Res, vol. 37, no. 15, pp. 5001-5006, 2009.

[74] C. E. Castro, F. Kilchherr, D.N. Kim, E.L. Shiao, T. Wauer, P. Wortmann, “A primer to scaffolded DNA origami,” Nat Methods, vol. 8, no. 3, pp. 221-229, 2011.

[75] D. N. Kim, F. Kilchherr, H. Dietz, and M. Bathe, “Quantitative prediction of 3D solution shape and flexibility of nucleic acid nanostructures,” Nucleic Acids Res, vol. 40, no. 7, pp. 2862-2868, 2012.

[76] B. Szabó and I. Babuška, Introduction to Finite Element Analysis: Formulation, Verification and Validation, vol.35, John Wiley & Sons, 2011.

[77] Y. Hu and C. M. Niemeyer, “From DNA Nanotechnology to Material Systems Engineering,” Advanced Materials, vol. 31, no. 26, 1806294, 2019.

[78] M. Madsen and K. V. Gothelf, “Chemistries for DNA Nanotechnology,” Chem Rev, vol. 119, no. 10, pp. 6384-6458, 2019.

[79] L. Richter, A. M. Szalai, C. L. Manzanares-Palenzuela, I. Kamińska, and P. Tinnefeld, “Exploring the Synergies of Single-Molecule Fluorescence and 2D Materials Coupled by DNA,” Adv Mat, vol. 35, no. 41, 2303152, 2023.

[80] E. Roth, A. Glick Azaria, O. Girshevitz, A. Bitler, and Y. Garini, “Measuring the Conformation and Persistence Length of Single-Stranded DNA Using a DNA Origami Structure,” Nano Lett, vol. 18, no. 11, pp. 6703-6709, 2018.

[81] Q. Du, C. Smith, N. Shiffeldrim, M. Vologodskaia, and A. Vologodskii, “Cyclization of short DNA fragments and bending fluctuations of the double helix,” Proc Natl Acad Sci U S A, vol. 102, no. 15, pp. 5397-5402, 2005.

[82] B. Liu, S. Salgado, V. Maheshwari, and J. Liu, “DNA adsorbed on graphene and graphene oxide: Fundamental interactions, desorption and applications,” Curr opin Colloid In, vol. 26, pp. 41-49, 2016.

[83] S. Zeng, L. Chen, Y. Wang, and J. Chen, “Exploration on the mechanism of DNA adsorption on graphene and graphene oxide via molecular simulations,” J Phys D Appl Phys, vol. 48, no. 27, 275402, 2015.

[84] S. Garaj, S. Liu, J. J. a Golovchenko, D. Branton, and J. J. a Golovchenko, “Super-sensitive Molecule-hugging Graphene Nanopores,” Proc Natl Acad Sci, vol. 110, no. 30, pp. 12192-12196, 2013.

[85] A. Kakatkar, T. S. Abhilash, R. De Alba, J. M. Parpia, and H. G. Craighead, “Detection of DNA and poly-l-lysine using CVD graphene-channel FET biosensors,” Nanotechnology, vol. 26, no. 12, 125502, 2015.

[86] P. J. J. Huang and J. Liu, “Separation of short single-and double-stranded dna based on their adsorption kinetics difference on graphene oxide,” Nanomaterials, vol. 3, no. 2, pp. 221-228, 2013.

[87] D. B. Wells, M. Belkin, J. Comer, and A. Aksimentiev, “Assessing graphene nanopores for sequencing DNA,” Nano Lett, vol. 12, no. 8, pp. 4117-4123, 2012.

[88] H. Zhang, H. Zhang, A. Aldalbahi, X. Zuo, C. Fan, and X. Mi, “Fluorescent biosensors enabled by graphene and graphene oxide,” Biosens Bioelectron, vol. 89, pp. 96-106, 2017.

[89] Y. Gao and Y. Wang, “Interplay of graphene-DNA interactions: Unveiling sensing potential of graphene materials,” Appl Phys Rev, vol. 1, no. 1, 2024.

[90] C. H. Lu, H. H. Yang, C. L. Zhu, X. Chen, and G. N. Chen, “A graphene platform for sensing biomolecules,” Angew Chem Int Ed, vol. 48, no. 26, pp. 4879-4881, 2009.

[91] N. S. Green and M. L. Norton, “Interactions of DNA with graphene and sensing applications of graphene field-effect transistor devices: A review,” Anal Chim Acta, vol. 853, pp. 127-142, 2015.

[92] A. M. Szalai, G. Ferrari, L. Richter, J. Hartmann, M.Z. Kesici, B. Ji, K.Coshic, A. Aksimentiev, I. Tessmer, I. Kamińska, A.M.Vera, and P. Tinnefeld, “Real-Time Structural Biology of DNA and DNA-Protein Complexes on an Optical Microscope,” bioRxiv, 2023.

[93] W. E. Moerner, “A dozen years of single-molecule spectroscopy in physics, chemistry, and biophysics,” J Phys Chem B, vol. 106, no. 5, pp. 910-927, 2002.

[94] W. E. Moerner and M. Orrit, “Illuminating single molecules in condensed matter,” Science, vol. 283, 5408, pp. 1670-1676, 1999.

[95] W. E. Moerner and D. P. Fromm, “Methods of single-molecule fluorescence spectroscopy and microscopy,” Rev Sci Instrum, vol. 74, no. 8, pp. 3597-3619, 2003.

[96] M. Pfeiffer, K. Trofymchuk, S. Ranallo, F. Ricci, F. Steiner, F. Cole, V. Glembockyte, and P. Tinnefeld, “Single antibody detection in a DNA origami nanoantenna,” Iscience, vol. 24, no. 9, 2021.

[97] S. E. Ochmann, H. Joshi, E. Büber, H.G. Franquelim, P. Stegemann, B. Saccà, “DNA Origami Voltage Sensors for Transmembrane Potentials with Single-Molecule Sensitivity,” Nano Lett, vol. 21, no. 20, pp. 8634-8641, 2021.

[98] R. Jungmann, C. Steinhauer, M. Scheible, A. Kuzyk, P. Tinnefeld, and F. C. Simmel, “Single-molecule kinetics and super-resolution microscopy by fluorescence imaging of transient binding on DNA origami,” Nano Lett, vol. 10, no. 11, pp. 4756-4761, 2010.

[99] L. Manzanares, D. Spurling, A.M. Szalai, T. Schröder, E. Büber, G. Ferrari, G, M.R.J. Dagleish, V. Nicolosi, and P. Tinnefeld “2D Titanium Carbide MXene and Single-Molecule Fluorescence: Distance-Dependent Nonradiative Energy Transfer and Leaflet-Resolved Dye Sensing in Lipid Bilayers,” Adv Mat, vol. 36, no. 49, 2024.

[100] P. Tinnefeld and M. Sauer, “Branching out of single-molecule fluorescence spectroscopy: Challenges for chemistry and influence on biology,” Angew. Chem. Int. Ed. vol. 44, no. 18, pp. 2642-2671, 2005.

[101] S. Weiss, “Fluorescence spectroscopy of single biomolecules,” Science, vol. 283, 5408, pp. 1676-1683, 1999.

[102] P. Tinnefeld and T. Cordes, “‘Self-healing’ dyes: Intramolecular stabilization of organic fluorophores,” Nat Methods, vol. 9, pp. 426-427, 2012.

[103] J. H. Smit, J.H. van der Velde, J. Huang, V. Trauschke, S.S. Henrikus, S. Chen, N. Eleftheriadis, E.M. Warszawik, A. Hermann, and T. Cordes“On the impact of competing intra- and intermolecular triplet-state quenching on photobleaching and photoswitching kinetics of organic fluorophores,”, Phys Chem Chem Phys, vol. 21, no. 7 , pp. 3721-3733, 2019.

[104] D. Sirbu, O. J. Woodford, A. C. Benniston, and A. Harriman, “Photocatalysis and self-catalyzed photobleaching with covalently-linked chromophore-quencher conjugates built around BOPHY,” Photochemical & Photobiological Sciences, vol. 17, no. 6, pp. 750–762, 2018

[105] T. Ha and P. Tinnefeld, “Photophysics of fluorescent probes for single-molecule biophysics and super-resolution imaging,” Annu Rev Phys Chem, vol. 63, no. 1, pp. 595-617, 2012.

[106] J. Vogelsang, R. Kasper, C. Steinhauer, B. Person, M. Heilemann, M. Sauer, and P. Tinnefeld “A Reducing and Oxidizing System Minimizes Photobleaching and Blinking of Fluorescent Dyes,” Angewandte Chemie International Edition, vol. 47, no. 29, pp. 5465–5469, 2008.

[107] T. Cordes, J. Vogelsang, and P. Tinnefeld, “On the Mechanism of Trolox as Antiblinking and Antibleaching Reagent,” J Am Chem Soc, vol. 131, no. 14, pp. 5018–5019, 2009.

[108] H. Schneckenburger and V. Richter, “Laser scanning versus wide-field—choosing the appropriate microscope in life sciences,” Appl Sci, vol. 11, no. 2, 733, 2021.

[109] J. R. Lakowicz, Principles of fluorescence spectroscopy. 2006.

[110] V. Panchal, Y. Yang, G. Cheng, J. Hu, M. Kruskopf, C.I. Liu, A.F. Rigosi, C. Melios, A.R> Hight Walker, D.B. Newell, O. Kazakova, and R.E Elmquist “Confocal laser scanning

microscopy: A tool for rapid optical characterization of 2D materials," arXiv Mesoscale and Nanoscale Physics, no. 2018, 2018.

[111] S. W. Paddock, "Principles and Practices of Laser Scanning Confocal Microscopy," Mol Biotechnol, vol. 16, no. 2, pp. 127–150, 2000.

[112] T. Umakoshi, S. Fukuda, T. Uchihashi, P. Verma, and T. Ando, "High-speed Scanning Near-field Optical Microscopy," in JSAP-OSA Joint Symposia 2018, Washington, D.C.: Optica Publishing Group, p. 19a_211B_1, 2018.

[113] E. Betzig, "Principles and Applications of Near-Field Scanning Optical Microscopy (NSOM)," in Near Field Optics, Dordrecht: Springer Netherlands, pp. 7–15, 1993.

[114] R. Rigler, U. Mets, J. Widengren, and P. Kask, "Fluorescence correlation spectroscopy with high count rate and low background: analysis of translational diffusion," European Biophysics Journal, vol. 22, no. 3, pp. 169-175, 1993.

[115] A. Brenneis, L. Gaudreau, M. Seifert, H. Karl, M.S. Brandt, H. Huebl, J.A. Garrido, F.H.L. Koppens, and A.W. Holleitner, "Ultrafast electronic readout of diamond nitrogen-vacancy centres coupled to graphene," Nat Nanotechnol, vol. 10, no. 2, pp. 135-139, 2015.

[116] H. Gonçalves, C. Bernardo, C. Moura, R.A.S. Ferreira, P.S. André, T. Stauber, M. Belsley, and P. Schellenberg, "Long range energy transfer in graphene hybrid structures," J Phys D Appl Phys, vol. 49, no. 31, 315102, 2016.

[117] Z. Jin, W. Sun, Y. Ke, C.J. Shih, G.L. Paulus, Q. Hua Wang, B. Mu, P. Yin, and M.S. Strano "Metallized DNA nanolithography for encoding and transferring spatial information for graphene patterning," Nat Commun, vol. 4, no. 1, 1663, 2013.

[118] Y. Kabiri, A.N. Ananth, J. van der Torre, A. Katan, J.Y. Hong, S. Malladi, J.Kong, H. Zandbergen, and C. Dekker, "Distortion of DNA origami on graphene imaged with advanced TEM techniques," Small, vol. 13, no. 31, pp. 1700876, 2017.

[119] N. S. Green, P. H. Q. Pham, D. T. Crow, P. J. Burke, and M. L. Norton, "Layered graphene-mica substrates induce melting of DNA origami," Mater Res Express, vol. 5, no. 4, 045035, 2018.

[120] A. R. Brill, E. Koren, and G. de Ruiter, "Molecular functionalization of 2D materials: From atomically planar 2D architectures to off-plane 3D functional materials," J Mat Chem C vol. 9.no. 35, pp. 11569-11587, 2021.

[121] V. Georgakilas, J.N. Tiwari, K.C. Kemp, J.A. Perman, A.B. Bourlinos, K.S. Kim, and R. Zboril, "Noncovalent functionalization of graphene and graphene oxide for energy

materials, biosensing, catalytic, and biomedical applications," Chem Rev, vol. 116, no. 9, pp. 5464-5519, 2016.

[122] M. Assali, N. Kittana, I. Badran, and S. Omari, "Covalent functionalization of graphene sheets for plasmid DNA delivery: experimental and theoretical study," RSC Adv, vol. 13, no. 10, pp. 7000-7008, 2023.

[123] G. H. Yang, D. D. Bao, H. Liu, D.Q. Zhang, N. Wang, and H.T. Li, "Functionalization of Graphene and Applications of the Derivatives," J. Inorg. Organomet. Polym. Mater., vol. 27, pp. 1129-1141, 2017.

[124] A. J. Clancy, H. Au, N. Rubio, G. O. Coulter, and M. S. P. Shaffer, "Understanding and controlling the covalent functionalisation of graphene," Dalton Transactions, vol. 49, no. 30, pp. 10308-10318, 2020.

[125] H. C. Lee, W-W. Liu, S-P. Chai, A.R. Mohamed, A. Aziz, C-S. Khe, N.M.S> Hidayah, and U. Hashim "Review of the synthesis, transfer, characterization and growth mechanisms of single and multilayer graphene," RSC advances, vol. 7, no. 26, pp. 15644-15693, 2017.

[126] M. Huang and R. S. Ruoff, "Growth of Single-Layer and Multilayer Graphene on Cu/Ni Alloy Substrates," Acc Chem Res, vol. 53, no. 4, pp. 800-811, 2020.

[127] X. Chen, L. Zhang, and S. Chen, "Large area CVD growth of graphene," Synth Met, vol. 210, pp. 95-108, 2015.

[128] H. J. Park, J. Meyer, S. Roth, and V. Skákalová, "Growth and properties of few-layer graphene prepared by chemical vapor deposition," Carbon, vol. 48, no. 4, pp. 1088-1094, 2010.

[129] Y. M. Chang, H. Kim, J. H. Lee, and Y. W. Song, "Multilayered graphene efficiently formed by mechanical exfoliation for nonlinear saturable absorbers in fiber mode-locked lasers," Appl Phys Lett, vol. 97, no. 21, 2010.

[130] Y. X. Fu, X. M. Wang, D. C. Mo, and S. S. Lu, "Production of monolayer, trilayer, and multi-layer graphene sheets by a re-expansion and exfoliation method," J Mater Sci, vol. 49, no. 5, pp. 2315-2323, 2014.

[131] R. V. Salvatierra, S. H. Domingues, M. M. Oliveira, and A. J. G. Zarbin, "Tri-layer graphene films produced by mechanochemical exfoliation of graphite," Carbon, vol. 57, pp. 410-415, 2013.

[132] A. V. Alaferdov, A. Gholamipour-Shirazi, M. A. Canesqui, Y. A. Danilov, and S. A. Moshkalev, “Size-controlled synthesis of graphite nanoflakes and multi-layer graphene by liquid phase exfoliation of natural graphite,” Carbon, vol. 69, pp. 525-535, 2014.

[133] Y. Xu, H. Cao, Y. Xue, B. Li, and W. Cai, “Liquid-phase exfoliation of graphene: An overview on exfoliation media, techniques, and challenges,” Nanomaterials vol. 8, no. 11, 942, 2018.

[134] Y. Hernandez, V. Nicolosi, M. Lotya, F.M. Blighe, Z. Sun, S. De, I.T. McGovern, B. Holland, M. Byrne, Y.K. Gun’Ko, J.J. Boland, P. Niraj, G. Duesberg, S. Krishnamurthy, R. Goodhue, J. Hutchison, V. Scardaci, A.C. Ferrari, and J.N. Coleman, “High-yield production of graphene by liquid-phase exfoliation of graphite,” Nat Nanotechnol, vol. 3, no. 9, pp. 563-568, 2008.

[135] Z. Li, R.J. Young, C. Backes, W. Zhao, X. Zhang, A.A. Zhukov, E. Tillotson, A.P. Conlan, F. Ding, S.J. Haigh, K.S. Novoselov, and J.N. Coleman (2020). Mechanisms of liquid-phase exfoliation for the production of graphene. ACS Nano, vol. 14, no. 9, pp. 10976-10985, 2010.

[136] J. Hass, W. A. De Heer, and E. H. Conrad, “The growth and morphology of epitaxial multilayer graphene,” Condensed Matter, vol. 20, no. 32, 323202, 2008.

[137] B. Sharma, T. Schumann, M. H. de Oliveira, and J. M. J. Lopes, “Controlled synthesis and characterization of multilayer graphene films on the C-face of silicon carbide,” Physica Status Solidi (A) Applications and Materials Science, vol. 214, no. 5, 1600721, 2017.

[138] M. Sprinkle, J. Hicks, A. Tejeda, A. Taleb-Ibrahimi, P. Le Fevre, F. Bertran, H. Tinkey, M.C. Clark, P. Soukiassian, D. Martinotti, J. Hass, and E.H. Conrad, “Multilayer epitaxial graphene grown on the surface; structure and electronic properties.”, Journal of Physics D: Applied Physics, vol. 43, no. 37, 374006, 2010.

[139] O. Ustavytska, Y. Kurys, V. Koshechko, and V. Pokhodenko, “One-Step Electrochemical Preparation of Multilayer Graphene Functionalized with Nitrogen,” Nanoscale Res Lett, vol. 12, no. 1, pp. 1-7, 2017.

[140] F. Liu, C. Wang, X. Sui, M.A. Riaz, M. Xu, M., L. Wei, and Y. Chen, “Synthesis of graphene materials by electrochemical exfoliation: Recent progress and future potential,” Carbon Energy, vol. 1, no. 2, pp. 173-199, 2019.

[141] K. F. Mak, M. Y. Sfeir, J. A. Misewich, and T. F. Heinza, “The evolution of electronic structure in few-layer graphene revealed by optical spectroscopy,” Proc Natl Acad Sci U S A, vol. 107, no. 34, pp. 14999-15004, 2010.

[142] S. Yuan, H. De Raedt, and M. I. Katsnelson, “Electronic transport in disordered bilayer and trilayer graphene,” Phys Rev B Condens Matter Mater Phys, vol. 82, no. 23, 235409, 2010.

[143] S. E. Zhu, S. Yuan, and G. C. A. M. Janssen, “Optical transmittance of multilayer graphene,” EPL, vol. 108, no. 1, 17007, 2014.

[144] K. Gundra and A. Shukla, “Band structure and optical absorption in multilayer armchair graphene nanoribbons: A Pariser-Parr-Pople model study,” Phys Rev B Condens Matter Mater Phys, vol. 84, no. 7, 075442, 2011.

[145] F. Cellini, F. Lavini, C. Berger, W. De Heer, and E. Riedo, “Layer dependence of graphene-diamene phase transition in epitaxial and exfoliated few-layer graphene using machine learning,” 2d Mater, vol. 6, no. 3, 035043, 2019.

[146] C. Androulidakis, E. N. Koukaras, M. Hadjinicolaou, and C. Galiotis, “Non-Eulerian behavior of graphitic materials under compression,” Carbon, vol. 138, pp. 227-233, 2018.

[147] Z. Yan, D. L. Nika, and A. A. Balandin, “Thermal properties of graphene and few-layer graphene: Applications in electronics,” IET Circuits, Devices and Systems, vol. 9, no. 1, pp. 4-12, 2015.

[148] S. Ghosh, W. Bao, D.L. Nika, S. Subrina, E.P. Pokatilov, C.N. Lau, and A.A. Balandin “Dimensional crossover of thermal transport in few-layer graphene,” Nat Mater, vol. 9, no. 7, pp. 555-558, 2010.

[149] W. R. Zhong, M. P. Zhang, B. Q. Ai, and D. Q. Zheng, “Chirality and thickness-dependent thermal conductivity of few-layer graphene: A molecular dynamics study,” Appl Phys Lett, vol. 98, no. 11, 113107, 2011.

[150] V. G. Kravets, A.N. Grigorenko, R.R. Nair, P. Blake, S. Anissimova, K.S. Novoselov, and A.K. Geim “Spectroscopic ellipsometry of graphene and an exciton-shifted van Hove peak in absorption,” Phys Rev B Condens Matter Mater Phys, vol. 81, no. 15, p.155413, 2010

[151] Y. Zhang, T-T. tang, C. Girit, Z. Hao, M.C. Martin, A. Zettl, M.F. Crommie, Y.R. Shen, and F. Wang “Direct observation of a widely tunable bandgap in bilayer graphene,” Nature, vol. 459, no. 7248, pp. 820-823, 2009.

[152] T. Ohta, A. Bostwick, T. Seyller, K. Horn, and E. Rotenberg, “Controlling the electronic structure of bilayer graphene,” Science, vol. 313, no. 5789, pp. 951-954, 2006.

[153] Y. Sui and J. Appenzeller, “Screening and interlayer coupling in multilayer graphene field-effect transistors,” Nano Lett, vol. 9, no. 8, pp. 2973-2977, 2009.

[154] A. Yacoby, “Graphene: Tri and tri again,” Nat Phys, vol. 7, no. 12, pp. 925-926, 2011.

[155] A. K. Geim and I. V. Grigorieva, “Van der Waals heterostructures,” Nature, vol. 499, no. 7459, pp. 419-425, 2013.

[156] Y. Liu, N. O. Weiss, X. Duan, H. C. Cheng, Y. Huang, and X. Duan, “Van der Waals heterostructures and devices,” Nat Rev Mater, vol. 1, no. 9, pp. 1-17, 2016.

[157] J. Wang, F. Ma, W. Liang, R. Wang, and M. Sun, “Optical, photonic and optoelectronic properties of graphene, h-NB and their hybrid materials,” Nanophotonics, vol. 6, no. 5, pp. 943-976, 2017.

[158] Z. Liu, L. Ma, G. Shi, W. Zhou, Y. Gong, S. Lei, X. Yang, J. Zhang, J. Yu, K.P. Hackenberg, A. Babakhani, J-C. Idrobo, R. Vajtai, J. Lou, and P. M. Ajayan “In-plane heterostructures of graphene and hexagonal boron nitride with controlled domain sizes,” Nat Nanotechnol, vol. 8, no. 2, pp. 119-124, 2013.

[159] G. Chen, “Correlated and topological physics in ABC-trilayer graphene moiré superlattices”, Quantum Frontiers, vol. 1, no. 8, 2022.

[160] K. Watanabe, T. Taniguchi, and H. Kanda, “Direct-bandgap properties and evidence for ultraviolet lasing of hexagonal boron nitride single crystal,” Nat Mater, vol. 3, no. 6, pp. 404-409, 2004.

[161] J. D. Caldwell, I. Aharonovich, G. Cassabois, J. H. Edgar, B. Gil, and D. N. Basov, “Photonics with hexagonal boron nitride,” vol. 4, no. 8, pp. 552-567, 2019.

[162] J. Wang, F. Ma, and M. Sun, “Graphene, hexagonal boron nitride, and their heterostructures: properties and applications,” vol. 7, no. 27, pp. 16801-16822, 2017.

[163] K. Zhang, Y. Feng, F. Wang, Z. Yang, and J. Wang, “Two dimensional hexagonal boron nitride (2D-hBN): Synthesis, properties and applications,” vol. 5, no. 46, pp. 11992-12022, 2017.

[164] C. R. Dean, A.F. Young, I. Meric, C. Lee, L. Wang, S. Sorgenfrei, K. Watanabe, T. Taniguchi, P. Kim, K.L. Shepard, and J. Hone “Boron nitride substrates for high-quality graphene electronics,” Nat Nanotechnol, vol. 5, no. 10, pp. 722-726, 2010.

[165] E. Kim, T. Yu, E. Sang Song, and B. Yu, “Chemical vapor deposition-assembled graphene field-effect transistor on hexagonal boron nitride,” Appl Phys Lett, vol. 98, no. 26, 2011.

[166] J. Wang, S. Cao, P. Sun, Y. Ding, Y. Li, and F. Ma, “Optical advantages of graphene on the boron nitride in visible and SW-NIR regions,” RSC Adv, vol. 6, no. 112, pp. 111345-111349, 2016.

[167] F. Pizzocchero, L. Gammelgaard, B.S. Jessen, J.M. Caridad, L. Wang, J. Hone, P. Bøggild, and T.J. Booth “The hot pick-up technique for batch assembly of van der Waals heterostructures,” Nat Commun, vol. 7, no. 11894, 2016.

[168] Q. Cai, W. Gan, A. Falin, K. Watanabe, T. Taniguchi, J. Zhuang, W. Hao, S. Huang, t. Tao, Y. Chen, and L.H. Li “Two-Dimensional Van der Waals Heterostructures for Synergistically Improved Surface-Enhanced Raman Spectroscopy,” ACS Appl Mater Interfaces, vol. 12, no. 19, pp. 21985-21991, 2020.

[169] L. Britnell, R.V. Gorbachev, r. Jalil, B.D. Belle, F. Schedin, A. Mishchenko, T. Georgiou, M.I. Katsnelson, l. Eaves, S.V. Morozov, N.M.R. Peres, J. Leist, A.K. Geim, K.S. Novoselov, and L.A. Ponomarenko “Field-effect tunneling transistor based on vertical graphene heterostructures,” Science, vol. 335, no. 6071, pp. 947-950, 2012.

[170] A. V. Kretinin, Y. Cao, J.S. Tu, G.L. Yu, R. Jalil, K>S> Novoselov, S.J. Haigh, A. Gholinia, A. Mishchenko, M. Lozada, T. Georgiou, C.R. Woods, F. Withers, P. Blake, G. Eda, A. Wirsig, C. Hucho, K. Watanabe, T. Taniguchi, A.K. Geim and R.V. Gorbachev “Electronic properties of graphene encapsulated with different two-dimensional atomic crystals,” Nano Lett, vol. 14, no. 6, pp. 3270-3276, 2014.

[171] J. Sülzle, W. Yang, Y. Shimoda, N. Ronceray, E. mayner, S. Manley, and A. Radenovic “Label-Free Imaging of DNA Interactions with 2D Materials,” ACS Photonics, vol. 11, no. 2, pp. 737-744, 2024.

[172] X. Yang, D.H. Shin, Z. Yu, K. Watanabe, T. Taniguchi, V. babenko, S. Hofmann, and S. Caneva “Hexagonal Boron Nitride Spacers for Fluorescence Imaging of Biomolecules,” ChemNanoMat, vol. 10, no. 5, e202300592, 2024.

[173] Q. Lin, X. Zou, G. Zhou, R. Liu, J. Wu, J. Li, and W. Duan “Adsorption of DNA/RNA nucleobases on hexagonal boron nitride sheet: An ab initio study,” Physical Chemistry Chemical Physics, vol. 13, no. 26, pp. 12225-12230, 2011.

[174] L. Zhang and X. Wang, “DNA sequencing by hexagonal boron nitride nanopore: A computational study,” Nanomaterials, vol. 6, no. 6, p. 111, 2016.

[175] B. Luan and R. Zhou, “Spontaneous ssDNA stretching on graphene and hexagonal boron nitride in plane heterostructures,” Nat Commun, vol. 10, no. 1, pp. 1-9, 2019.

[176] B. Luan and M. A. Kuroda, “Electrophoretic transport of single-stranded DNA through a two-dimensional nanopore patterned on an in-plane heterostructure,” ACS Nano, vol. 14, no. 10, pp. 11540-11546, 2020.

[177] Z. He and R. Zhou, “Exploring an In-Plane Graphene and Hexagonal Boron Nitride Array for Separation of Single Nucleotides,” ACS Nano, vol. 15, no. 7, pp.11600-11607, 2021.

[178] V. Shukla, N. K. Jena, A. Grigoriev, and R. Ahuja, “Prospects of Graphene-hBN Heterostructure Nanogap for DNA Sequencing,” ACS Appl Mater Interfaces, vol. 9, no. 46, pp. 39945-39952, 2017.

[179] Y. Zhan, J. Yan, M. Wu, L. Guo, Z. Lin, B. Qiu, G. Chen, and K. Wong “Boron nitride nanosheets as a platform for fluorescence sensing,” Talanta, vol. 174, pp. 365-371, 2017.

[180] X. Li, S. Chen, Q. Liu, Y. Luo, and X. Sun, “Hexagonal boron nitride nanosheet as an effective nanoquencher for the fluorescence detection of microRNA,” Chemical Communications, vol. 57, no. 65, pp. 8039-8042, 2021.

[181] M. H. Alshehri, F. Z. Duraihem, and M. A. Aba Oud, “Instability and translocation through nanopores of DNA interacting with single-layer materials,” RSC Adv, vol. 10, no. 61, pp. 36962-36970, 2020.

[182] S. Liu, B. Lu, Q. Zhao, J. Li, T. Gao, Y. Chen, Y. Zhang, Z. Liu, Z. Fan, F. Yang, L. You, and D. Yu “Boron nitride nanopores: Highly sensitive DNA single-molecule detectors,” Advanced Materials, vol. 25, no. 33, pp. 4549-4554, 2013.

[183] A. K. Manna and S. K. Pati, “Theoretical understanding of single-stranded DNA assisted dispersion of graphene,” J Mater Chem B, vol. 1, no. 1, pp. 91-100, 2013.

[184] S. Muraru, C. G. Samoila, E. I. Slusanschi, J. S. Burns, and M. Ionita, “Molecular dynamics simulations of DNA adsorption on graphene oxide and reduced graphene Oxide-PEG-NH2 in the presence of Mg2+ and Cl-ions,” Coatings, vol. 10, no. 3, pp. 123-135, 2020.

[185] S. Bae, H. Kim, Y. Lee, J. H. Lee, S. Jung, J. H. Lee, S. J. Park, J. H. Ahn, H. Jang, Y. Il Jung, Y. K. Choi, J. Kim, Y. W. Lee, and J. W. Lee, “Roll-to-roll production of 30-inch graphene films for transparent electrodes,” Nat Nanotechnol, vol. 5, no. 8, pp. 574-578, 2010.

[186] S. Gorantla, P. Kumar, R. S. Rajam, K. Krishnan, S. Sharma, R. Kumari, and R. R. Mehta, "A universal transfer route for graphene," Nanoscale, vol. 6, no. 2, pp. 411-418, 2014.

[187] J. Kang, D. Shin, S. Bae, B. H. Hong, J. H. Lee, Y. W. Lee, H. Jang, S. J. Park, and J. W. Lee, "Graphene transfer: Key for applications," 2012.

[188] X. Li, X. Wu, J. Chen, C. Zhang, H. Wang, Y. Gao, C. Shen, Y. Zhang, and Z. Liu, "Transfer of large-area graphene films for high-performance transparent conductive electrodes," Nano Lett, vol. 9, no. 12, pp. 4352-4356, 2009.

[189] P. C. Nickels, A. Böhm, A. Hackenberger, M. J. Milinkovitch, R. L. Frohlich, D. Nadakuduti, S. Waldherr, B. Heuberger, A. Radenovic, and C. Dietler, "Molecular force spectroscopy with a DNA origami-based nanoscopic force clamp," Science, vol. 354, no. 6310, pp. 184-187, 2016.

[190] S. Fischer, C. Hartl, K. Frank, J. O. Rädler, T. Liedl, B. Nickel, M. Herrmann, and F. Kremer, "Shape and interhelical spacing of DNA origami nanostructures studied by small-angle X-ray scattering," Nano Lett, vol. 16, no. 7, pp. 4174-4180, 2016.

[191] Y. Ke, X. Liu, L. Yu, M. Wang, Z. Wang, Z. Fang, and L. Gong, "Multilayer DNA origami packed on a square lattice," J Am Chem Soc, vol. 131, no. 43, pp. 15270-15273, 2009.

[192] M. Raab, C. M. Klinkert, M. F. Hossain, A. T. Petri-Fink, M. Rothen-Rutishauser, M. L. Tanase, J. D. Finkelstein, C. A. Mirkin, and O. S. Wolfbeis, "Using DNA origami nanorulers as traceable distance measurement standards and nanoscopic benchmark structures," Sci Rep, vol. 8, no. 1, pp. 1-10, 2018.

[193] M. Wahl, "Modern TCSPC Electronics: Principles and Acquisition Modes," pp. 1–21, 2014.

[194] W. Becker, "The bh TCSPC Handbook," Scanning, no. 800, 2010.

[195] D. Xiao, N. Sapermsap, M. Safar, M. R. Cunningham, Y. Chen, and D. D. Li, "On Synthetic Instrument Response Functions of Time-Correlated Single-Photon Counting Based Fluorescence Lifetime Imaging Analysis," Front Phys, vol. 9, pp. 1-10, 2021.

[196] A. Perri et al., "Time- and frequency-resolved fluorescence with a single TCSPC detector via a Fourier-transform approach," Opt Express, vol. 26, no. 3, pp. 1-10, 2018.

[197] I. Rech, A. Bovolenta, A. Cominelli, and G. Acconcia, "Toward Constraintless Time-Correlated Single-Photon Counting Measurements: A New Method to Remove Pile-Up

Distortion," IEEE Journal of Selected Topics in Quantum Electronics, vol. 30, no. 1, pp. 1-10, 2024.

[198] B. Li, J. Bartos, Y. Xie, and S.-W. Huang, "Time-magnified photon counting with 550-fs resolution," Optica, vol. 8, no. 8, pp. 1-10, 2021.

[199] W. Becker, A. Bergmann, G. L. Biscotti, and A. Rueck, "Advanced time-correlated single photon counting techniques for spectroscopy and imaging in biomedical systems," in Commercial and Biomedical Applications of Ultrafast Lasers IV, pp. 1-50, 2004.

[200] W. Becker, A. Bergmann, M. A. Hink, K. König, K. Benndorf, and C. Biskup, "Fluorescence Lifetime Imaging by Time-Correlated Single-Photon Counting," Microsc Res Tech, vol. 63, no. 1, pp. 1-12, 2004,

[201] O. Krichevsky and G. Bonnet, "Fluorescence correlation spectroscopy: The technique and its applications," Reports on Progress in Physics, vol. 65, no. 2, pp. 203-256, 2002,

[202] Z. Yang, H. Xu, J. Wang, W. Chen, and M. Zhao, "Single-Molecule Fluorescence Techniques for Membrane Protein Dynamics Analysis," Appl Spectrosc, vol. 75, no. 5, pp. 515-523, 2021.

[203] L. A. Masullo, A. M. Szalai, L. F. Lopez, and F. D. Stefani, "Fluorescence nanoscopy at the sub-10 nm scale," Biophysical Reviews, vol. 13, pp. 1-12, 2021.

[204] J. Zähringer, F. Cole, J. Bohlen, F. Steiner, I. Kamińska, and P. Tinnefeld, "Combining pMINFLUX, graphene energy transfer and DNA-PAINT for nanometer precise 3D super-resolution microscopy," Light Sci Appl, vol. 12, no. 1, 2023.

[205] R. Kumar, D.P. Singh, R. Muñoz, M. Amami, R.K. Singh, S. Singh, and V. Kumar "Graphene-based materials for biotechnological and biomedical applications: Drug delivery, bioimaging and biosensing," 2023.

[206] A. Ghosh, A. Sharma, A.I. Chizhik, S. Isbaner, D. Ruhlandt, R. Tsukanov, I. Gregor, N. Karedla, and J. Enderlein "Graphene-based metal-induced energy transfer for sub-nanometre optical localization," Nat Photonics, vol. 13, pp. 860–865, 2019.

[207] N. Füllbrunn, Z. Li, L. Jorde, C. P. Richter, R. Kurre, L. Langermeyer, C. Yu, C. Meyer, J. Enderlein, C. Ungermann, J. Piehler, and C. You "Nanoscopic anatomy of dynamic multi-protein complexes at membranes resolved by graphene-induced energy transfer," Elife, vol. 10, pp. 1-12, 2021.

[208] R. M. R. Adão, R. Campos, E. Figueiras, P. Alpuim, and J. B. Nieder, “Graphene setting the stage: tracking DNA hybridization with nanoscale resolution,” 2d Mater, vol. 6, no. 4, p. 045056, 2019.

[209] J. M. Park, Y. Cao, L-Q. Xia, S. Sun, K. Watanabe, T. Taniguchi, and P. Jarillo-Herrero “Robust superconductivity in magic-angle multilayer graphene family,” Nat Mater, vol. 21, no. 8, 2022.

[210] S. Turkel, J. Swann, Z. Zhu, M. Christos, K. Watanabe, T. Taniguchi, S. Sachdev, M.S. Scheurer, E. Kaxiras, C.R. Dean, and A.N. Pasupathy “Orderly disorder in magic-angle twisted trilayer graphene,” Science, vol. 376, no. 6589, 2022.

[211] S. Kaushal, M. Kaur, N. Kaur, V. Kumari, and P. P. Singh, “Heteroatom-doped graphene as sensing materials: A mini review,” 2020.

[212] Y. Han, L. Gao, J. Zhou, Y. Hou, Y. Jia, K. Cao, K. Duan, and Y. Lu “Deep Elastic Strain Engineering of 2D Materials and Their Twisted Bilayers,” 2022.

[213] N. P. Kazmierczak, M. Van Winkle, C. Ophus, K.C. Bustillo, S. Carr, H.G. Brown, J. Ciston, T. Taniguchi, K. Watanabe, and D.K. Bediako “Strain fields in twisted bilayer graphene,” Nat Mater, vol. 20, no. 7, pp. 930-935, 2021.

[214] J. Liu, X. Zhang, S. Zhang, Z. Zou, Z. Zhang, Z. Wu, Y. Xia, Q. Li, P. Zhao, and H. Wang “Sequential growth and twisted stacking of chemical-vapor-deposited graphene,” Nanoscale Adv, vol. 3, no. 4, pp. 1374-1380, 2021.

[215] H. C. Hong, J. I. Ryu, and H. C. Lee, “Recent Understanding in the Chemical Vapor Deposition of Multilayer Graphene: Controlling Uniformity, Thickness, and Stacking Configuration,” 2023.

[216] J. H. Cho, S. R. Na, S. Park, D. Akinwande, K. M. Liechti, and M. A. Cullinan, “Controlling the number of layers in graphene using the growth pressure,” Nanotechnology, vol. 30, no. 23, pp. 235704, 2019.

[217] Z. Ni, Y. Wang, T. Yu, and Z. Shen, “Raman spectroscopy and imaging of graphene,” Nano Res, vol. 1, no. 4, pp. 273-290, 2008.

[218] A. C. Ferrari, J.C. Meyer, V. Scardaci, C. Casiraghi, M. Lazzeri, F. Mauri, S. Piscanec, D. Jiang, K.S. Novoselov, S. Roth, and A.K. Geim “Raman spectrum of graphene and graphene layers,” Phys Rev Lett, vol. 97, no. 18, pp. 187401, 2006.

[219] T. Cordes, A. Maiser, C. Steinhauer, L. Schermelleh, and P. Tinnefeld, “Mechanisms and advancement of antifading agents for fluorescence microscopy and single-molecule spectroscopy,” Physical Chemistry Chemical Physics, vol. 13, no. 14, pp. 6699–6709, 2011.

[220] Z. Zhou, Y. Hu, H. Wang, Z. Xu, W. Wang, X. Bai, X. Shan, and X. Lu “DNA Translocation through hydrophilic nanopore in hexagonal boron nitride,” Sci Rep, vol. 3, 2013.

[221] V. Shautsova, A. M. Gilbertson, N. C. G. Black, S. A. Maier, and L. F. Cohen, “Hexagonal Boron Nitride assisted transfer and encapsulation of large area CVD graphene,” Sci Rep, vol. 6, 2016.

[222] R. V. Gorbachev, I. Riaz, R.R. Nair, R. Jalil, L. Britnell, B.D. Belle, E.W. Hill, K.S. Novoselov, K. Watanabe, T. Taniguchi, A. K. Geim, and P. Blake, “Hunting for monolayer boron nitride: Optical and Raman signatures,” Small, vol. 7, no. 4, pp. 465–468, 2011.

[223] L. Wang, I. Meric, P.Y. Huang, Q. Gao, Y. Gao, H. Tran, K. Watanabe, L.M. Campos, D.A. Muller, J. Guo, P. Kim, J. Hone, K.L. Shepard, and C.R. Dean., “One-Dimensional Electrical Contact to a Two-Dimensional Material,” Science, vol. 342, no. 6158, pp. 614–617, 2013.

[224] D. G. Purdie, N. M. Pugno, T. Taniguchi, K. Watanabe, A. C. Ferrari, and A. Lombardo, “Cleaning interfaces in layered materials heterostructures,” Nat Commun, vol. 9, no. 5387, pp. 1-8, 2018.

[225] P. J. Zomer, M. H. D. Guimarães, N. Tombros, and B. J. Van Wees, “Long-distance spin transport in high-mobility graphene on hexagonal boron nitride,” Phys Rev B Condens Matter Mater Phys, vol. 86, no. 16, pp. 161416(R)1–161416(R)5, 2012.

[226] S. Li, Z. Ren, J. Zheng, Y. Zhou, Y. Wan, and L. Hao, “Band gap engineering of graphene/ h -BN hybrid superlattices nanoribbons,” J Appl Phys, vol. 113, no. 3, 2013.

[227] P. Moon and M. Koshino, “Electronic properties of graphene/hexagonal-boron-nitride moiré superlattice,” Phys Rev B, vol. 90, no. 15, p. 155406, 2014.

[228] H. Vovusha, R. G. Amorim, R. H. Scheicher, and B. Sanyal, “Controlling the orientation of nucleobases by dipole moment interaction with graphene/h-BN interfaces,” RSC Adv, vol. 8, no. 12, pp. 6527–6531, 2018.

[229] Z. Kong, W. Zheng, Q. Wang, H. Wang, F. Xi, L. Liang, and J. Shen, “Charge-tunable absorption behavior of DNA on graphene,” J Mater Chem B, vol. 3, no. 24, pp. 4957–4962, 2015.

[230] A. Benvidi, M. D. Tezerjani, A. D. Firouzabadi, M. Mazloum-Ardakani, and S. M. Moshtaghioun, “Application of graphene oxide nanosheets as probe oligonucleotide immobilization platform for DNA sensing,” Journal of the Iranian Chemical Society, vol. 13, no. 11, pp. 2135–2142, 2016.

[231] W. Lu, G. Chang, Y. Luo, F. Liao, and X. Sun, “Method for effective immobilization of Ag nanoparticles/graphene oxide composites on single-stranded DNA modified gold electrode for enzymeless H 2O2 detection,” J Mater Sci, vol. 46, no. 15, pp. 5260–5266, 2011.

[232] D. H. Shin, S.H. Kim, K. Coshic, K. Watanabe, T. Taniguchi, G. Verbiest, S. Caneva, A. Aksimentiev, P.G. Steeneken, and C. Joo “Diffusion of DNA on Atomically Flat 2D Material Surfaces,” bioRxiv, 2023.